
Modelling Light-induced Charge-transfer from Transition-metal-doped Aluminium Clusters to Carbon Dioxide

Dissertation
zur Erlangung des Doktorgrades
an der Fakultät für Mathematik, Informatik und Naturwissenschaften
Fachbereich Chemie
der Universität Hamburg

vorgelegt von
Alexandra Göbel

Hamburg
2021

Für Oma und Opa.

Gutachter/in der Dissertation:

Prof. Dr. Gabriel Bester
Prof. Dr. Carmen Herrmann

Zusammensetzung der Prüfungskommission:

Prof. Dr. Gabriel Bester
Prof. Dr. Volker Abetz
Prof. Dr. Arwen Pearson

Vorsitzender der Prüfungskommission:

Prof. Dr. Gabriel Bester

Datum der Disputation:

20.08.2021

The work underlying this dissertation has been carried out from June 2017 to July 2021 at the Max-Planck Institute for the Structure and Dynamics of Matter in Hamburg as well as at Imperial College in London (UK) in the groups of Prof. Angel Rubio and Dr. Johannes Lischner.

List of Publications

- doi:10.1021/acs.jpca.1c02621: Göbel, A.; Rubio, A. & Lischner, J., Light-Induced Charge Transfer from Transition-Metal-Doped Aluminum Clusters to Carbon Dioxide, *The Journal of Physical Chemistry A*, **2021**.
- Another publication on the results presented in chapters 4.3 and 4.4 (Electronic Properties of $[\text{Al}_{54}M]-\text{CO}_2$ and $[\text{Al}_{146}M]-\text{CO}_2$) is in preparation.

Contents

1	Carbon Dioxide – A Global Challenge	6
1.1	Catalytic Conversion of CO ₂	6
1.2	Outline and Motivation	10
2	Methods	12
2.1	Density Functional Theory (DFT)	12
2.2	Forces and Relaxations	16
2.3	XC Functionals	17
2.4	Pseudopotentials (PPs) versus All-Electron Calculations	21
2.5	Basis Sets	23
2.6	Charge Partitioning Schemes	24
2.7	Time-dependent Density Functional Theory (TDDFT)	27
3	Results and Discussion	33
3.1	Relaxed Structures of [Al ₁₂ M], [Al ₅₄ M] and [Al ₁₄₆ M] Aluminium Clusters with CO ₂	33
3.1.1	Summary	44
3.2	Electronic Properties of [Al ₁₂ M]–CO ₂	46
3.2.1	Ground State Properties	46
3.2.2	Excited State Properties	55
3.2.3	Summary	61
3.3	Electronic Properties of [Al ₅₄ M]–CO ₂	64
3.3.1	Ground State Properties	64
3.3.2	Excited State Properties	69
3.3.3	Comparison of the results to [Al ₁₂ M]–CO ₂	72
3.3.4	Summary	74
3.4	Electronic Properties of [Al ₁₄₆ M]–CO ₂	76
3.4.1	Ground State Properties	76
3.4.2	Comparison of the results to [Al ₁₂ M]–CO ₂ and [Al ₅₄ M]–CO ₂	78
3.4.3	Summary	81
4	Conclusion and Outlook	83
5	Computational Details	86
5.1	Geometry Optimizations	86
5.2	Ground State and Excited State Properties	88

Acronyms

ALDA	adiabatic local density approximation
CGF	contracted Gaussian function
CT	charge-transfer
DFT	density functional theory
DOS	density of states
ELF	electron localization function
GGA	generalized gradient approximation
GTO	Gaussian type orbital
HOMO	highest occupied molecular orbital
KS	Kohn-Sham
LCAO	linear combination of atomic orbitals
LDA	local density approximation
LICT	light-induced charge-transfer
LSD	local spin density approximation
LUMO	lowest unoccupied molecular orbital
PBE	Perdew-Burke-Ernzerhof
pDOS	projected density of states
PP	pseudopotential
SCF	self-consistent field
SIC	self-interaction correction
SCF	self-consistent field

TDDFT	time-depndent density functional theory
vdW	van der Waals
XC	exchange correlation

Abstract

A lot of effort has been concentrated in the catalytic conversion of carbon dioxide, turning it from a pollutant into valuable basis chemicals. One crucial step herein is the transfer of an electron into CO_2 which results in increased reactivity of the molecule. Different approaches such as plasma activation or electro-chemical activation have been used to achieve this electron transfer and a wide variety of catalysts has been shown to induce charge-transfer. However, these catalysts often contain large amounts of precious metals which makes the conversion process expensive. Aluminium with its low cost and high natural abundance could be an alternative to Au-, Cu- or Rh-based catalysts. Another common problem in catalysis is the challenge of understanding structure and activity relationships. Small clusters or molecules with well defined structures, also referred to as atomically defined catalysts, are useful tools for gaining deeper insights into catalytic processes.

We studied a total of 55 different neutral and singly-negatively charged atomically-defined aluminium clusters of varying sizes with and without dopants with respect to their ability to adsorb and activate carbon dioxide. The clusters in this study consisted of either 13, 55 or 147 atoms which form complete icosahedral shells. For the doped systems, one of the aluminium atoms from the outer shell was substituted by one of the following dopants: H, B, C, Si, N, P, O, S, Zr, Mn, Fe, Ru, Co, Ni, Cu, Ti, Pd, Rh, Ag and Au. We found that only transition-metal-doped clusters were capable of activating CO_2 . Adsorption distances above 2.3 Å never resulted in bent CO_2 geometries which are associated with activation while distances below 2.3 Å always led to O-C-O angles significantly smaller than 180° .

We then investigated the ground-state and excited-state electronic properties of the 7 smallest neutral systems for which the shortest adsorption distances were observed which were $[\text{Al}_{12}\text{Zr}]-\text{CO}_2$, $[\text{Al}_{12}\text{Mn}]-\text{CO}_2$, $[\text{Al}_{12}\text{Fe}]-\text{CO}_2$, $[\text{Al}_{12}\text{Ru}]-\text{CO}_2$, $[\text{Al}_{12}\text{Co}]-\text{CO}_2$, $[\text{Al}_{12}\text{Ni}]-\text{CO}_2$ and $[\text{Al}_{12}\text{Cu}]-\text{CO}_2$. In the case of the Fe- and Cu-doped clusters, CO_2 was not activated. We found that systems which exhibit ground-state CO_2 activation are more prone to transfer the excess electron from the molecule back onto the cluster when excited. On the other hand, systems without CO_2 activation at the ground-state level showed electron transfer into carbon dioxide upon excitation. We computed the same properties for the medium-sized clusters $[\text{Al}_{54}\text{Zr}]-\text{CO}_2$, $[\text{Al}_{54}\text{Mn}]-\text{CO}_2$, $[\text{Al}_{54}\text{Fe}]-\text{CO}_2$, $[\text{Al}_{54}\text{Ru}]-\text{CO}_2$, $[\text{Al}_{54}\text{Co}]-\text{CO}_2$, $[\text{Al}_{54}\text{Ni}]-\text{CO}_2$ and $[\text{Al}_{54}\text{Cu}]-\text{CO}_2$. We found that the trends remained the same but ionization energies as well as the onset of the light-induced charge-transfer (LICT) were generally red-shifted. We also discovered that $[\text{Al}_{54}\text{Ni}]-\text{CO}_2$ resulted in a dissociation of CO_2 on the cluster surface at ground-state level. We then compared the ground-state electronic properties of the selected small- and medium-sized systems to those of $[\text{Al}_{146}\text{Zr}]-\text{CO}_2$, $[\text{Al}_{146}\text{Mn}]-\text{CO}_2$, $[\text{Al}_{146}\text{Ru}]-\text{CO}_2$, $[\text{Al}_{146}\text{Co}]-\text{CO}_2$, $[\text{Al}_{146}\text{Ni}]-\text{CO}_2$ and $[\text{Al}_{146}\text{Cu}]-\text{CO}_2$. We found that with increasing cluster size, differences in ionization energy between differently doped clusters are reduced and adsorption gets weaker. We only observed high-spin ground-states for systems with Mn-, Fe- or Co-doping. Our study gives insights into the effect of different dopants and cluster sizes on charge-transfer and paves the way to a more rational design of aluminium catalysts for CO_2 activation.

Zusammenfassung

Viele Bemühungen sind in die katalytische Umwandlung von Kohlenstoffdioxid geflossen um den Schadstoff in wertvolle Basischemikalien umzuwandeln. Ein entscheidender Schritt hierbei ist die Übertragung eines Elektrons in das CO₂-Molekül. Dadurch reduziert sich seine Stabilität und es wird reaktiver. Hierzu wurden verschiedene Ansätze verfolgt und eine große Bandbreite an Katalysatoren hat sich als aktiv für diese Ladungsübertragung erwiesen. Allerdings beinhalten diese Katalysatoren oft große Mengen an Edelmetallen, was die Kosten dieser Prozesse in die Höhe treibt. Eine Alternative hierfür könnte Aluminium darstellen. Durch sein hohes natürliches Vorkommen ist es deutlich kostengünstiger als andere Metalle wie beispielsweise Cu, Au oder Rh. Ein weiteres Problem in der Katalyse stellt die Schwierigkeit dar, Struktur-Aktivitätsbeziehungen herzuleiten auf Grund der Komplexität vieler katalytischer Systeme. Hier haben sich sogenannte atomar definierte Katalysatoren als nützlich erwiesen, welche aus kleinen Clustern oder Molekülen mit wohldefinierten Strukturen bestehen. Diese ermöglichen es vielfach, einen tieferen Einblick in katalytische Prozesse zu erlangen.

Wir haben insgesamt 55 solcher atomar definierten Katalysatoren im Hinblick auf ihre Fähigkeit CO₂ zu adsorbieren untersucht. Diese umfassten 13, 55 und 147 atomige Aluminiumcluster mit und ohne Dotierung. Diese Atomanzahlen ergeben vollständige Ikosaederschalen. Hierbei waren einige Cluster einfach negativ geladen und andere neutral. Als Dotieratome wurden H, B, C, Si, N, P, O, S, Zr, Mn, Fe, Ru, Co, Ni, Cu, Ti, Pd, Rh, Ag und Au eingesetzt. Hierfür wurde eines der Aluminiumatome in der äußeren Ikosaederschale gegen ein Dotieratom ausgetauscht. Es zeigte sich, dass nur Übergangsmetalle in der Lage sind, CO₂ zu aktivieren. Hierbei erweist sich 2.3 Å Abstand zwischen Cluster und Molekül als Schwellenwert, über welchem nur lineares CO₂ zu finden ist, wohingegen alle Werte unter 2.3 Å ausnahmslos zu gewinkelttem CO₂ und damit zu Aktivierung führen.

Desweiteren haben wir die elektronische Struktur einiger ausgewählter Systeme im Grund- sowie im angeregten Zustand untersucht. Hierzu wurden die 7 kleinsten neutralen Systeme welche die niedrigsten Adsorptionslängen aufwiesen selektiert. Dabei handelt es sich um [Al₁₂Zr]-CO₂, [Al₁₂Mn]-CO₂, [Al₁₂Fe]-CO₂, [Al₁₂Ru]-CO₂, [Al₁₂Co]-CO₂, [Al₁₂Ni]-CO₂ und [Al₁₂Cu]-CO₂. Die mit Fe und Cu dotierten Systeme resultierten hierbei nicht in aktiviertem CO₂. Es zeigte sich, dass Systeme, die im Grundzustand Ladung auf das CO₂ Molekül übertragen hatten unter Anregung eher zu einem Rücktransfer dieser Ladung auf den Cluster neigen. Dahingegen zeigten Systeme, welche im Grundzustand zu keiner CO₂ Aktivierung geführt hatten nur Ladungstransfer vom Cluster auf das Molekül unter Anregung.

Die selben Kenngrößen wurden für die mittelgroßen Cluster [Al₅₄Zr]-CO₂, [Al₅₄Mn]-CO₂, [Al₅₄Fe]-CO₂, [Al₅₄Ru]-CO₂, [Al₅₄Co]-CO₂, [Al₅₄Ni]-CO₂ und [Al₅₄Cu]-CO₂ ermittelt. Hierbei zeigte sich, dass die Trends die sich für die kleinen Systeme ergeben hatten sich ebenso hier beobachten lassen, allerdings waren beispielweise Ionisationenergien rotverschoben. Darüber hinaus resultierte der Ni-dotierte Cluster in einer Dissoziation des CO₂ Moleküls im Grundzustand. Die Ergebnisse für den Grundzustand der kleinen und mittleren Systeme wurden mit denen der größten Cluster, [Al₁₄₆Zr]-CO₂,

$[\text{Al}_{146}\text{Mn}]-\text{CO}_2$, $[\text{Al}_{146}\text{Ru}]-\text{CO}_2$, $[\text{Al}_{146}\text{Co}]-\text{CO}_2$, $[\text{Al}_{146}\text{Ni}]-\text{CO}_2$ und $[\text{Al}_{146}\text{Cu}]-\text{CO}_2$, verglichen. Hierbei stellte sich heraus dass mit steigender Clustergröße sich die Ionisationsenergien zwischen unterschiedlich dotierten Clustern angleichen. Desweiteren konnte in einigen Fällen eine Abnahme der Adsorptionsstärke beobachtet werden. High-spin Zustände konnten, unabhängig von der Clustergröße, nur für Systeme die entweder Mn, Fe oder Co enthielten beobachtet werden. Unsere Untersuchungen eröffnen Einblicke in die Auswirkung von Dotieratomen und unterschiedlichen Clustergrößen auf die Ladungsübertragung von kleinen, atomar definierten Aluminiumclustern auf CO_2 . Dies ermöglicht ein rationaleres Katalysatordesign im Hinblick auf die katalytische Aktivität dieser Systeme zur CO_2 Aktivierung.

1 Carbon Dioxide – A Global Challenge

In this chapter we will give the reader a brief overview of the past and current developments in the field of catalytic CO₂ activation and conversion and address problems which our work is attempting to help resolve. We will start by commenting on the impact carbon dioxide has on our environment and the possibility of using CO₂ as a carbon feedstock. Catalytic conversion of CO₂ into useful chemicals as a promising approach will be discussed and several catalysts will be introduced which have exhibited activity for those processes. Catalytic activation of CO₂ as a crucial step and the main focus of this thesis will be discussed and different approaches are introduced. In the last part, we will explain the motivation behind the research conducted within this thesis.

1.1 Catalytic Conversion of CO₂

One of the biggest global challenges that society is facing at the moment is climate change. A significant driving force of global warming are carbon dioxide emissions. This process has been going on for several decades now, and if action is not taken immediately the impact will not be fully reversible[1, 2] At the current stage, carbon dioxide is not only a burden to the environment but facilities producing it have to purchase emission allowances which can be costly[3]. A possible solution to this problem would be the usage of CO₂ as a carbon feedstock. Due to carbon dioxide's high thermodynamic stability this is a challenging task.[4] A lot of research has focused on the development of new catalysts for CO₂ conversion into useful products like fuels or polymers.[5, 6, 7, 8] One of the key steps for these reactions is the transfer of an electron into the lowest unoccupied molecular orbital (LUMO) of the carbon dioxide molecule. This leads to a weakening of the C-O bonds in addition with a bending of the linear molecule and is often referred to as activation. The electron transfer into CO₂ is accompanied by an "Umpolung" of the carbon atom, i.e. the formerly partially positive C then bears a negative partial charge, which opens new reaction pathways (e.g. for electrophilic attacks).[4]

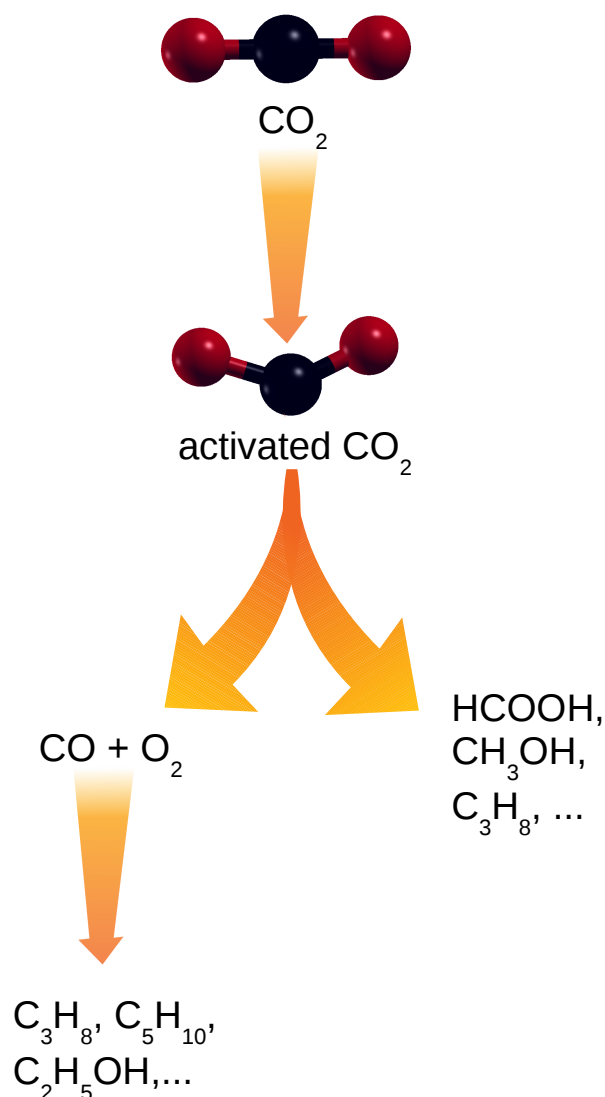


Figure 1.1: Illustration of the products obtained via CO_2 activation. After activation, the CO_2^- anion can either dissociate into carbon monoxide and oxygen or can be directly used for further reactions.

The methods used to activate CO_2 are diverse and range from plasma-treatment[9], electrochemical-activation[10] and thermal activation methods (e.g. on metal surfaces)[11] to photo-activation[5]. Depending on the method chosen for activation, the products will vary. As a general trend, plasma and thermally activated CO_2 has a tendency to dissociate into CO and oxygen while the other methods tend to produce the radical anion, $\text{CO}_2^{\cdot-}$, as an intermediate product which can then further react to formic acid, methane, methanol, higher hydrocarbons and other products.[4] Carbon monoxide in combination with hydrogen gas on the other hand can be transformed to a wide variety of products like olefines and hydrocarbons for example via a Fischer-Tropsch synthesis.[12] This is illustrated in figure 1.1. However, the resulting products are of course highly dependent

on the catalyst and reaction conditions like temperature, solvent and pressure. A crucial role is also played by the interaction between CO_2 and the catalyst since adsorption of the molecule to the surface with its carbon atom results in steric hindrance of attacks to this atom: The carbon atom, especially when CO_2 bends on the surface, is harder to access since it is being shielded by the oxygen atom. As a result, this will predominantly produce CO as a product.[13] Overall, the field is very complex and a lot of catalysts already exist, but in order to achieve efficiencies that would allow CO_2 conversion to become an environmentally friendly and clean energy source, a lot of additional research is still necessary. In particular, some conversion methods like plasma-activation and electrochemical activation require large amounts of energy[14] which makes them dependent on other sources like fossil fuels.[6] Another problem lies in the low quantum yields of current photo-catalysts. Even photo catalysts with comparably high quantum yields of over 10% under solar-light irradiation only result in relatively low CO_2 conversion rates of 3.5% in a continuous flow reactor at 225°C.[15] This need for high temperatures originates from the endothermic nature of most conversion reactions.[14] However, 10% quantum yield is considered the threshold above which photo catalytic conversion of CO_2 becomes economically interesting, but this is just a rule of thumb. In reality, there is many more factors like e.g. catalyst cost, lifetime and reaction temperature (which mostly equates to operational cost).[6]

Catalysts can roughly be divided into a homogeneous and a heterogeneous category. Homogenous catalysts are organo-metallic complexes which consist of a central metal atom which is surrounded by ligands. Their structure is well defined and they are often dissolved within the reaction batch. They usually only have one active-site and their properties can be easily tailored.[16] They are generally operated at relatively mild conditions with respect to pressure and temperature and can result in impressive conversion rates due to their easily accessible active sites. However, homogeneous catalysts are often expensive[17], not just because of the precious central metal but also due to the pricey ligands.[18] In addition to this, recycling or separating the catalyst from the reaction batch is usually difficult and expensive.[19] Because of homogeneous catalysts' high selectivity also with regard to chiral products, they are mostly used for the production of fine-chemicals e.g. in the pharmaceutical sector.[18] There are plenty of homogenous catalysts that have shown to be active for CO_2 conversion. "FCAT", an Fe porphyrin catalyst, produces CO[20] and $[\text{Rh}(\text{cod})\text{Cl}_2]-\text{Ph}_2\text{P}(\text{CH}_2)_4\text{PPh}_2$ was shown to convert CO_2 into formic acid[21]. Interestingly, the Ru-based homogenous catalyst system of pentaethylenhexamin and "Ru-Macho-BH" led to 79% yield of methanol by just being operated with regular air[22]. Another homogenous catalyst, $[\text{Co}(\text{NTB})\text{CH}_3\text{CN}](\text{CLO}_4)_2$, has been shown to photo-catalytically reduce CO_2 to CO in water under illumination by visible light.[23]

Heterogeneous catalysts on the other hand consist of materials with high surface areas and their exact structure and active sites are often hard to characterize which makes it harder to systematically understand the origin of their catalytic activity and improve their properties.[16] They usually show lower selectivities and conversion rates than homogenous catalysts, but due to their high robustness, long life-cycles, easy separation from the reaction and low cost they are the work-horses in many industrial processes.[16, 24, 17] Heterogeneous catalysts are however more likely to suffer from poisoning and, as a result,

loss of activity over time and, especially in porous materials, diffusion can be a limiting factor in terms of turn-over frequency.[16] In the field of heterogeneous catalysts there is also a steadily growing variety of systems which have proven to be catalytically active in terms of CO₂ conversion. The species at the active sites are usually transition-metals like Ni, Ru, Rh, Pd, Pt, Fe, Cu, Co, Ag or Au.[13] Examples of heterogeneous catalytic systems used in CO₂ conversion are "Fe-Cu-Al-K(2)" (weight ratios: 100:6.6:15.7:4, alumina is added via co-precipitation) which exhibits CO₂ conversion of up to 30%[25], Cu/ZnO catalysts[26] which were used for methanol synthesis from CO₂ or supported Ni catalysts which have been reported to have CO₂ conversion yields of almost 50 %.[27]

Besides enzyme catalysts which we will not cover here, there is another class of catalysts which has gained relevance over the last years. These catalysts are called "atomically-defined" and usually consist of small, well-defined metallic nano clusters. The surface to volume ratio of atomically defined catalysts is much higher than in most heterogeneous catalysts but they often suffer from stability issues.[28] Despite the promising results obtained from heterogeneous catalysts, it is a difficult task to understand the catalytic activity of these systems and draw conclusions between structural properties and the resulting catalytic behaviour. In the field of atomically defined catalysts, this gap between homogenous and heterogeneous catalysts can be bridged. Beyond their academic interest for a better understanding of catalytic processes, they have been shown to exhibit high activity, selectivity, stability and recyclability, making them promising systems for further studies.[28]

CO₂ has been reduced to CO on [Cu₃₂H₂₀(S₂P(OiPr)₂)₁₂][29]. [Au₂₅(SR)₁₈]⁻, which belongs to the class of Au_n(SR)_m clusters, which have proven to endure temperatures of up to 200 °C[30], has been used for the electro reduction of CO₂. [31] The introduction of different dopants into the structure of Au₂₄M(SR)₁₈ (M = Pt, Pd, Hg, and Cd) revealed that Hg and Cd are always located in the shell of the icosahedron and never at its centre[32] Most of the catalytic systems, no matter if homogenous, heterogeneous or atomically defined, contain large amounts of precious metals. In order to develop affordable high-throughput catalysts, there is a need for cheaper options. In recent years, aluminium has seen a renaissance.[33] It is not only cheap but also has one of the highest natural abundances of all elements. Its rediscovery came from the field of plasmonics since it was found that Al nanoparticles did not only exhibit a localized surface plasmon, but its frequency could be tuned across a much wider range than those of the more common plasmonic materials gold and silver.[34] In addition to this, solar devices from Al nanoparticles are easy to fabricate.[35] One of the drawbacks of using Al, though, is its tendency to oxidize since it is non-precious.[34] It has been shown though that the oxide layer is porous and still allows diffusion of small molecules.[36] One of the leading groups in the field of plasmonics, Halas and co-workers, have used Al@CuO nanostructures to produce synthesis gas (CO and H₂) from water and CO₂. [37] In another publication they used aluminium nanoparticles as the basis of an antenna reactor: they decorated the surface of the Al nanoparticles with different transition-metals (Fe, Co, Ni, Ru, Rh, Pd, Ir and Pt) which catalyses a reaction while the plasmonic nano-particle leads to increased light absorption and generates local regions of higher temperature ("hot-spots"). [38]

Another important pillar of understanding catalytic activities are systematic theoretical studies. For icosahedral, 13-atomic Al clusters doped with Al, Be, Zn, Ni, Cu, B or P at

their centre, Zhao et al. studied CO₂ adsorption. They used DFT and considered neutral as well as singly positively and negatively charged systems.[39] They found adsorption to be tunable with the dopant and showed the catalytic potential of such structures. In a second publication, they showed that these structures are not just capable of adsorbing CO₂ but also of activating and dissociating it.[40] Their studies were focused on ground-state properties and did not include light absorption spectra or excited-state properties which are relevant to photo catalysis.

1.2 Outline and Motivation

The aim of this work is to study the effect of dopants on small aluminium clusters' electronic structure and their catalytic behaviour in terms of CO₂ adsorption and activation. Additionally, the size-dependence of parameters such as adsorption energy, ionisation energy and spin-state will be investigated and general trends will be discussed to help understand and improve catalysts for CO₂ conversion and pave the way towards the development of cheaper alternatives to the regular precious metal catalysts.

We have studied the more reactive Al clusters with the dopant located in the outer icosahedron shell. We will refer to them as "[Al₁₂M]" throughout this work. *M* is the placeholder for a wide variety of dopants (Al, B, C, H, N, O, P, S and Si; Zr, Mn, Fe, Ru, Co, Ni, Cu, Ti, Pd, Rh, Ag and Au). We have chosen the notation in square brackets to indicate the coordinative nature of the structures (one Al atom at the centre is surrounded by 11 other Al atoms and one dopant).

In the first part of this work, we will focus on the abilities of different dopants to adsorb carbon dioxide. Then we will investigate the electronic structure of the most promising candidates both in the ground- and in the excited state. The last part of this thesis is concerned with the size dependence of these properties and we will study systems with one and two more icosahedral shells, [Al₅₄M] and [Al₁₄₇M], and compare the results.

2 Methods

In this chapter we will briefly describe the methods that were used to obtain the results presented in this thesis. We will start by introducing the general concepts of Density Functional Theory (DFT) as well as some vital parts of it such as different exchange-correlation (XC) functionals, discuss forces and relaxations, the differences between all-electron calculations and pseudopotential (PP) approaches, different basis sets and last but not least the pitfalls of charge-partitioning schemes. In the last part we will cover Time-dependent Density Functional Theory (TDDFT). In particular, we will cover how absorption spectra can be obtained from time-propagations and introduce the Casida formalism of TDDFT. In the following chapter, atomic units will be used unless stated otherwise. In particular, this means that $\hbar = m_e = e = 4\pi\epsilon_0 = 1$.

2.1 Density Functional Theory (DFT)

In this section we will start off with the fundamental concepts of Density Functional Theory (DFT), namely the Hohenberg-Kohn theorem and the Kohn-Sham theorem. We will then talk about more specific aspects of the general theory like spin-polarized DFT, the delta-SCF (SCF = self-consistent field) approach and common problems in DFT like the difference between Kohn-Sham energies and quasi-particle energies.

Many quantum-mechanical methods like Hartree-Fock or coupled cluster theory are centred around many-electron wave functions. While many-electron wave functions contain all the information that is possible to acquire about a system and all observables can be calculated from them, they do not have a direct physical meaning and cannot be measured. Considering that the wave function's dimensionality grows exponentially with system size, it becomes clear that such approaches are only applicable to systems with few atoms.[41] In reality though, usually the use of many atoms is required in order to describe materials.

One approach to overcome this problem is density functional theory (DFT). Here, the electron density $n(\vec{r})$ with \vec{r} as the electronic coordinates of a system is the relevant quantity from which its properties can be calculated. In contrast to the many-body wave function $\Psi(x_1, x_2, \dots, x_N)$, the density of the N -electron system, is an observable which can be measured and can be written as $n(\vec{r}) = N \sum_{\sigma_2, \dots, \sigma_N} \int d^3\vec{r}_2 \dots \int d^3\vec{r}_N |\Psi(\vec{r}\sigma, \vec{r}_2\sigma_2, \dots, \vec{r}_N\sigma_N)|^2$ [42]. Here x_i denotes the electronic coordinates of the i^{th} electron, which consist of the

spin σ_i and spatial coordinates r_i . The space integral over the density yields the number of electrons in the system. The integral over a volume in space of the density can be interpreted as the probability of finding an electron within this volume at position \vec{r} . The density only depends on the spatial (and spin-) coordinates \vec{r} and it is sufficient to calculate relevant quantities like the total energy of the system which was shown by Hohenberg and Kohn[41]. The atomic nuclei with their positive charge form a potential $\hat{V}(\vec{r})$ which interacts with the electrons. Assuming that the system has a non-degenerate ground-state, a potential $\hat{V}(\vec{r})$ can only have one corresponding ground-state density $n_0(\vec{r})$. Beyond that, Hohenberg and Kohn proved that this statement is also reversible, meaning that considering a ground-state density $n_0(\vec{r})$, the potential $\hat{V}(\vec{r})$ is determined: One can state that there is a Hamiltonian $\hat{H} = \hat{T} + \hat{U} + \hat{V}(\vec{r})$ in which \hat{T} and \hat{U} denote the kinetic energy operator and the electron-electron interaction, respectively. We will treat the nuclei as clamped since electrons move on a much faster time scale than nuclei (hence there is no kinetic-energy term considered for the nuclei). This is also referred to as the Born-Oppenheimer approximation. \hat{H} has a ground-state wave function $\Psi(\vec{r})$ and, as stated above, a ground-state electron density $n_0(\vec{r})$. Hohenberg and Kohn showed that there exist no two different potentials resulting in the same ground-state density. On the other hand, this means that there is a bijection between ground-state densities and external potentials, since one determines the other. For this proof which lays out the foundations of DFT, Kohn was awarded the Nobel-prize in chemistry in 1998.

The Hohenberg-Kohn theorem implies more than just the bijection between the external potential and the ground-state density: it also shows that the total ground-state energy E is a functional of the ground-state density $n_0(r)$ and can be written as

$$E[n_0(\vec{r})] = \langle \Psi | \hat{T} + \hat{U} | \Psi \rangle + \langle \Psi | V(\vec{r}) | \Psi \rangle = F[n_0(\vec{r})] + \int n_0(\vec{r}) V(\vec{r}) d\vec{r}. \quad (2.1)$$

The ground-state density inserted into the exact functional $F[n_0(\vec{r})]$ minimizes the total energy of the system. By using the density, the three-dimensional problem which wave functions pose is reduced to a 4-dimensional one (spatial coordinates and spin). Strictly speaking, DFT is an exact ab initio theory. There is only one problem, which — in practice — is a major one: $F[n_0(\vec{r})]$ is not known.

While the integral in equation 2.1 describes the Coulomb interactions between the density and the nuclei, $F[n_0(\vec{r})]$ contains the kinetic energy and the electron-electron interactions. Kohn and Sham paved the way to transform DFT from a theoretical construct to one of the most successful and widely used theories of today's electronic structure calculations. A lot of the difficulties of finding a generally valid expression for $F[n_0(\vec{r})]$ are caused by the problem of quantifying electron-electron interactions in terms of density (e.g. the term for electron exchange is well defined within Hartree-Fock theory which is based on wave functions). To overcome these problems, Kohn and Sham defined an auxiliary system which generates the same density as the real one but consists of non-interacting electrons. This Kohn-Sham (KS) density can be written in terms of KS single particle wave functions $\phi_i(\vec{r})$ as $n_{KS}(\vec{r}) = 2 \sum_{i=1}^{N/2} |\phi_i(\vec{r})|^2$ with the factor 2 arising from the fact that at this point we are not considering different spins of electrons but treat states that are doubly occupied. As a result of the Hohenberg-Kohn theorem it

2 Methods

follows that the external potential is not the same as $\hat{V}(\vec{r})$ and to avoid confusion we will denote it by \hat{V}_{KS} . Some contributions of \hat{V}_{KS} can be accurately described, so the KS potential can be rewritten in the following way:

$$V_{KS}(\vec{r}) = \hat{V}(\vec{r}) + \int \frac{n_0(\vec{r}')}{|\vec{r} - \vec{r}'|} d\vec{r}'^3 + \hat{V}_{xc}[n_0(\vec{r})](\vec{r}). \quad (2.2)$$

The first term denotes the external potential and describes any external forces acting on the electrons (e.g. the Coulomb potential of the nuclei but also external electro-magnetic fields), the second term is the so-called Hartree potential which describes the Coulomb interaction of one electron with the entire density which hence also includes interactions of the electron with itself. The last term is the exchange-correlation (XC) potential which includes all many-body effects. It is worth noting that the kinetic energy functional is not explicitly known for a density but can be accurately described for the KS wave functions (since the KS electrons are non-interacting, so even in this description we are missing some parts that come from many-body effects like correlation):

$$\hat{T}[n_0] \approx \sum_{i=1}^N \langle \phi_i | -\frac{1}{2} \nabla^2 | \phi_i \rangle. \quad (2.3)$$

The ground-state energy of the KS potential \hat{V}_{KS} can be written as

$$E_{tot} = \hat{T}[n_0(\vec{r})] + E_H[n_0(\vec{r})] + E_{xc}[n_0(\vec{r})] + \int n_0(\vec{r}) V(\vec{r}) d\vec{r}^3, \quad (2.4)$$

with E_H denoting the Hartree energy and E_{xc} describing the xc energy. The term "XC energy" generally includes everything that has been neglected due to either the non-interacting nature of the KS wave functions (like in the calculation of the kinetic energy) or since its description in terms of density is inaccurate (e.g. the Hartree potential contains Coulomb interactions of the electron with itself). One of the upsides of this approach is that the known terms in equation 2.4 already include the largest contributions to the total energy, so if one approximates $E_{xc}[n_0(\vec{r})]$, only smaller parts of the total energy are affected.[43] The nature of the most popular approximations for E_{xc} will be described in a later section (see section 2.3).

So far all quantities are described in terms of the total density, in most systems though spin plays a more or less significant role. The adaptation of the previous equations to accommodate spin is fairly straightforward: Instead of treating one density, two different densities are treated, one for spin-up and one for spin-down electrons. We will denote them by $n_{0\uparrow}(\vec{r})$ and $n_{0\downarrow}(\vec{r})$, respectively. The total density $n_0(\vec{r})$ is equal to $n_{0\downarrow}(\vec{r}) + n_{0\uparrow}(\vec{r})$. However, when using spin-dependent DFT, there is a need for functionals that are dependent on spin σ (e.g. an external potential containing a magnetic field or an XC potential that contains exchange only between electrons of the same spin):

$$\hat{V}_{KS}(\vec{r}, \sigma) = -\frac{1}{2} \nabla^2 + \hat{V}(\vec{r}) + \int \frac{n_0(\vec{r}')}{|\vec{r} - \vec{r}'|} d^3(\vec{r}') + \hat{V}_{xc}[n_{0\downarrow}(\vec{r}), n_{0\uparrow}(\vec{r})]. \quad (2.5)$$

The exact functional is of-course spin-dependent.[44]

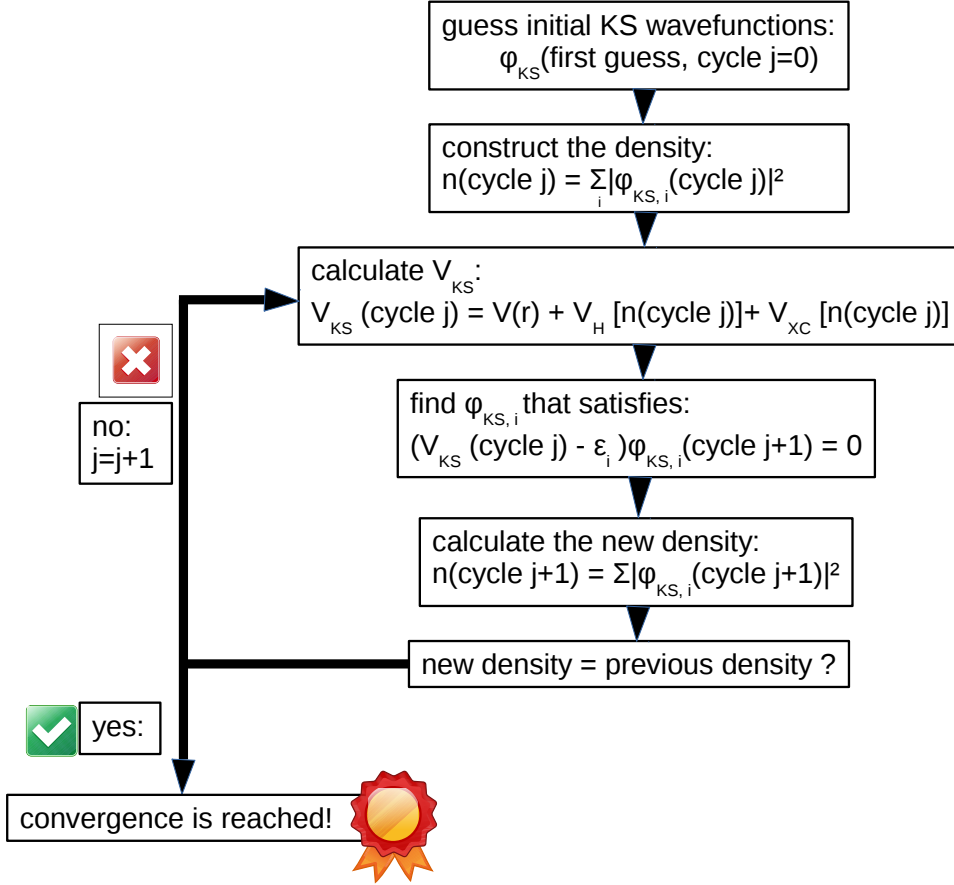


Figure 2.1: Scheme for self-consistent solving of the coupled KS equations.

Usually neither the KS potential nor the ground-state KS wave functions (or even $n_0(\vec{r})$) are known. They can still be calculated by taking advantage of the bijective nature between the *external* potential (which is usually known) and the density as well as the fact that the ground-state is defined as a system's state that is lowest in energy. Combination of these traits leads to a self-consistent problem which is often referred to as a self-consistent field (SCF) approach: The Schrödinger equation $\hat{H}\Psi_i = \epsilon_i\Psi_i$ with \hat{H} being the Hamiltonian operator and ϵ_i denoting the i^{th} eigenenergy and Ψ_i denoting the i^{th} eigenfunction of \hat{H} can be reformulated in terms of DFT by simply exchanging \hat{H} for equation 2.5. Subtracting the right side leads to

$$\left(-\frac{1}{2}\nabla^2 + \hat{V}(\vec{r}) + \int \frac{n_0(\vec{r}')}{|\vec{r} - \vec{r}'|} d^3\vec{r}' + \hat{V}_{xc}[n_{0\downarrow}(\vec{r}), n_{0\uparrow}(\vec{r})] - \epsilon_i^{KS} \right) \phi_{i,KS}(\vec{r}) = 0. \quad (2.6)$$

The SCF scheme for DFT is illustrated in Figure 2.1. Once the density does not change more than a chosen threshold value between cycles, the calculation is considered converged and the final density is the ground-state density.[45] In practice, usually not the new density is used during the SCF-cycles but it is mixed with the previous one since this makes convergence easier.[43]

Now that we specified how the different parts can be obtained, we will discuss some of the pitfalls of KS DFT concerning the KS wave functions. As mentioned earlier, these are *non-interacting* single-particle wave functions. Strictly speaking, they do not have a direct physical meaning since they are an auxiliary systems which is lacking some vital information. The same can be said about their eigenenergies. On the other hand though, the sum over the squares of the $\phi_{i,KS}$ are the *exact* density which cannot be said about the orbitals of Hartree-Fock theory since these are lacking correlation and do not reproduce the exact density.[44] Despite the lack of a rigorous proof, in practice the KS orbitals have shown to be successfully used for qualitative molecular orbital analysis.[46, 47] In terms of KS eigenenergies, only the highest occupied molecular orbital (HOMO) has a meaning since the principle value of its eigenenergy equals minus the first ionization energy. This statement though is only true if the calculation was performed with the exact functional. In practice though results usually deviate quite a lot from the ionization energy due to the approximations made to V_{XC} . [44] In order to overcome this problem and obtain more reasonable ionization energies, in practice often a so-called "delta-SCF approach" is used. Therefore the total energy of the system and the total energy of the ionized system with the same external potentials are calculated and the difference can be interpreted as the first ionization energy.[48]

2.2 Forces and Relaxations

In this section we will describe the fundamental principles on which ab initio geometry relaxations are performed. While semi-empirical approaches are based on force-fields [49], ab initio methods focus on the calculation of forces through the Hellman-Feynman theorem.[50] The atomic structure is represented within $\hat{V}(\vec{r})$ and its determination will be the focus of this section.

One important part of electronic structure calculations is the determination of the atomic positions. This is not only of interest since the atomic structure is a vital part of the KS potential, but also since interesting conclusions can be drawn from these geometries (e.g. adsorption behaviour of molecules on surfaces). These quantities can be determined spectroscopically (e.g. via x-ray diffraction or neutron scattering) but if one wants to either predict structures or experimental data is simply not accessible it is favourable to have computational tools instead. Here, the total energy comes in handy: The ground-state atomic structure should be the one that leads to the lowest total energy. There are different ways to achieve this: for example, one could randomly assign spatial coordinates to atoms and calculate the total energy of each resulting structure, the one yielding the lowest total energy is then the ground-state configuration. This is a simplified explanation of the route which random search algorithms follow (in practice of course there is usually constraints that simplify the problem and can be taken advantage of, e.g. atoms have to have a minimum distance from each other).[51] As one can imagine, this is rather costly and even if one would find the ideal structure right away it can only be determined after a certain amount of structures have been calculated. On the other hand, if the amount of tested structure variations is big enough, one can be almost certain to have

found the *global* minimum and not have stranded in a local one. Since this problem is not unique to atomic structure optimizations but appears in many different disciplines ranging from economics to mathematics[52, 53], the field of global optimization and its algorithms is a whole world by itself[54, 55, 56] which we will not cover here. What we will focus on are the basic constraints that arise from physical laws which allow for an efficient optimization of the atomic positions with respect to the system's total energy. One of the most straightforward constraints in that respect is that nuclei should have a minimum distance from each other due to Coulomb repulsion and their finite size. On the other hand, the ground state by its nature is in equilibrium, meaning that the sum over all forces acting should be zero. In the following, we will focus on how the forces acting within the system can be calculated in the DFT framework.

The Hellman-Feynman forces, \vec{F}_i , can be expressed as a derivative of the total energy with the atomic positions being denoted by \vec{R}_i :

$$\vec{F}_i = -\frac{\partial E}{\partial \vec{R}_i} = -\int n(\vec{r}) \frac{\partial \hat{V}(\vec{r})}{\partial \vec{R}_i} d\vec{r} - \frac{\partial E_{II}}{\partial \vec{R}_i}. \quad (2.7)$$

Here E_{II} describes the nucleus-nucleus interactions which are described in a classical way and the first term contains a gradient of the external potential. In principle, a geometry optimization is converged once $-\frac{dE}{d\vec{R}_i} = 0$ for all nuclei i and the total energy E has reached a minimum.[42] In practice though, equation 2.7 contains some extra terms that do not vanish like in the ideal theoretical case. This is due to mainly two reasons: First of all, it is not possible to *perfectly* converge the density, there will always be some small oscillations and one has to set a threshold under which computation is stopped. Secondly, wave functions cannot be calculated analytically, so there is a need for a basis, and in practice this basis needs to be truncated at some point, so it is never complete. One way to deal with these so-called Pulay forces is to use a plane wave basis. This works especially well since unlike most other basis sets, plane-waves do not directly depend on the positions of the nuclei.[43]

However, with this force driven approach the initial guess of the atomic positions is crucial since this sets the starting point for the calculation. If the initial geometry is very far off from the global minimum the algorithm might not converge at all or converge to a local minimum that is close by.[43] Therefore it usually makes sense to perform a geometry optimization from different starting points to minimize the risk of confusing a local minimum for the global one.

2.3 XC Functionals

In this section we will discuss different approximations to the exact XC-functional and give an overview about the most common ones, namely the local density approximation (LDA or local spin-density approximation, LSD, for spin-polarized cases), generalized gradient approximated functionals (GGAs), hybrid functionals, self-interaction corrected functionals (SICs), +U functionals and functionals that can capture van der Waals inter-

2 Methods

actions. We will discuss strengths and pitfalls of the different types of methods. In 1965, shortly after their publication of the KS approach, Kohn and Sham made another ground-breaking contribution to DFT. This was not of a purely theoretical nature but consisted of the first approximation for the XC energy, the so-called local density approximation (LDA), paving DFT's way to the first actual calculations.[45] Local means that the XC term is evaluated at a position \vec{r} according to the *local* density at this point in space. One can rewrite the XC part $E_{XC}^{LDA}[n(\vec{r})]$ of the total energy as

$$E_{XC}^{LDA}[n(\vec{r})] = \int n(\vec{r})\epsilon_{XC}^{LDA}(n(\vec{r}))d^3\vec{r}. \quad (2.8)$$

This equals an average XC energy that is weighted by the probability of finding electrons at \vec{r} . [44] In LDA, $\epsilon_{XC}^{LDA}(n(\vec{r}))$ is approximated by the homogenous electron gas. In this model (also known as "jellium"[43]), electronic charge is moving in front of an average positive background, resulting in a density that is constant with respect to position \vec{r} . [44] The XC energy is then evaluated for the density of each point in space. As a consequence of this, the XC energy is no longer a functional but a function of the density. The homogenous electron gas is a common approximation for simple metals like sodium, but systems like molecules usually differ a lot from this picture. Nevertheless, LDA is the only approximation for which the exchange and correlation term can be written in an analytical form with very high accuracy. It is usually obtained from Quantum Monte Carlo calculations. There is however parametrizations different from that by Perdew and Zunger, but all approaches yield very similar results.[43] The per electron XC energy ϵ_{XC} (as parametrized by Perdew and Zunger[57]) takes the form

$$\epsilon_{XC} = -\frac{0.4582}{r_s} - \frac{0.1423}{1 + 1.0529\sqrt{r_s} + 0.3334r_s}, r_s \geq 1 \quad (2.9)$$

$$\epsilon_{XC} = -\frac{0.4582}{r_s} - 0.0480 + 0.0311\ln(r_s) - 0.0116r_s + 0.0020r_s\ln(r_s), r_s \leq 1, \quad (2.10)$$

with $r_s = \sqrt[3]{\frac{3}{4\pi n(\vec{r})}}$. [43] For a spin-polarized case, the so-called local spin density approximation (LSD) is used. Instead of considering the density of the system, the *spin densities* n^\uparrow and n^\downarrow are each considered to be mimicked by the homogeneous electron gas model.[42] However, in both LDA and LSD, there are some pitfalls: Firstly, the density in most systems is far from that of a homogenous electron gas. The correlation energy can vary rapidly with respect to the spatial coordinate if the density has a significant gradient.[43] Comparison of results obtained from Hartree-Fock calculations to LDA-level DFT show that the quality of LDA results is comparable or even superior to Hartree-Fock for molecules, despite the coarse jellium approximation in LDA[58, 43]. In the case of periodic systems, LDA clearly outperforms Hartree-Fock theory in terms of accuracy.[43] There are several reasons for this: On the one hand, this is due to error cancellation between the exchange and the correlation energy.[43, 42] On the other hand, it was shown by Gunnarson and Lundqvist that the homogeneous electron gas approximation holds pretty well in cases of slowly varying densities, which is usually not a good description of the densities of molecules but can be the dominating reason in other systems.[45] In contrast, LDA and LSD lead to a significant over binding when bond-breaking is calculated

by stretching a bond (for the H_2^+ molecule, the result obtained by LDA is two separate H atoms with half an electron each[59]).[43] Despite being the oldest approximation, LDA is still one of the most widely used XC functionals due to its low computational cost and relatively good results.

Another popular type of XC functionals (e.g. PBE) are based on a generalized gradient approximation (GGA). Here, instead of assuming that the density on which the calculation of the XC energy is based is uniform, an additional term containing the gradient of the density is included. The gradient contribution is only taken into account under a threshold value since high gradients would violate certain rules that the exact functional should have: The exchange-hole should be negative everywhere and the exchange and correlation holes should not contain fractional electronic charges. These constraints have to be enforced in this approximation, but when done so it yields more reasonable results for bond-stretching and other chemically relevant parameters.[44] Another class of XC functionals that is popular for predicting chemical properties are so-called hybrid functionals (examples: B3LYP, PBE0). These are based on an interpolation between two extremes: On the one hand, the exact exchange in a fully interacting system is known from Hartree-Fock theory. On the other hand, the exchange of a system of non-interacting particles is described by KS DFT. How these extrema are weighted though is empirical and finding the correct mixture of LDA which underestimates the band gap and Hartree-Fock which overestimates it is a sensitive topic.[60] It is also worth mentioning that computation of hybrids is more expensive than the previously mentioned methods since calculation of the exact exchange energy for the fully interacting system requires the use of a wave function method (Hartree-Fock).[45]

In addition to these basic approximations to the exact XC functional, there is extensions which can be used to improve results in situations where certain physical effects are more dominant. These include a self-interaction correction (SIC), the Hubbard +U correction[61] for strongly correlated systems or a van der Waals correction to improve the description of physisorption. Self-interaction is, as mentioned above, a problem that arises from the description of electron-electron interactions in terms of the density. This becomes especially obvious in the case of the hydrogen atom. Since H does only contain one electron, all electron-electron interactions should vanish, but for most functionals this is not the case (only for one Hybrid functional, BLYP, Koch and Holthausen found the self-interaction vanished[44]). This demonstrates how the approximations introduce unphysical contributions, but self-interaction of course is not limited to one-electron systems but is a side-effect of describing exchange and correlation in terms of the density. The bad news is that despite corrections having been introduced, they are quite controversial since they lead to orbital-dependent functionals[44] and, while giving improved results for atoms, can in the case of molecules yield worse results for reaction energies or molecular geometries than LDA.[62]

The "+U correction" originated from the problem that transition metal oxides were often found to be metals within LSD and GGA calculations, while indeed, they are Mott-insulators.[61] The origin of this problem lies in the over delocalization of valence electrons and in the resulting over stabilization of metallic ground-states.[63] This short-coming was tried to be overcome by adding an extra correlation term. The term is usually referred to as "+U" in the Hubbard model from which it originates.[45] The Hamiltonian of the

2 Methods

Hubbard model can be defined as

$$\hat{H}_{Hubbard} = t \sum_{\langle i,j \rangle, \sigma} (c_{i,\sigma}^\dagger c_{j,\sigma} + h.c.) + U \sum_i n_{i,\uparrow} n_{i,\downarrow}. \quad (2.11)$$

Here, t is the hopping amplitude, σ denotes the spin, $\langle i, j \rangle$ denote nearest neighbouring atomic sites, $c_{i,\sigma}^\dagger$ and $c_{j,\sigma}$ stand for the creation and annihilation operators, respectively, U is the Hubbard parameter mentioned above and $n_{i,\uparrow}$ and $n_{i,\downarrow}$ are electronic number operators for different spins.[63] Equation 2.11 can be understood in the following way: Assuming that the electrons are strongly localized, interactions are only accounted for when electrons are on the same site, which, in this picture, can be used synonymously with localized at the same atom. In this model though, the electrons are allowed to "hop" from one atom to a neighbouring one which is captured by the first term in equation 2.11 (an electron with spin σ is created at atom i and is annihilated at site j). This hopping takes place with a certain amplitude. The resulting interactions are proportional to the occupation number of this atom i (the more electrons, the more Coulomb repulsion). It is worth noting that both the hopping amplitude and the Hubbard U are at this point empirical parameters. If t is much smaller than U , it means that basically there is no hopping taking place since the repulsion between electrons is too large. The result are strongly localized electrons that are assigned to one atom. In contrary, if t is much larger than U , electrons can easily "hop" between neighbouring atoms and are rather delocalized. This is well described by the aforementioned standard DFT approximations.[63] The correction term is usually only applied to d- and f-type orbitals since the other electrons are well described with LDA and other methods. However, one needs to take into account that electronic interactions are already included in the underlying approximation (e.g. in the LDA XC-functional in the case of LDA+U). Therefore, technically there is some double counting which needs to be corrected. The total energy can be written as

$$E_{LDA+U}[n(\vec{r})] = E_{LDA}[n(\vec{r})] + E_{Hubbard}[o_{i,\sigma}(m)] - E_{doublecounting}[o_{i,\sigma}]. \quad (2.12)$$

It is worth noting that $E_{Hubbard}$ is a functional of the occupation numbers $o_{i,\sigma}(m)$ of the states m of an atom i while $E_{doublecounting}$ is a functional of the general, state-independent amount of electrons at an atom. The last term can hence be interpreted as a sort of mean field correction. In practice, the occupation of the states of an atom is often obtained through projection of the KS states onto an atomic basis. This projection is not unique and bears its very own problems of which some will be discussed in section 2.6. There is also no analytical description of $E_{doublecounting}$ so the outcome depends on the approximation one chooses. In general though, if the right parameters are chosen, the +U correction can be a very successful tool.[63]

Another common problem in popular XC functionals within DFT is their lack of accurate description of van der Waals (vdW) interactions. This stems from the local and semi-local approximations that are predominant in these common functionals, but vdW forces have a non-local component since they originate from induced dipole interactions and are present in areas of low density (in particular between molecules).[64] A common approach

is correcting the correlation part of the total energy by a non-local term:

$$E_C[n(\vec{r})] = E_C^{LDA}[n(\vec{r})] + E_C^{non-local}[n(\vec{r})]. \quad (2.13)$$

The first term resembles the correlation energy obtained from LDA while the correction term should approach zero in the local regime of $n(\vec{r})$. [64] The decay over long ranges r should follow a $\frac{1}{r^6}$ behaviour (Lennard Jones potential). Finding approximations that satisfy these criteria while remaining computationally efficient and feasible is a vital field of research. [65, 66] Approaches either do not only focus on corrections made to the correlation energy but also involve corrections applied to the potential V_{KS} . [66] The approximation which we used in this work is the so-called Grimme-d2 correction [67]. It is based on a correction to the energy and in order to meet the criteria mentioned above, a damping factor $f_{damping}(r_{ij})$ is applied:

$$E_C^{non-local}[n(\vec{r})] = -s_6 \sum_{i=1}^{N_{atoms}-1} \sum_{j=i+1}^{N_{atoms}} \frac{C_6(ij)}{r_{ij}^6} f_{damping}(r_{ij}). \quad (2.14)$$

In this equation, s_6 is a global scaling factor that is dependent on the XC functional one uses, i and j are the indexes of different atoms, $C_6(ij)$ denotes the dispersion coefficient of different atom pairs, N_{atoms} stands for the total number of atoms and r_{ij} is the corresponding interatomic distance of atom pair ij . [67] It is important that the damping factor leads to a decay that ensures that, on the one hand, long-range interactions are present, but on the other hand, double counting in short-range regions is avoided. As a damping factor, Grimme et al. proposed

$$f_{damping}(r_{ij}) = \frac{1}{1 + e^{-20(\frac{r_{ij}}{R_r} - 1)}}, \quad (2.15)$$

with R_r being the sum of atomic vdW radii. It is worth noting that C_6 is an empirical parameter. [67]

2.4 Pseudopotentials (PPs) versus All-Electron Calculations

In this section we will talk about the concept of PPs compared to all-electron calculations. We will give the reader an idea of what requirements a PP has to hold up to. Every description so far has included the full density and all KS states. When describing chemical properties, though, one is usually only interested in valence electrons since core levels are so low in energy that they usually do not participate in reactions. Core-regions also pose another problem: Wave functions usually have cusps close to the atom core which require bigger basis sets to describe. [45] Hence it would be beneficial to not just be able to neglect core-electrons but approximate the whole region close to the nucleus. When considering contributions like the kinetic energy that are calculated from the KS wave functions, reduction of the amount of states to take into account can dramatically

2 Methods

decrease the computational effort. The general idea underlying the development of PPs was the approximation that the core-electrons can be "frozen" (frozen core approximation) and remain unchanged.[43] Janak, however, showed that this is not necessarily true since these low-energy electrons can also be subject to significant changes depending on the chemical environment.[68] It took four years until von Barth and Gelatt showed that PPs are indeed a valid tool within electronic structure calculations.[69] Their argument was based on a separation of the valence density and the core density within the total energy functional and comparison of this result to a "frozen core functional". The difference of both total energies should then give the error one makes when using PPs (PPs):

$$\delta = E[n_{core}(\text{frozen core}), n_{valence}(\text{frozen core})] - E[n_{core}, n_{valence}]. \quad (2.16)$$

They could show that the PP approach yields results that differ less than 5% from all-electron calculations.[69] In today's electronic structure calculations, PPs are popular tools. The earlier PPs were constructed to reproduce experimental results like ionization potentials[43]. Modern PPs on the other hand are usually norm-conserving, meaning that they have to meet certain criteria. Unlike their predecessors, they are constructed to mimic the scattering of an atom of a certain type. Beyond that, they are required to

- 1) yield the same eigenenergies for the valence electrons as obtained from all-electron calculations.

- 2) result in the same wave functions as the ones obtained from all-electron calculations outside of a certain radius r_{core} around the atom core.

- 3) contain the same charge for $r > r_{core}$ as the real atom would (which is where the name "norm-conserving" comes from). [43]

The core-electrons are included in the external potential in that way that the Coulomb repulsion is mimicked in the potential. Due to the construction from scattering properties, PPs have minimum energy cut-offs in order to obtain valid results. This can easily be found by increasing the cut-off and checking for convergence of the result.[45] For some elements like transition metals, accuracy can be increased by inclusion of lower lying states as valence electrons. These are then referred to as "semi-core PPs". It is worth noting that one has to use a different PP for each angular momentum since it is not easy to find a function that ensures that states of different angular momentum are orthogonal to the core states. One of the downsides of norm-conserving PPs, however, is that they are relatively "hard", meaning that the wave functions resulting from these calculations still show features that require larger basis-sets (more on basis-sets: see section 2.5).[43] This was fixed by the construction of so-called "ultra-soft PPs". However, these are more complex and can sometimes contain unphysical core-like states (ghost-states).[45] Despite PPs strictly speaking, as a result of their construction, only being valid for isolated atoms[45], they have proven their worth and transferability to molecules and solids over the years in numerous calculations and have since become the work-horses of DFT making the calculation of large systems possible. Nevertheless, it is good practice to test a PP e.g. against results from an all-electron calculation to ensure that the approximation is valid for the system under study and it is important to only use PPs that have been generated with the same XC functional used for the calculations.

2.5 Basis Sets

This section is dedicated to the introduction of different basis-sets. We will talk about plane waves, local orbitals and real-space grids in particular. While plane waves are superior when it comes to periodic systems, local orbitals are usually the method of choice in quantum chemistry. The third category, real-space grids, can be easily applied to both fields and is a numerical solution of the problem of finding the correct wave function.

Finding an analytical function that represents the exact wave function is a daunting task. In theory, one would have to test an infinite amount of functions. In order to reduce the size of the problem, a basis set is chosen. This means that the exact wave function is expressed not in its analytical form but is approximated e.g. with a set of Gaussians.[44] One has to be aware that, in theory, only an infinitely large basis would yield the accurate result. In practice though, one needs to truncate the basis at a point that is sufficiently large to describe the wave function well enough.

One of the most common basis function types in condensed matter physics are plane waves. Plane waves are functions of the type $\frac{1}{V}e^{i(\vec{k}+\vec{G})r}$, with \vec{k} denoting the Bloch vector of a crystal, V representing the volume of the unit cell and \vec{G} standing for the reciprocal lattice vectors.[43] Their physical interpretation is the solutions of the Schrödinger equation of a free particle.[44] Due to the relationship between the momentum \vec{p} and the Bloch vector \vec{k} , which in free space is $\vec{p} = \hbar \vec{k}$, one can define a cut-off, E_{cut} , of the kinetic energy as

$$\frac{1}{2}|\vec{k} + \vec{G}|^2 \leq E_{cut}. \quad (2.17)$$

Due to the exponential character of plane waves, the basis functions are quite extended. This poses a problem in the description of low lying states which have complicated structures around the nuclei and require extensive basis sets. For this reason, plane-waves are usually only applied in combination with PPs.[43] Plane waves are strictly only designed for periodic systems but this can be circumvented by increasing the unit cell around a finite system so that it mimics vacuum.[43] This, on the other hand, can require very large unit cells which increases the computational cost. This is why plane waves are most popular in periodic systems and are rather unpopular in quantum chemistry.[44]

Most quantum chemistry basis sets are based on local orbitals. A very popular approach is the use of Gaussian type orbitals (GTOs), η_{GTO} , which can be described by

$$\eta_{GTO} = Nx^l y^m z^n e^{-\alpha r^2}. \quad (2.18)$$

Here, α is a sort of "damping factor" which determines how quickly a state decays over space. N makes sure that the GTO is normalized and the exponents l , m and n sum up to the angular momentum of a state. It is worth noting that, while plane-waves are orthonormal by construction[43], GTOs are normalized but not orthogonal.[44] There are extensions that make the use of this basis-set more efficient, namely contracted Gaussian functions (CGFs). For this, a subset of GTOs is used as a basis function and the Gaussians

within this subset can be linearly combined:

$$\eta_{CGF} = \sum_a^A d_\tau(a) \eta_{GTO}(a). \quad (2.19)$$

Here, η_{CGF} is a basis function constructed of a set of A GTOs (η_{GTO}) with coefficients d_τ for each GTO a .^[44] There is a variety of different basis-sets which are all more or less designed in this way. While the exact type of function in use might differ (some electronic structure codes like e.g. FHI-aims use an atomic orbital basis instead of some form of Gaussian function), all local orbital basis sets have in common that they are atom centred which requires additional effort when one wants to compute Hellman-Feynman forces (the so-called Pulay forces cancel out for plane waves due to their atom-independence, see section 2.2). On the other hand, local orbital basis sets have been designed for fast convergence in quantum chemistry and no more than a few tens of functions per atom are necessary to achieve this. In comparison, one would need about 250.000 plane waves to describe the unit cell of diamond, if no PP is used.^[43]

A totally different approach is that of real-space grids. While both plane waves and the local orbitals are centred around the idea of describing the wave function by a combination of analytical functions, real-space grids choose the opposite direction: Instead of defining basis functions, they "sample" the wave function at different points in space. Convergence is achieved if one has enough points to describe the function well enough. For the computation of integrals etc., numerical methods are required and technically speaking, the resulting wave function is not "smooth" since it consists of discrete points (which is not the case for the other methods). However, if enough points are chosen, interpolation will lead to the correct results. ^[43] In summary, the choice of basis set should be considered with the respective application in mind since all methods have their very own strengths and weaknesses.

2.6 Charge Partitioning Schemes

This section is focused on charge partitioning and its many pitfalls. While there are plenty of different approaches, each of them bears its own problems and limitations and it is important to take these into account when choosing a method.^[70, 71] We will give a quick overview over some of the most common schemes, namely the Hirshfeld analysis, Mulliken analysis, the Bader scheme and the projection of the density of states (pDOS) onto an atomic orbital basis.

When analysing phenomena like charge-transfer (CT), one is usually not only interested in the amount of electrons being transferred but also in the participation of different parts of the system within the process. While the amount of charge being transferred can easily be determined via integration over the density of the region in which the acceptor is located, this does neither give insight on the origin of the CT nor on the resulting charge-distribution of the acceptor. Another prominent example of the importance of charge-partitioning is the question if a part of a molecule is prone to electrophilic or

nucleophilic attacks (e.g. consider the Umpolung of CO_2 upon activation)[4]. In these cases, the density clearly does not contain enough information and the shape of the KS orbitals is more of a qualitative measure than an analytical result.[46, 47] In order to resolve this dilemma, several schemes have been established over the years.[71]

One of the most famous approaches has been established by Mulliken. It is predominantly used in methods that use a linear combination of atomic orbitals as their basis set. For other basis-set types, it is possible to perform a basis-transformation by e.g. projecting the density of states (DOS) onto e.g. an atomic basis. The partial charge q of each atom i can then be derived from the coefficients c_j of each molecular orbital ϕ_k 's basis functions χ_j with $\phi_k = \sum c_j \chi_j$.

$$q_i = Q_0(i) - Q(k) \quad (2.20)$$

describes the resulting charge of atom i with $Q_0(i)$ standing for the number of electrons of the neutral, isolated atom i in its ground-state, $Q(k)$ denoting the amount of electrons found on atom i through summation of the coefficients.[72] While this approach is fairly straightforward, it has the downside that it depends on the choice of basis functions. More atomic orbitals do not necessarily lead to a "more accurate" result since those functions might be more delocalized and there will be overlap with other atoms. This overlap is usually evenly split between participating atoms but if this term gets very large, results are usually unphysical.[71]

Another method that follows a similar approach is the Hirshfeld charge-partitioning scheme. Here, one starts from a "pro-molecule". This describes a construct of atoms with spherically averaged ground-state densities. These are arranged in a way that the nuclei are positioned at the same coordinates as those of the real molecule. Regions of overlap are, unlike in the Mulliken approach, not "equally shared" between participating atoms but with respect to their contribution evaluated through the overlap of the pro-molecule. The density of the pro-molecule can then be expressed as $n_{pro}(\vec{r}) = \sum_i n_i(\vec{r})$ and the sharing function $w_i(r)$ can be written as

$$w_i(\vec{r}) = \frac{n_i(\vec{r})}{n_{pro}(\vec{r})}. \quad (2.21)$$

The resulting atomic charge Q_i of atom i can then be expressed via integration of the deformation density $\delta n_i(\vec{r})$:

$$Q_i = - \int \delta n_i(\vec{r}) d^3 \vec{r} = - \int w_i(\vec{r}) (n_{mol}(\vec{r}) - n_i(\vec{r})) d^3 \vec{r}. \quad (2.22)$$

It is also possible to directly integrate over the molecular density $\rho_{mol}(\vec{r})$ multiplied with the sharing function for atom i to obtain Q_i , but since this quantity varies more rapidly, it is numerically easier to use equation 2.22 instead.[73] While this method yields excellent results for ground-state atomic charges[71], it is to be taken with a grain of salt for excited states[70]. This can be explained by the construction of the pro-molecule from atomic ground-state densities: At higher excitation energies, the density might get deformed in a way that reaches outside of the pro-molecule. In this case, one would be blind to these electrons. Checking for this on the other hand is fairly easy since the sum of the partial charges should, by construction, yield the amount of electrons in the system. If this is

2 Methods

Method	charge on C [e]	charge on O (average) [e]
Hirshfeld	+0.3	-0.2
Mulliken	+0.4	-0.2
Bader (without PP)	+2.1	-0.9
Bader (with PP)	+4.0	-2.0

Table 2.1: Results of a partial charge analysis for a linear CO₂ molecule in gas phase at 0 K. The Bader analysis was performed on a density obtained through Octopus and Hartwigsen Goedecker Hutter LDA PPs, as well as on a density obtained from an all electron calculation with FHIaims. For better comparison, a Mulliken analysis was performed using FHI-aims and a Hirshfeld scheme using Octopus and only the deviation from the neutral atom's charge is displayed.

not the case any more and one is well below the first ionization energy, it is clear that the Hirshfeld approach cannot be used for this case since the result is unphysical through the constraint of the pro-molecule.

In 1971, Bader developed a scheme that was independent of atomic densities, wave functions and basis-sets. He defined basins over which he then integrated the density. The border of a basin is defined as the points where the gradient of the density is equal to zero.[74] While this approach is quite elegant since it only requires the density and there is no arbitrariness within it, it poses a huge problem for the use with PPs. Due to the PP's additional repulsion to mimic the Coulomb repulsion from the lower lying electrons and the resulting construction that the wave functions decay before the core-region, there is a "hole" in the density at the nuclei positions. This can lead to oddities in the gradient which then result in unphysical results. Bader analysis is not only problematic in combination with PPs but is also known to yield too extreme values which indicate a structure's components to be more ionic than they actually are.[71]

If one calculates the partial charges of a simple CO₂ molecule using a Hirshfeld, a Mulliken and a Bader scheme with and without PPs, the results (Table 2.1) are quite telling: In table 2.1, we calculated the charge distribution in a linear CO₂ molecule with the different schemes. Apparently, the size of basis set for the Mulliken analysis in this case was sufficient since it agrees rather well with the Hirshfeld result. While all different charge-partitioning methods seem to capture the total amount of electrons rather well ($2 * q(\text{oxygen}) + q(\text{carbon}) \approx 0$, deviations from this might seem more prominent due to rounding) and the general picture that the carbon atom is positively charged while the oxygen atoms bear a partial negative charge is consensus among all different methods, this is about it when it comes to similarities. The most extreme values can be observed for the Bader analysis with PPs which results in an even distribution of *all* valence electrons of the carbon atom among the oxygens. According to this picture, CO₂ would be a salt which is clearly not the case. The results from the Bader analysis with the density of an all-electron calculation are less extreme but still indicate that the carbon atom donates more than two of its electrons to the neighbouring oxygen atoms. On the other hand, the Hirshfeld and Mulliken charges show much smaller partial charges of +0.3 e and +0.4 e, respectively. These values are in very good agreement with one another and literature.[4]

One of the upsides of the Mulliken analysis over the schemes developed by Bader and Hirshfeld however is that, since it is not based on the density but on atomic orbitals, the charge analysis can be resolved with respect to the angular momentum. Guerra et al. go as far as to claim that Mulliken analysis is useless due to its heavy basis set dependence[71], but when used with caution, it can yield reasonable qualitative results.[72]

2.7 Time-dependent Density Functional Theory (TDDFT)

While the section 2.1 was concerned with the fundamentals of ground-state DFT, if one wants to calculate excited state properties there is certain extensions to the theory that need to be made. This section will start by introducing the most fundamental basis of time-dependent density functional theory (TDDFT) which is the Runge-Gross theorem. We will then continue to talk about different TDDFT XC-functionals (ALDA, memory kernels) and their strengths and weaknesses. We will finish by talking about light-electron coupling and discuss two of the most common approaches to handle this phenomenon which are real-time propagations and the solution of Casida's equation. To illustrate some interesting aspects of relevance to our work we will explain how absorption spectra are obtained from both methods.

The basis of excited-state calculations is the time-dependent Schrödinger equation,

$$i\frac{\partial}{\partial t}|\Psi(t)\rangle = \hat{H}(t)|\Psi(t)\rangle, \quad (2.23)$$

with $\Psi(t)$ denoting the many-body wave function and t equalling time. For DFT, Hohenberg and Kohn laid the foundation, their reasoning though was strictly constrained to the ground-state. One of the key pillars of the proof underlying the Hohenberg-Kohn theorem was the argument that the ground-state is associated with the lowest total energy possible. In a perturbed system, however, this does not hold any more. If the system is not just initially perturbed but is driven by an electromagnetic field, the total energy of the system even changes over time. However, instead of focusing on the energy, one can utilize the so-called quantum mechanical action $A[\Psi(t)]$. The quantum mechanical action is defined as

$$A[\Psi(t)] = \int_{t_0}^{t_1} \langle \Psi^*(t) | i\frac{\partial}{\partial t} - \hat{H}(t) | \Psi(t) \rangle dt. \quad (2.24)$$

The wave function Ψ that results in a stationary point of the quantum mechanical action ($A[\Psi(t)] = 0$) is the solution of the time-dependent Schrödinger equation (equation 2.23). While the static Schrödinger equation is a second order differential equation (with respect to the spatial coordinates), the time-dependent Schrödinger equation is of first order (with respect to the time). This has some further implications: The static Schrödinger equation is a boundary value problem (one wants to find the *minimum* energy), but for the time-dependent case, the solution also depends on the initial state of the system.[42]

The Hohenberg-Kohn theorem proofed the bijectivity of the external potential $V(\vec{r})$ and

2 Methods

the density $n(\vec{r})$. The Runge-Gross theorem, in contrast, shows that if two potentials are truly different, meaning that $V(\vec{r}, t) \neq V'(\vec{r}, t) + c(t)$ with $c(t)$ being a time-dependent function, they cannot lead to the same density $n(r, t)$. The proof utilized a Taylor expansion of the potential with respect to the initial time t_0 . As long as this can be done, the Runge-Gross theorem holds and there is a one-to-one mapping between $n(\vec{r}, t)$ and $V(\vec{r}, t)$ for a given initial state Ψ_0 . [42]

One of the most common XC functionals in TDDFT is the adiabatic local density approximation (ALDA). It is the time-dependent analogy to LDA and can be expressed as

$$\hat{V}_{XC}^{ALDA}(\vec{r}, t) = \hat{V}_{XC}^{HEG}(n)|_{n=n(\vec{r}, t)}, \quad (2.25)$$

with $\hat{V}_{XC}^{HEG}(n)$ denoting the XC potential of the homogeneous electron gas of density n . The general idea behind this is to use the same approximations that have been developed for DFT and simply "re-evaluate" the functional for each different density. This can also be utilized to use other DFT functionals in time-dependent calculations. It is worth noting though that ALDA of course does not fix the problems of LDA and hence suffers from the same wrong asymptotic decay of the density (in a neutral finite system, it should decay with $\frac{1}{r}$, indeed though it decays exponentially), as well as the other shortcomings mentioned above (see section 2.3). [42] As a result of this rapid decay of the density, local XC functionals are less attractive at long ranges than the exact functional would be. [44] This underestimation of the attractive character can lead to quite dramatic overestimations of excitation energies. [42] Even when the approximation fails (like e.g. in the case of CT excitations), there is usually still conditions under which useful information can be extracted nevertheless. [75]

Time-dependent functionals that are derived in this way only depend on the density at t . The exact functional, however, should have some sort of "memory", meaning that previous points in time, t' , are relevant to the system's current state.

In order to obtain the density at t , the initial KS wave functions of the system (initial here refers to $t = t_0$ which, in most cases, will be the ground-state) can be propagated for a finite time t_f . Therefore, the initial KS states are acted upon with a time-evolution operator $\hat{U}(t_f, t_0)$:

$$\phi_i(\vec{r}, t_f) = \hat{U}(t_f, t_0)\phi_i(\vec{r}, t_0). \quad (2.26)$$

The time-evolution operator $\hat{U}(t_f, t_0)$ can be defined in terms of the time-dependent KS Hamiltonian, the Keldysh pseudo-time, τ , and a time-ordering operator \hat{T} :

$$\hat{U}(t', t) = \hat{T}e^{-i\int_t^{t'} \hat{H}_{KS}(\tau)d\tau}. \quad (2.27)$$

There is a need for approximations to the exponential in equation 2.27. In addition, it is beneficial to split the propagation time into smaller intervals Δt (often referred to as "time-steps") in order to reduce the total error within the propagation. A simple direct expansion in a power series of δt , unfortunately, results in not normalized KS wave functions and hence an unstable propagation. One of the most common solutions to this

problem is the so-called Crank-Nicholson scheme. This facilitates the fact that a state at t can either be reached by propagating the state at $t - \Delta t$ forward in time or by a backwards propagation from $t + \Delta t$. The time-dependent KS wave functions can then be rewritten as

$$\phi(t + \frac{\Delta t}{2}) = \hat{U}(t + \frac{\Delta t}{2}, t)\phi(t) \quad (2.28)$$

$$= \hat{U}(t - \frac{\Delta t}{2}, t + \Delta t)\phi(t + \Delta t). \quad (2.29)$$

With $\hat{U}^{-1}(t + \Delta t, t) = \hat{U}(t - \Delta t, t)$, it follows that

$$\phi(t + \Delta t) = \hat{U}(t + \frac{\Delta t}{2}, t + \Delta t)\hat{U}(t + \frac{\Delta t}{2}, t)\phi(t). \quad (2.30)$$

In a first step, a first guess for the KS wave functions at $t + \delta t$ is made by e.g. a third or fourth order direct expansion of the exponential in equation 2.27 with δt in order to obtain an estimate for \hat{U} . This is a poor approximation but is sufficient to construct $\hat{H}(t + \delta t)$ and $\hat{U}(t + \frac{\delta t}{2}, t + \delta t)$. Using these again to obtain the time-dependent KS wave functions with equation 2.30 yields stable propagations and reasonably good results.[42] One common time-dependent problem is the response of a system to an external electromagnetic field. For a constant electric field, $V_{electric}(\vec{r}, t) = eE(t)\vec{r}$, the electron-light coupling can be described by

$$i\frac{\partial}{\partial t}|\Psi(t)\rangle = [\hat{H}(t) + V_{electric}(t)]|\Psi(t)\rangle. \quad (2.31)$$

[76] When calculating absorption spectra, instead of using a "regular" electric field, a delta pulse, $V_{pulse}(\vec{r}, t) = -k_0\vec{s}_v\delta(t)$, is applied to the ground-state wave functions at $t = 0$. Here, \vec{s}_v denotes three orthogonal vectors in space (e.g. x,y,z) and k_0 is the amplitude which should be chosen sufficiently small in order to ensure a linear and dipolar behaviour of the system. This is an elegant mathematical trick: Since a delta-perturbation can be written as an infinite sum over sines, basically all possible frequencies ω get excited at the same time. When propagating this perturbed state, the density will move. This displacement of negative charge against the positively charged nuclei is a dipole moment. Fourier transformation of this yields the dynamical polarisability, $\alpha(t)$, whose imaginary part \Im is proportional to the photo-absorption cross-section, σ , according to

$$\sigma(\omega) = \frac{4\pi\omega}{c} \cdot \frac{1}{3}\Im \sum_{v=x,y,z} \alpha_v(\omega), \quad (2.32)$$

with c denoting the vacuum speed of light. The factor of $\frac{1}{3}$ in combination with the spatial dependence of $\alpha_v(\omega)$ produces a spatially averaged response.[42]

Another way of obtaining excitation spectra is through linear response theory. For perturbations, the density can be expanded in a series of the form

$$n(\vec{r}, t) = n^{(0)}(\vec{r}) + n^{(1)}(\vec{r}, t) + n^{(2)}(\vec{r}, t) + n^{(3)}(\vec{r}, t) \dots, \quad (2.33)$$

in which $n^{(0)}(\vec{r})$ denotes the unperturbed ground-state density. If the perturbation $v^{(1)}$

2 Methods

is small, the expression can be truncated after the linear term $n^{(1)}(\vec{r}, t)$. The time-dependent density can then be rewritten in terms of the density-density response function χ as

$$n(\vec{r}, \omega) = n^{(0)}(\vec{r}) + \int \chi(\vec{r}, \vec{r}', \omega) v^{(1)}(\vec{r}', \omega) d\vec{r}'. \quad (2.34)$$

Here, \vec{r}^j denotes the spacial coordinates of density. For the KS approach, χ_{KS} is much easier to calculate since the electrons are non-interacting. It can be written as

$$\chi_{KS}(\vec{r}, \vec{r}', \omega) = \lim_{\eta \rightarrow 0^+} \sum_{jk}^{\infty} (f_k - f_j) \frac{\phi_j(\vec{r}) \phi_j(\vec{r}') \phi_k^*(\vec{r}) \phi_k^*(\vec{r}')}{\omega - (\epsilon_j - \epsilon_k) + i\eta}, \quad (2.35)$$

in which f_k denotes the occupation number and ϵ_k is the eigenvalue of the k^{th} KS ground-state orbital.[42] η stands for a positive infinitesimal which enforces the adiabatic approximation (meaning that the system varies slowly over time)[77] and 0^+ denotes the time at which the perturbation occurs. It is worth noting that only excitations between occupied ($f = 1$) and unoccupied KS orbitals ($f = 0$) contribute to the density-density response since all other contributions cancel out. The excitation energies of the system can be found at the poles of the polarisability. The time-dependent KS potential in the linear expansion can be expressed as

$$\hat{V}_{KS}^{(1)}(\vec{r}, t) = \hat{V}_{ext}^{(1)}(\vec{r}, t) + \hat{V}_{Hartree}^{(1)}(\vec{r}, t) + \hat{V}_{XC}(\vec{r}, t), \quad (2.36)$$

with $\hat{V}_{Hartree}^{(1)}(\vec{r}, t) = \int \frac{n^{(1)}(\vec{r}', t)}{|\vec{r} - \vec{r}'|} d\vec{r}'$ and

$$\hat{V}_{XC}(\vec{r}, t) = \int \int \frac{\delta \hat{V}_{XC}(\vec{r}, t)}{\delta n(\vec{r}', t')} n^{(1)}(\vec{r}', t') d^3\vec{r}' dt'. \quad (2.37)$$

The term $\frac{\delta \hat{V}_{XC}(\vec{r}, t)}{\delta n(\vec{r}', t')}$ in equation 2.37 is often referred to as XC kernel, $f_{XC}(\vec{r}t, \vec{r}'t')$, and, in the spirit of DFT, contains everything that is unknown. The approximation to the kernel used in this thesis is the ALDA XC kernel, $f_{XC}^{ALDA}(\vec{r}t, \vec{r}'t')$, which can be defined as

$$f_{XC}^{ALDA}(\vec{r}t, \vec{r}'t') = \delta(\vec{r} - \vec{r}') \delta(t - t') f_{XC}^{HEG}(n)|_{n=n(\vec{r}, t)} \quad (2.38)$$

with $f_{XC}^{HEG}(n) = \frac{d\hat{V}_{XC}^{HEG}(n)}{dn}$. It is worth noting that equation 2.38 is local in time and space but despite this rather simplistic approximation, it performs surprisingly well. [42]

A common way of finding the poles of the density-density response function is through the Casida formalism which turns the search into a pseudo-eigenvalue problem:

$$\begin{bmatrix} A & B \\ -B & -A \end{bmatrix} \begin{bmatrix} X^I \\ Y^I \end{bmatrix} = \hbar\omega_I \begin{bmatrix} X^I \\ Y^I \end{bmatrix} \quad (2.39)$$

Here ω_I denotes the excitation energy of the I^{th} excitation, X^I and Y^I are the Casida matrix eigenvectors and the matrix elements A and B are given by

$$A_{vcv'c'} = \delta_{v'v} \delta_{c'c} (\epsilon_c - \epsilon_v) + K_{vc, v'c'}^{H(XC)} \quad (2.40)$$

and

$$B = K_{vc,v'c'}^{H(XC)}, \quad (2.41)$$

respectively. The superscript v here denotes an unoccupied state and c stands for occupied orbitals. $K_{vc,v'c'}^{H(XC)}$ is given by

$$K_{vc,v'c'}^{H(XC)}(\omega) = \int \int \phi_v(\vec{r}) \phi_c(\vec{r}') \left(\frac{1}{|\vec{r} - \vec{r}'|} + f_{XC}(\vec{r}, \vec{r}', \omega) \right) \phi_{v'}(\vec{r}') \phi_{c'}(\vec{r}) d\vec{r} d\vec{r}' \quad (2.42)$$

and describes the Coulomb interactions (e.g. electron-hole attraction), so for $K_{vc,v'c'}^{H(XC)}(\omega) = 0$, the excitation energy is the eigenvalue difference of the KS wave functions.[78] The excitation energies that are obtained from solving equation 2.39 are exact. In practice though they suffer from the approximations made, namely the approximation to the XC functional which results in an inaccurate KS ground-state and the approximated frequency dependent XC kernel. Under the assumption that the KS orbitals are real and f_{XC} is independent of the frequency (which is only true within the adiabatic approximation), the A and B become real. The equation 2.39 can be simplified to

$$CF_I = \omega_I^2 F_I \quad (2.43)$$

with $F = \sqrt{A - B}(X - Y)$ and

$$C(vcv'c') = \delta_{vcv'c'} \omega_{vc}^2 + 2\sqrt{(\epsilon_v - \epsilon_c)(\epsilon'_v - \epsilon'_c)} K_{vc,v'c'}^{H(XC)}. \quad (2.44)$$

[77, 78, 79] The excitation energies and Casida matrix eigenvector elements can be obtained through diagonalization of C . The oscillator strength f of excitation I can be obtained via

$$f_I = \frac{2}{3} (|\vec{\mu}_x S^{-1/2} F_I|^2 + |\vec{\mu}_y S^{-1/2} F_I|^2 + |\vec{\mu}_z S^{-1/2} F_I|^2), \quad (2.45)$$

in which the factor 2 originates from the different spin-channels, the factor of 1/3 forms the spatial average, $\vec{\mu}_x$, $\vec{\mu}_y$ and $\vec{\mu}_z$ denote the dipole moments in x , y and z direction and $S = \frac{-\delta_{vc}\delta_{v'c'}}{(f_c - f_v)(\epsilon_c - \epsilon_v)}$. [77] The spectrum can then be obtained by broadening the oscillator strengths. For a complete basis, $\sum_I F_I F_I^\dagger = 1$. In practice, this can be used as a test criterium to check if enough unoccupied states have been included. For Casida calculations usually a large number of empty states is required to achieve full convergence which makes it scale worse with electron number than time-propagations.[42] The excited state Ψ_I can be approximated by $\sum_{cv}^{f_c - f_v > 0} C_{cv}(I) \hat{a}_v^\dagger \hat{a}_c \Phi_0$ with the ground state Φ_0 and the coefficients $C_{cv}(I) = \sqrt{\frac{\epsilon_v - \epsilon_c}{\omega_I}} F_{cv}(I)$. This allows for qualitative assignment of the excited state wave function. This is basically a configuration interaction picture which is popular in quantum chemistry: Ψ_I is a singly excited configuration which consists of the coefficient weighted KS orbitals.[77] If one wants exact excitation energies and band-gaps, many-body perturbation theory (e.g. the GW approximation or Bethe Salpeter equations)[80] or more complex hybrid functionals and meta-GGAs can be used.[81] Although being much more expensive in terms of computational effort, the quality of the results justifies this.[42]

3 Results and Discussion

In this chapter we will present the findings of our research and discuss their implications. The first part (section 3.1) is focused on the atomic structure and carbon dioxide adsorption behaviour of different systems. We relaxed icosahedral aluminium clusters with a variety of dopants and studied their capability of adsorbing and activating CO_2 . For the smallest clusters, $[\text{Al}_{12}M]$ (with M denoting the dopant), we studied dopants with and without d-electrons. We also considered singly negatively charged clusters $[\text{Al}_{12}M]^-$. From this pool of candidate systems we selected the neutral clusters which led to the smallest adsorption distances, which were the Zr, Mn, Fe, Ru, Co, Ni and Cu doped systems. We then relaxed the geometries of these systems with one and two more cluster shells and CO_2 placed in the proximity of the dopant which is always located in the outer shell in our studies.

The other parts (sections 3.2, 3.3 and 3.4) give insights into the electronic structure of these systems and their excited state properties. We start with the smallest clusters $[\text{Al}_{12}M]$ in section 3.2 on which we test and establish some general methods (e.g. we test whether a Hubbard+U[61] correction must be included and justify our analysis of light-induced charge-transfer). We perform the same calculations which we found to be of relevance to the smaller clusters on the medium-sized systems, $[\text{Al}_{54}M]-\text{CO}_2$ (section 3.3). All ground-state calculations (if possible) are repeated for the largest clusters in our study (section 3.4), $[\text{Al}_{147}M]-\text{CO}_2$. Based on these results, the size-dependence of CO_2 adsorption and activation is discussed and general trends are highlighted.

3.1 Relaxed Structures of $[\text{Al}_{12}M]$, $[\text{Al}_{54}M]$ and $[\text{Al}_{146}M]$ Aluminium Clusters with CO_2

In this section we discuss the structures obtained through geometry relaxations with special focus on their ability of adsorbing carbon dioxide. We will display results for different metallicly and organically doped small aluminium clusters, both neutral or singly negatively charged. We will also present results for selected medium and large sized neutral clusters ($[\text{Al}_{54}M]-\text{CO}_2$ and $[\text{Al}_{147}M]-\text{CO}_2$). Our main emphasis in this chapter lies on CO_2 adsorption distances and the O-C-O angles.

$[\text{Al}_{13}]^-$ is especially of interest due to its high stability, perfect icosahedral geometry and the fact that it can be synthesized. Additionally, it has been shown that surface plasmon-like transitions can be found.[82] However, it is not clear if these can be excited since their energies lie well above the first ionization energy. In our studies we only saw

3 Results and Discussion

comparably large CO₂ adsorption distances for both the [Al₁₃] and the [Al₁₃]⁻ cluster. As a consequence, we decided to exchange one of the outer atoms of the original pure Al cluster for a dopant to serve as an anchor.

System	Adsorption Distance [Å]	O-C-O Angle[°]
[Al ₁₃]-CO ₂	3.6 (C-Al)	177.7
([Al ₁₃]-CO ₂) ⁻	3.6 (C-Al)	177.7
[Al ₁₂ H]-CO ₂	2.9 (O-H)	179.4
([Al ₁₂ H]-CO ₂) ⁻	2.9 (C-H)	177.5
[Al ₁₂ B]-CO ₂	3.2 (C-B)	178.8
([Al ₁₂ B]-CO ₂) ⁻	3.3 (C-B)	177.1
[Al ₁₂ C]-CO ₂	3.1 (C-C)	178.6
([Al ₁₂ C]-CO ₂) ⁻	3.3 (C-C)	177.7
[Al ₁₂ Si]-CO ₂	3.5 (C-Si)	179.5
([Al ₁₂ Si]-CO ₂) ⁻	3.4 (C-Si)	175.6
[Al ₁₂ N]-CO ₂	3.0 (C-N)	179.1
([Al ₁₂ N]-CO ₂) ⁻	3.1 (C-N)	177.7
[Al ₁₂ P]-CO ₂	3.4 (C-P)	179.0
([Al ₁₂ P]-CO ₂) ⁻	3.3 (C-P)	175.8
[Al ₁₂ O]-CO ₂	3.3 (C-O)	179.8
([Al ₁₂ O]-CO ₂) ⁻	3.4 (C-O)	178.7
[Al ₁₂ S]-CO ₂	3.3 (C-S)	179.3
([Al ₁₂ S]-CO ₂) ⁻	3.3 (C-S)	177.8

Table 3.1: Structural data for the relaxed [Al₁₂M] and ([Al₁₂M])⁻ clusters with d-electron free dopants and adsorbed CO₂. The adsorption distance is measured as the minimum distance that can be found between any molecular and any cluster atom. The information given in the brackets refers to the atoms between which this distance is measured. The third column shows the O-C-O angle in degree.

For further details on how these structures were obtained, please refer to **chapter 5 "Computational Details"**. The results of our geometry optimizations are displayed in Tables 3.1 and 3.2. We analysed the lowest energy structures with respect to their adsorption distance, O-C-O angle and the atoms between which adsorption is taking place. Adsorption distance was defined as the smallest distance that could be found between any cluster atom and any atom of the CO₂ molecule. The dopants without d-electrons are Al, B, C, H, N, O, P, S and Si. As d-metal dopants we considered Zr, Mn, Fe, Ru, Co, Ni, Cu, Ti, Pd, Rh, Ag and Au.

For the neutral clusters doped with elements that do not contain d-electrons in their valence shell (Table 3.1), adsorption distances range from 2.9 Å (found in the H-doped cluster) to 3.6 Å for the un-doped [Al₁₃] cluster. This shows that doping improves CO₂ adsorption significantly. The Si and P doped clusters exhibit larger adsorption distances than the other doped systems which show adsorption distances between 3.0 Å in the case of the N-doped cluster and 3.3 Å which is found for O and S as dopants. Adsorption in

3.1 Relaxed Structures of $[Al_{12}M]$, $[Al_{54}M]$ and $[Al_{146}M]$ Aluminium Clusters with CO_2

all cases except for one is occurring between the carbon atom of CO_2 and the dopant. In the differing case, $[Al_{12}H]$, the carbon dioxide molecule adsorbs to the dopant with one of its oxygen atoms. Here it is worth noting though that CO_2 does not clearly coordinate to the cluster with one of its oxygen atoms but appears to be rather perpendicular with its molecular axes to the cluster surface. The distance between the oxygen atom and hydrogen is only slightly smaller than the one between the carbon atom and hydrogen. Adsorption angles are very close to 180° , corresponding to the geometry of a neutral isolated CO_2 molecule.

Similar trends are found for the negatively charged clusters doped with elements that do not contain d-electrons (Table 3.1). Adsorption distances are 0.1 to 0.2 Å smaller in all cases than those of the neutral clusters. The only exceptions are the Al, H and S doped clusters. For those, the adsorption distances are the same as for the neutral systems. Adsorption angles of the negatively charged clusters without d-electrons are always smaller than those of their neutral counterparts without any exception. This could be explained by the excess charge of the cluster which is, although very slightly due to the rather large adsorption distances, delocalized over the CO_2 molecule which is known to bend under charge-transfer[4]. This bending is very small though due to the presumably small charge-transfer. The angle that differs the most from 180° can be observed for the negatively charged Si doped cluster with an O-C-O angle of 175.6° followed by the negatively charged P-doped cluster which exhibits an O-C-O angle of 175.8° . Adsorption between the negatively charged, non-transition metal doped clusters occurs between the carbon atom and the dopant in all cases.

The resulting structures after the geometry relaxations of the neutral and singly negatively charged clusters without d-electrons are displayed in figures 3.1 and 3.2.

It can be seen that most clusters deviate from the geometry of a perfect icosahedron. Especially the clusters in $[Al_{12}H]-CO_2$, $([Al_{12}H]-CO_2)^-$, $[Al_{12}B]-CO_2$, $[Al_{12}C]-CO_2$, $([Al_{12}C]-CO_2)^-$, $[Al_{12}N]-CO_2$, $([Al_{12}N]-CO_2)^-$, $[Al_{12}O]-CO_2$, $([Al_{12}O]-CO_2)^-$ and $([Al_{12}S]-CO_2)^-$ show strong distortions. On the other hand, the clusters in $([Al_{13}]-CO_2)^-$, $([Al_{12}B]-CO_2)^-$, $[Al_{12}Si]-CO_2$, $([Al_{12}Si]-CO_2)^-$ and $[Al_{12}S]-CO_2$ exhibit almost perfect icosahedral geometry. For $[Al_{13}]^-$ this is usually explained by its 40 valence electrons which result in a closed shell according to the jellium model.[82] However, this does clearly not apply to all icosahedral clusters from figures 3.1 and 3.2. Only $([Al_{13}]-CO_2)^-$, $[Al_{12}B]-CO_2$ and $[Al_{12}Si]-CO_2$ contain a total of 40 valence electrons and, at the same time, exhibit the structure of an almost perfect icosahedron. On the other hand, $[Al_{12}C]-CO_2$ also contains exactly 40 valence electrons but appears to be one of the most distorted clusters with the Al atom at the bottom not aligning with the axis formed by the central Al atom and the dopant. This is surprising since it has been shown that full jellium cluster shells are associated with high symmetry arrangements of the atoms[83].

For the d-metal-doped clusters (Table 3.2), adsorption distances cover a wider range, falling between 1.8 Å ($M = Mn, Co$) and 3.4 Å ($M = Au$) for neutral clusters and 1.9 Å ($M = Co, Ni$) and 3.5 Å ($M = Mn$) for negatively charged clusters. Here it is worth noting that one of the smallest adsorption distances is observed for the neutral Mn-doped cluster, while its negative counterpart has the largest adsorption distance of all d-metal-

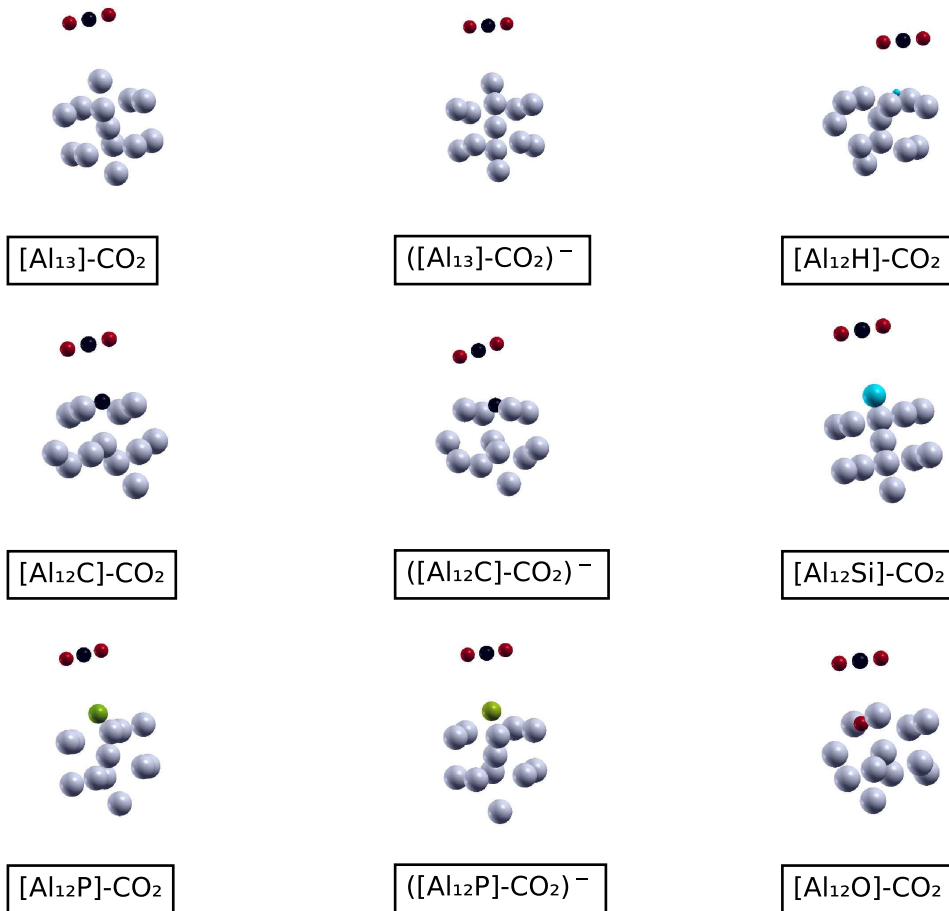


Figure 3.1: Relaxed structures of the d-metal-free $[Al_{12}M]-CO_2$ and $([Al_{12}M]-CO_2)^-$ systems (part 1). Atom colours: Grey = aluminium, black = carbon, red = oxygen, other = dopant.

doped systems. As for the neutral d-metal-doped clusters, adsorption of CO_2 via one of its oxygens is far more prevalent than for the non-d-metal-doped clusters (7 out of 12 cases). This trend can also be observed for the negatively charged d-metal-doped clusters, nevertheless it is rarer (5 out of 12 cases). The latter can be explained by the negative partial charge of the oxygen atom which is less prone to be in the direct vicinity of the negative charges on the cluster, although the presence of the d-metal seems to be able to compensate for this in some cases.

The most striking difference between the d-metal-doped and non-d-metal-doped systems lies in the adsorption angles. For the neutral clusters, these range from 131.4° ($M = Zr$) to 179.7° ($M = Fe, Au$). According to this, the systems can be grouped into two different categories. The systems from the first class are capable of adsorbing CO_2 but the molecule retains its linear geometry. The second group, in addition to adsorbing the molecule, are capable of bending it by a significant angle. The observed adsorption angles resemble those of the radical anion of carbon dioxide, CO_2^- , which has been computed to exhibit an O-C-O angle of 135.1° [4]. In the following chapters, we will revisit this observation and perform additional analysis of the charge distribution. It is worth noting that strong bending of CO_2 appears to correlate with adsorption distances smaller than 2.3 \AA .

3.1 Relaxed Structures of $[Al_{12}M]$, $[Al_{54}M]$ and $[Al_{146}M]$ Aluminium Clusters with CO_2

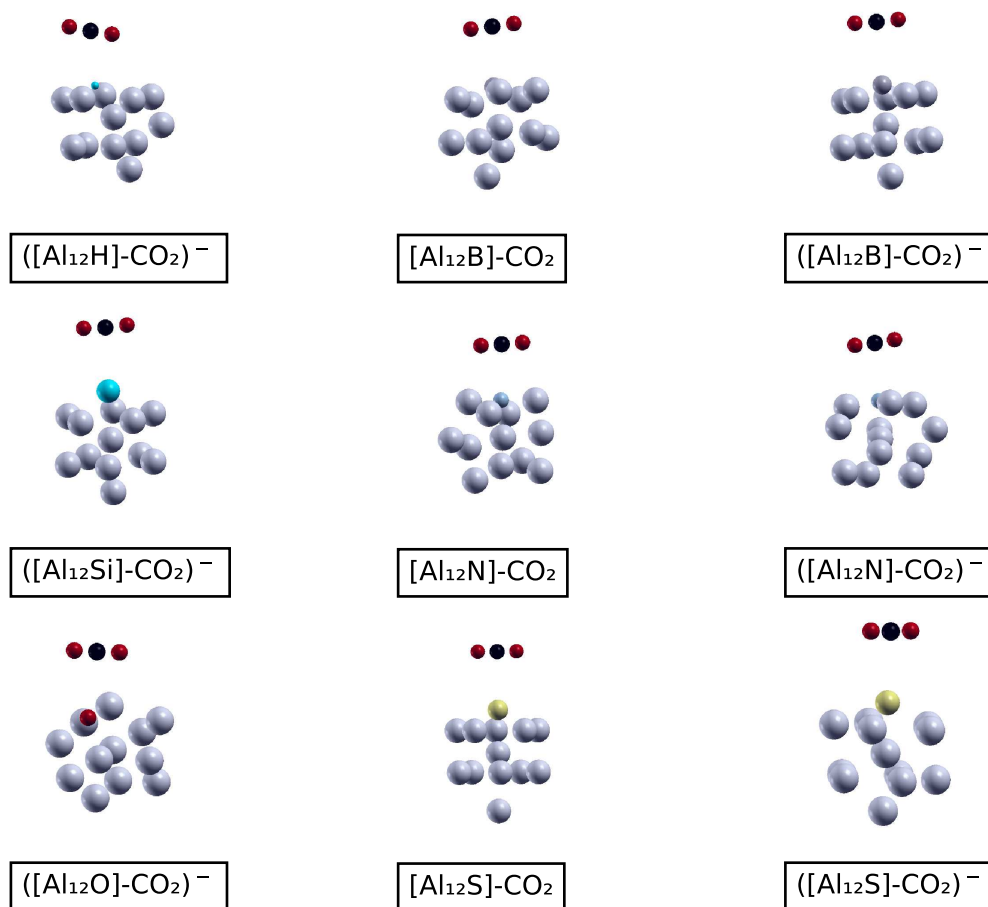


Figure 3.2: Relaxed structures of the d-metal-free $[Al_{12}M]-CO_2$ and $([Al_{12}M]-CO_2)^-$ systems (part 2). Atom colours: Grey = aluminium, black = carbon, red = oxygen, other = dopant.

For negatively charged d-metal-doped clusters (Table 3.2), the systems associated with CO_2 activation are the clusters with $M = Zr, Ru, Co, Ni$ and Ti . For neutral clusters, bent O-C-O angles were observed for the clusters doped with Zr, Mn, Ru, Co and Ni . Although being very popular optical materials, in terms of CO_2 adsorption and activation, gold and silver clearly underperform compared to other dopants. Common catalysts for CO_2 hydrogenation (subsequent to its activation) often contain Rh as a central atom[21], but there have also been reports on catalysts with Ru, Pd, Ti with[84] and without Au [21], Ti with Cu [84], Ni [85], and Zr with Co [86], just to name a few. In both the neutral and the negatively charged cases we found Ru to activate CO_2 but Ti only led to bent carbon dioxide geometries for a negatively charged cluster. Rh - and Pd -doped clusters in our study did not directly activate CO_2 but had adsorption distances that fell into the medium range. Since negatively charged clusters suffer from large Coulomb repulsion which makes it difficult to assemble new materials with them[87], we decided to focus on the neutral clusters. More precisely, our subsequent studies are centred around all neutral clusters exhibiting ground-state CO_2 activation and the two systems without ground-state activation with the smallest adsorption distance ($M = Fe$ and Cu).

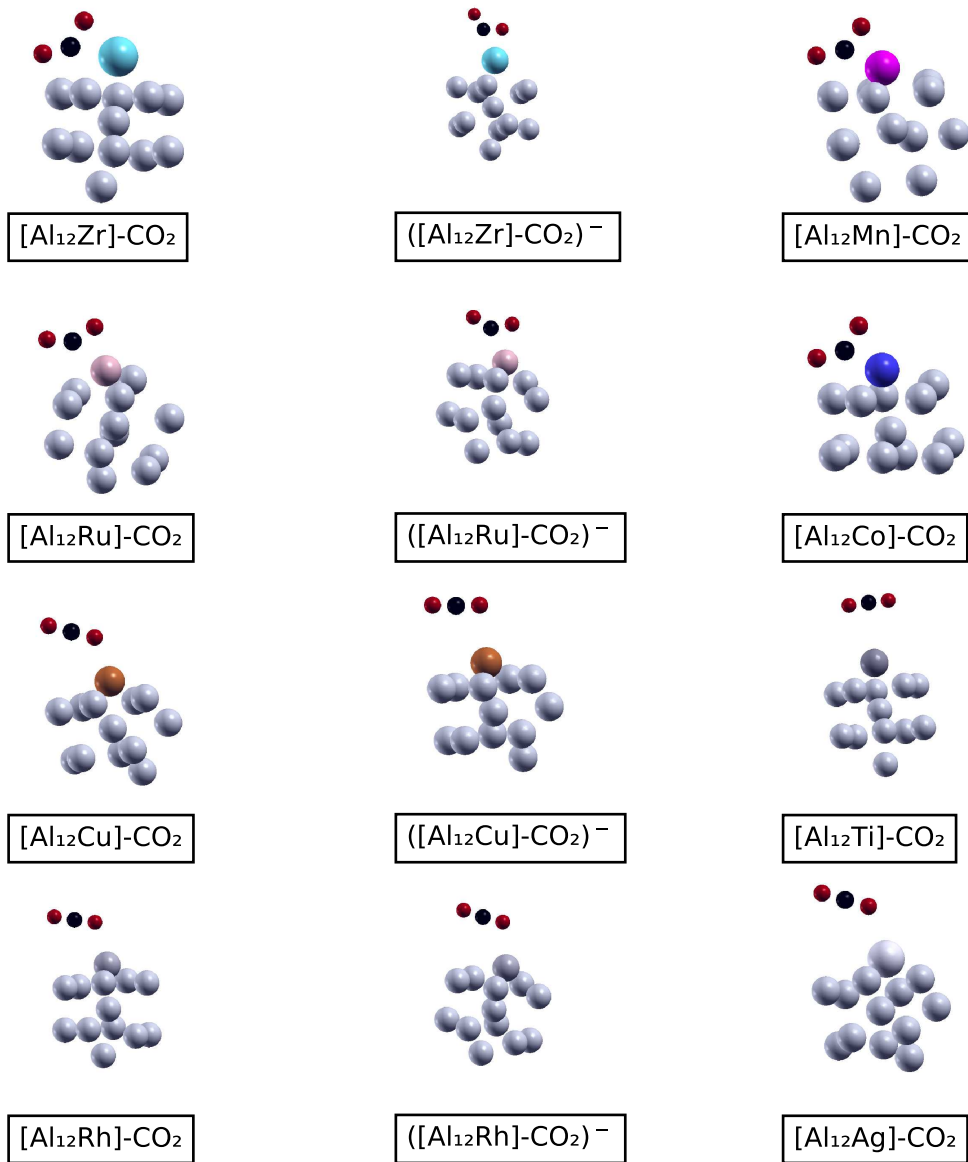


Figure 3.3: Relaxed structures of the d-metal-doped $[Al_{12}M]-CO_2$ and $([Al_{12}M]-CO_2)^-$ systems (part 1). Atom colours: Grey = aluminium, black = carbon, red = oxygen, other = dopant.

For the d-metal doped clusters, the structures after relaxations are displayed in figures 3.3 and 3.4. For the Cu-doped cluster we were able to compare our structure with literature[88]. Despite the adsorbed CO_2 molecule on our cluster, the structure is very similar. It appears that only the clusters in $[Al_{12}Zr]-CO_2$, $([Al_{12}Zr]-CO_2)^-$, $([Al_{12}Mn]-CO_2)^-$, $([Al_{12}Fe]-CO_2)^-$, $[Al_{12}Ti]-CO_2$, $([Al_{12}Ti]-CO_2)^-$ and $[Al_{12}Rh]-CO_2$ exhibit almost perfect icosahedral geometries while all other clusters are strongly distorted. In the case of $[Al_{12}Zr]-CO_2$ and $[Al_{12}Ti]-CO_2$, the total number of valence electrons is 40 which is the same as in $[Al_{13}]^-$, the other d-metal-doped systems with icosahedral geometry, however, have deviating electron numbers.

3.1 Relaxed Structures of $[Al_{12}M]$, $[Al_{54}M]$ and $[Al_{146}M]$ Aluminium Clusters with CO_2

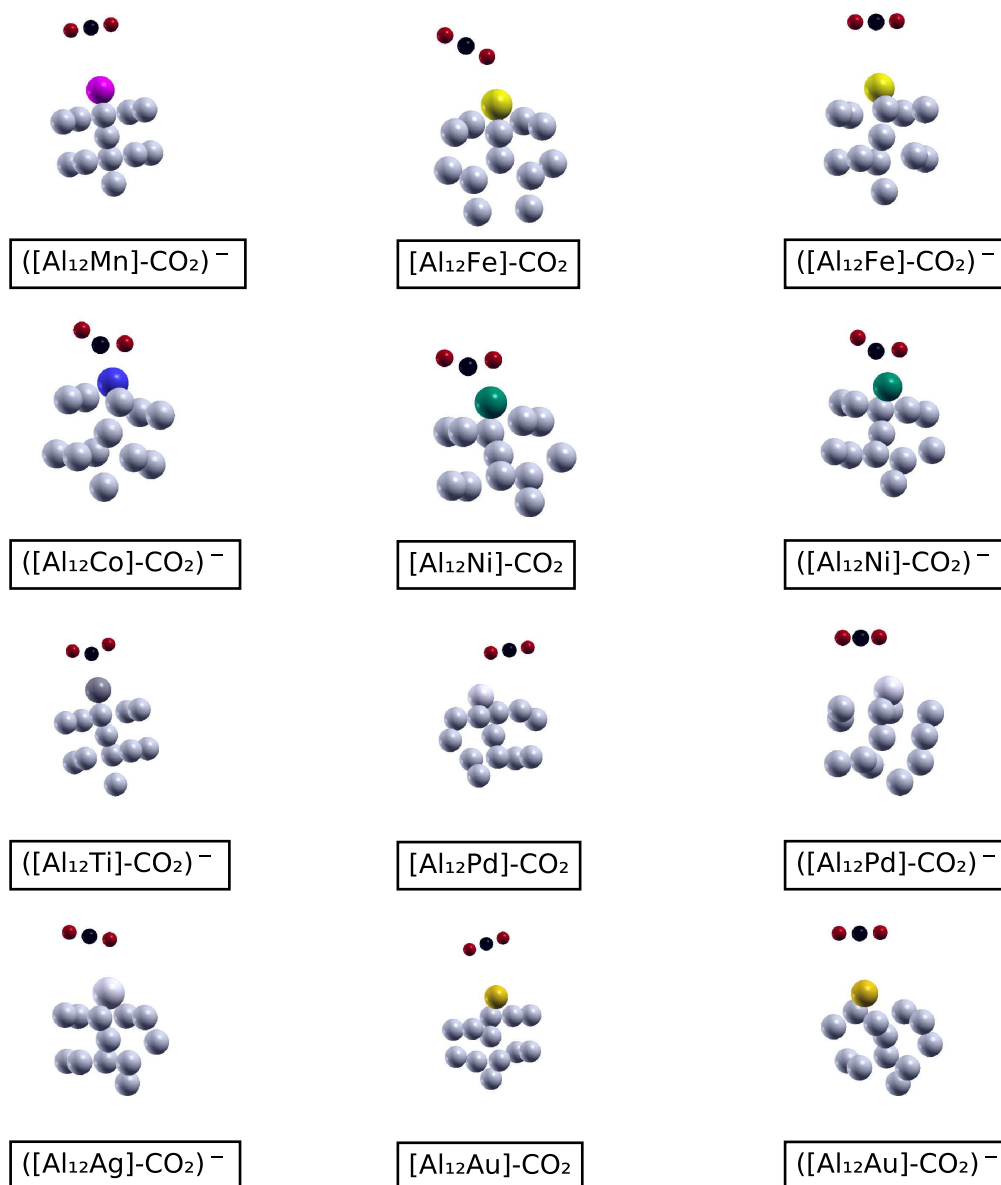


Figure 3.4: Relaxed structures of the d-metal-doped $[Al_{12}M]-CO_2$ and $([Al_{12}M]-CO_2)^-$ systems (part 2). Atom colours: Grey = aluminium, black = carbon, red = oxygen, other = dopant.

In order to investigate the size dependence of a cluster's interaction with CO_2 , we performed the same calculations for neutral Zr-, Mn-, Fe-, Ru-, Co-, Ni- and Zr-doped clusters with one and two additional cluster shells. Again, one of the outer Al atoms is exchanged for a dopant. The resulting geometries for $[Al_{54}M]-CO_2$ and $[Al_{146}M]-CO_2$ can be found in Figures 3.5 and 3.6, respectively. The adsorption distances and O-C-O angles are listed with the other transition-metal-doped clusters in Table 3.2.

Adsorption distances between CO_2 and $[Al_{54}M]$ range from 1.8 Å to 3.7 Å. This is a wider range than the one observed for the $[Al_{12}M]$ clusters. Qualitatively, the results for most clusters do not differ from their smaller counterparts. The Fe-doped cluster e.g. adsorbs CO_2 at roughly the same distance that was observed for $[Al_{12}Fe]$ and is (just like its

3 Results and Discussion

System	Adsorption Distance [Å]	O-C-O Angle[°]
[Al ₁₂ Zr]–CO ₂	1.9 (O-Al)	131.4
([Al ₁₂ Zr]–CO ₂) [−]	2.0 (O-Zr)	126.8
[Al ₅₄ Zr]–CO ₂	1.9 (O-Al)	132.4
[Al ₁₄₆ Zr]–CO ₂	2.0 (O-Al)	132.2
[Al ₁₂ Mn]–CO ₂	1.8 (C-Mn)	137.1
([Al ₁₂ Mn]–CO ₂) [−]	3.5 (C-Mn)	178.2
[Al ₅₄ Mn]–CO ₂	1.9 (C-Mn)	136.0
[Al ₁₄₆ Mn]–CO ₂	1.9 (C-Mn)	135.4
[Al ₁₂ Fe]–CO ₂	2.4 (O-Fe)	179.7
([Al ₁₂ Fe]–CO ₂) [−]	3.4 (C-Fe)	178.2
[Al ₅₄ Fe]–CO ₂	2.3 (O-Fe)	178.8
[Al ₁₂ Ru]–CO ₂	2.1 (C-Ru)	142.9
([Al ₁₂ Ru]–CO ₂) [−]	2.1 (C-Ru)	139.7
[Al ₅₄ Ru]–CO ₂	1.8 (O-Al)	127.6
[Al ₁₄₆ Ru]–CO ₂	1.9 (O-Al)	130.5
[Al ₁₂ Co]–CO ₂	1.8 (C-Co)	135.5
([Al ₁₂ Co]–CO ₂) [−]	1.9 (C-Co)	141.2
[Al ₅₄ Co]–CO ₂	1.8 (O-Al)	126.0
[Al ₁₄₆ Co]–CO ₂	1.9 (O-Al)	132.2
[Al ₁₂ Ni]–CO ₂	2.0 (O-Ni)	146.2
([Al ₁₂ Ni]–CO ₂) [−]	1.9 (C-Ni)	142.0
[Al ₅₄ Ni]–CO ₂	1.8 (C-Ni)	not applicable
[Al ₁₄₆ Ni]–CO ₂	1.8 (O-Al)	125.9
[Al ₁₂ Cu]–CO ₂	2.3 (O-Cu)	179.3
([Al ₁₂ Cu]–CO ₂) [−]	2.8 (O-Cu)	177.1
[Al ₅₄ Cu]–CO ₂	3.7 (O-Cu)	179.6
[Al ₁₄₆ Cu]–CO ₂	3.7 (O-Cu)	179.6
[Al ₁₂ Ti]–CO ₂	3.3 (C-Ti)	178.4
([Al ₁₂ Ti]–CO ₂) [−]	2.2 (C-Ti)	144.8
[Al ₁₂ Pd]–CO ₂	2.7 (O-Pd)	179.6
([Al ₁₂ Pd]–CO ₂) [−]	2.8 (O-Pd)	177.7
[Al ₁₂ Rh]–CO ₂	2.5 (O-Rh)	178.3
([Al ₁₂ Rh]–CO ₂) [−]	2.5 (O-Rh)	175.0
[Al ₁₂ Ag]–CO ₂	2.6 (O-Ag)	179.3
([Al ₁₂ Ag]–CO ₂) [−]	3.0 (O-Ag)	177.8
[Al ₁₂ Au]–CO ₂	3.4 (C-Au)	179.7
([Al ₁₂ Au]–CO ₂) [−]	3.4 (C-Au)	176.9

Table 3.2: Data for the relaxed structures of [Al₁₂M], ([Al₁₂M])[−], [Al₅₄M] and [Al₁₄₆M] clusters with transition-metal dopants and adsorbed CO₂. The adsorption distance is measured as the minimum distance that can be found between any molecular and any cluster atom. The information given in the brackets refers to the atoms between which this distance is measured. The third column shows the O-C-O angle in degree.

smaller counterpart) not able to angle the molecule upon adsorption. The Zr-, Mn-, Ru- and Co-doped clusters are capable of activating carbon dioxide, with the main difference

3.1 Relaxed Structures of $[Al_{12}M]$, $[Al_{54}M]$ and $[Al_{146}M]$ Aluminium Clusters with CO_2

being the 0.3 Å decrease in adsorption distance for the Ru doped cluster compared to that

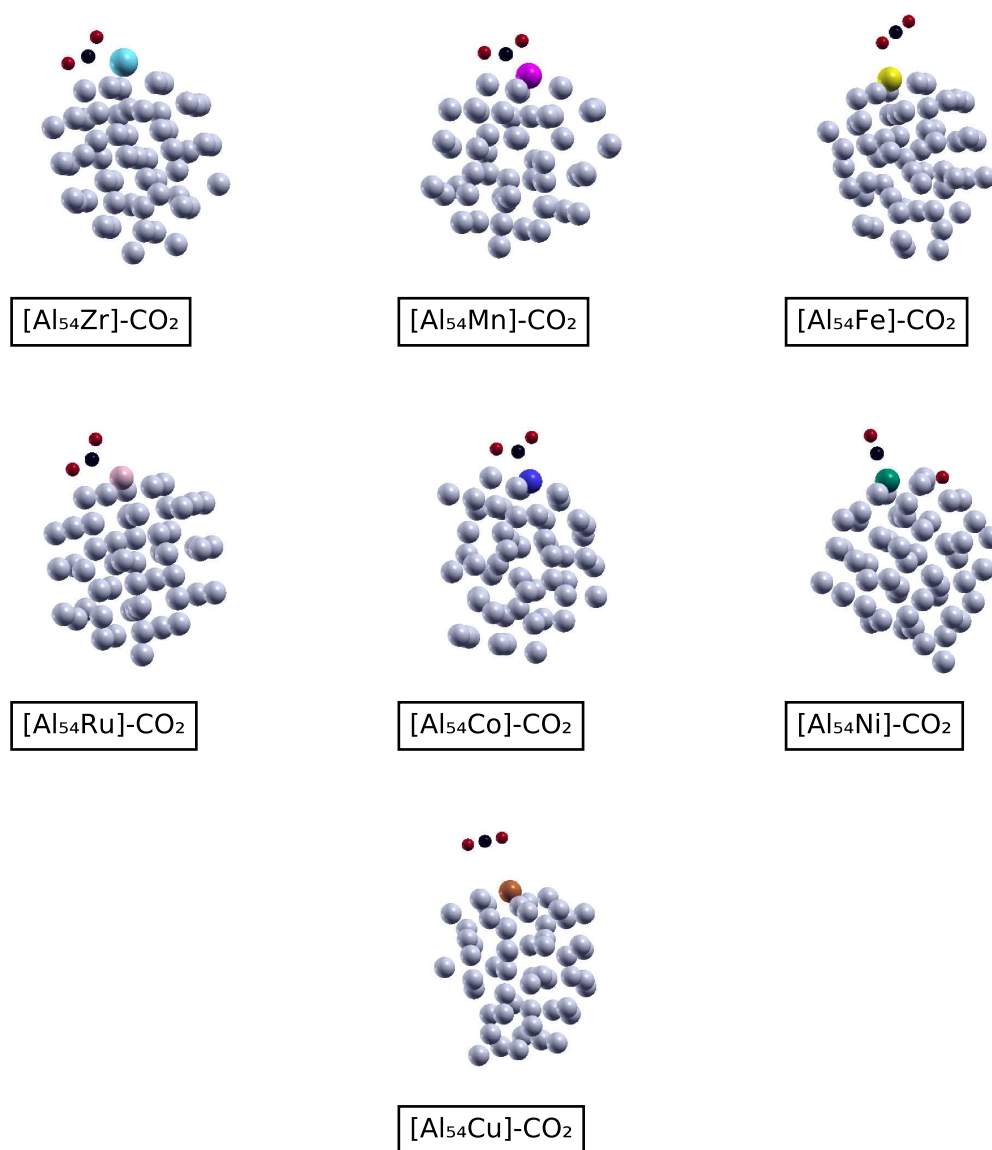


Figure 3.5: Relaxed structures of the d-metal-doped $[Al_{54}M]-CO_2$ systems. Atom colours: Grey = aluminium, black = carbon, red = oxygen, other = dopant.

of $[Al_{12}Ru]-CO_2$. This also explains the smaller O-C-O angle of CO_2 when adsorbed to $[Al_{54}Ru]$. The other adsorption distances differ from their smaller counterparts by no more than 0.1 Å. The relaxed structures of the $[Al_{54}M]-CO_2$ systems are displayed in figure 3.5. For the medium sized clusters, the most distorted structures are formed by the Co-, Cu- and Ni-doped clusters. This is in good agreement with the structures obtained for small clusters. The Cu-doped cluster exhibits the largest adsorption distance of all small and medium sized systems with 3.7 Å, which is 0.9 Å more than in $[Al_{12}Cu]-CO_2$. In contrast to the smaller systems though no medium-sized cluster takes on a perfectly icosahedral structure. The $[Al_{54}M]$ clusters all contain between 127 ($[Al_{54}Zr]$) and 134 electrons in

3 Results and Discussion

the case of $[\text{Al}_{54}\text{Cu}]$ in their valence shell. The "magic numbers", referring to the number of valence electrons that would form a full jellium shell, which are closest to this are 112 and 168[89]. This comparably large gap to the neighbouring magic numbers might be the reason for the lack of highly symmetrical geometries in these systems. For the Ni-doped cluster, however, a new behaviour can be observed: Instead of adsorbing and activating the molecule, CO_2 is dissociated into CO and an oxygen atom which is adsorbed to the surface Al atoms. While carbon monoxide is adsorbed to the dopant with its carbon atom, the oxygen seems to oxidize the neighbouring Al atoms. Al, being a non-precious metal, is known to be very prone to oxidation[90], yet it is not clear why this is not observed for any of the other systems. It would be interesting to investigate how a fully oxidized Al surface with a Ni atom as dopant would interact with CO_2 . Although not covered in this thesis, it remains to be seen if, after poisoning of the surface, the cluster would still be catalytically active and capable of adsorbing, activating or even dissociating CO_2 (e.g. via diffusion through porous aluminium oxide layers[36]). The same study could be conducted for the other clusters to investigate the effect of oxidization on the catalysts' performance.

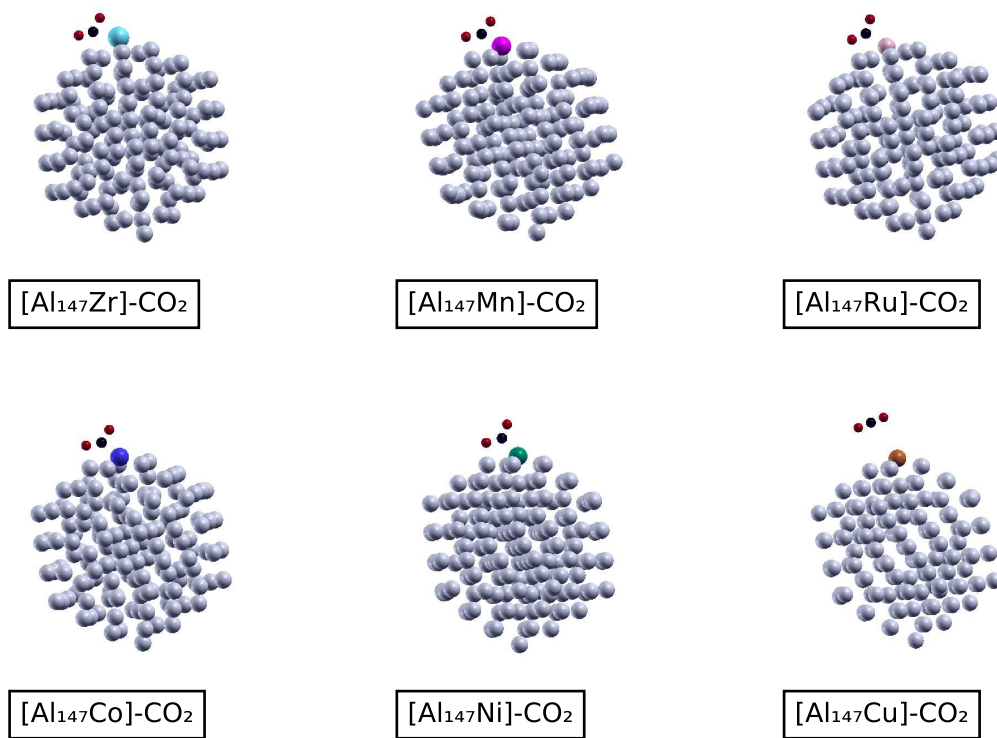


Figure 3.6: Relaxed structures of the d-metal-doped $[\text{Al}_{146}M]-\text{CO}_2$ systems. Atom colours: Grey = aluminium, black = carbon, red = oxygen, other = dopant.

For the large clusters, $[\text{Al}_{146}M]-\text{CO}_2$, finding relaxed structures proofed difficult due to slow convergence. For this reason we did not include an Fe-doped system but only clusters doped with Zr-, Mn-, Ru-, Co-, Ni- and Cu. The relaxed structures of the $[\text{Al}_{146}M]-\text{CO}_2$ systems can be found in figure 3.6. Distortions in these systems are very small, leading to almost perfect, quasi-spherical icosahedra. With these clusters' valence electrons

3.1 Relaxed Structures of $[Al_{12}M]$, $[Al_{54}M]$ and $[Al_{146}M]$ Aluminium Clusters with CO_2

falling between 280 and 287, again the next magic numbers with 240 and 330[89] are far away. Although the jellium model seems to be sufficient to explain some trends in the smaller clusters, it seems to lose predictive power with increasing cluster size. Adsorption distances in $[Al_{146}M]-CO_2$ range from 1.8 Å to 3.7 Å. Again, the Cu-doped cluster has the largest adsorption distance. The adsorption distances of all other systems are almost equal to those of the medium sized clusters. All dopants that have been found to be capable of activating CO_2 upon adsorption in $[Al_{12}M]$ exhibit bent geometries for CO_2 . It is worth noting that, unlike in the medium sized cluster, Ni doping here does not lead to dissociation of CO_2 .

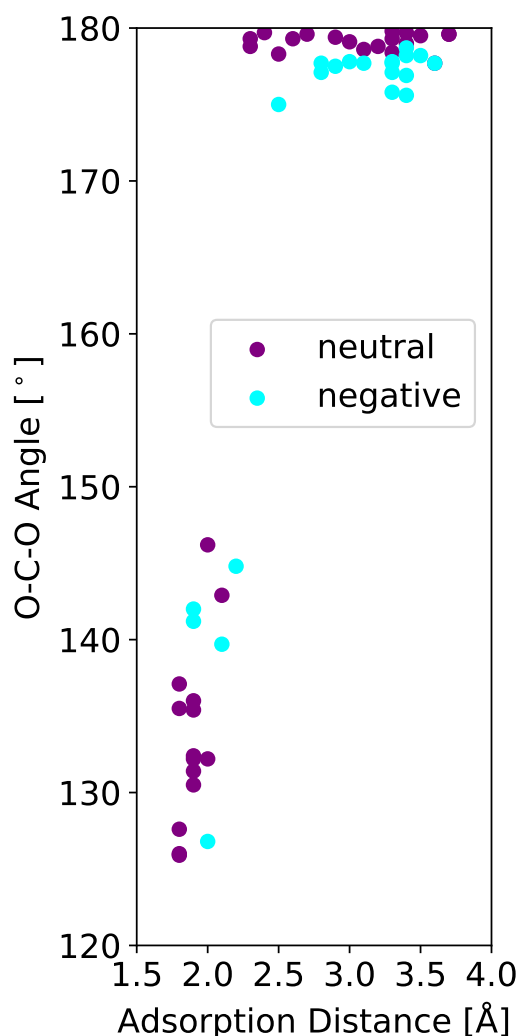


Figure 3.7: O-C-O angle plotted against the respective adsorption distance. The results for the neutral clusters are displayed in purple, the negatively charged clusters' values are indicated in turquoise.

In general, structural differences between systems seem to be decreased with increasing cluster size which can be seen from the almost perfect icosahedral geometries of all large clusters. This trend can be explained by the smaller fraction the dopant has compared to the over all structure since we always only introduced one dopant atom per cluster. This

emphasizes that the adsorption is not solely a property of the dopant but the Al atoms also play a crucial role: The overall differences in adsorption distances among the large systems are smaller than for the $[\text{Al}_{12}M]$ and $[\text{Al}_{54}M]$ clusters but CO_2 is always located in direct proximity to the dopant. The bigger a system, the more likely it seems to approach a spherical geometry which is in good agreement with the fact that synthesized Al nanoparticles often take up spherical geometries[91].

Figure 3.7 shows the O-C-O angles of all 55 systems studied plotted against their respective adsorption distance. It can be seen that for adsorption distances larger than 2.3 Å, the O-C-O angles are very close to 180°. For all adsorption distances which are below this threshold value, O-C-O angles are smaller than 150°. For the longer adsorption distances with almost linear CO_2 , there is a significant difference between neutral and negatively charged systems. The resulting O-C-O angles from the negative clusters (symbolized by turquoise symbols) are all slightly smaller than those found in the neutral systems at comparable adsorption distances. One possible explanation is delocalization of some of the excess electron over the CO_2 molecule which results in a more bent geometry in order to accommodate the charge. Nevertheless, O-C-O angles in all negative systems with adsorption distances above 2.3 Å are all well above 170° so the CO_2 remains almost linear. For smaller adsorption distances, the trend of finding smaller O-C-O angles for comparably larger adsorption distances in negatively charged clusters seems at least to be less dominant. Due to the small amount of negative systems in our study which exhibited adsorption distances below 2.3 Å, it is difficult to tell if the trend continues for these cases or if local effects become so dominant that this is compensated.

3.1.1 Summary

We investigated CO_2 adsorption behaviour on a variety of small Al clusters, ranging from 13 to 147 atoms. Results were highly sensitive to spin, charge, dopant atom and size. Introduction of dopants led to increased adsorption compared to the un-doped $[\text{Al}_{13}]$ and $[\text{Al}_{13}]^-$ clusters. Generally, there seems to be a critical adsorption distance of 2.3 Å below which CO_2 activation is observed. This distance could only be achieved by d-metal-doped systems. Adsorption angles of all negatively charged systems without d-metal-dopants turned out to be smaller than those of their neutral counter-parts. With increasing size, clusters become less distorted and adsorption distances among different systems approach each other.

We found that for neutral systems, Zr, Mn, Ru, Ni and Co consistently exhibited CO_2 activation, although of varying kind for Ni with respect to system size. Cu doping only led to CO_2 adsorption distances below 2.5 Å for the smallest neutral system size and never resulted in bent CO_2 geometries. For the negatively charged $[\text{Al}_{12}M]^-$ CO_2 systems, the dopants Zr, Ru, Co, Ni and Ti resulted in CO_2 activation. Independent of charge and size, Zr, Ru and Co led to bent O-C-O angles without exception. Ni also appeared to be catalytically active for all types of clusters studied, but in the medium-sized system it did not just activate but dissociate CO_2 .

3.2 Electronic Properties of $[\text{Al}_{12}\text{M}]-\text{CO}_2$

In this chapter we investigate the electronic properties of the structures we previously found to be most promising, namely the neutral $[\text{Al}_{12}\text{M}]-\text{CO}_2$ systems with M being Zr, Mn, Fe, Ru, Co, Ni and Cu. Since some clusters led to activated O-C-O adsorption geometries, we will further study the implications this has on the electronic structure. Our focus lies on ground-state properties such as spin multiplicity, dopant electron configuration, ionization energy, adsorption energy and ground-state electron transfer as well as excited state properties such as absorption spectra and light-induced charge-transfer (LICT). All calculations except for the LICT analysis have also been performed with a Hubbard +U correction[61] to show that the effect of d-electrons is sufficiently well described by LDA in these systems. For the LICT we introduce an approach that combines the information obtained from linear response TDDFT calculations with results from a projection of the DOS onto atomic orbitals which results in a measure of electron transfer without requiring integration over excited state transition densities.¹

3.2.1 Ground State Properties

In this section we will discuss all ground state properties of the isolated clusters and those with adsorbed CO_2 . We will start with a discussion of general aspects like the spin multiplicity, ionization potentials, adsorption energies and ground-state charge-transfer, move on to electron localization functions (ELFs) and atomic orbital projected densities of states (pDOS) and dopant electron configurations. We will also analyse the HOMO and LUMO shapes of the adsorbed CO_2 molecules. Along the way we will compare the results to values obtained with a Hubbard +U correction of 6 eV to determine if this correction is necessary for further calculations or yields qualitatively similar results.

Table 3.3 shows the electronic ground-state properties of $[\text{Al}_{12}\text{Zr}]-\text{CO}_2$, $[\text{Al}_{12}\text{Mn}]-\text{CO}_2$, $[\text{Al}_{12}\text{Fe}]-\text{CO}_2$, $[\text{Al}_{12}\text{Ru}]-\text{CO}_2$, $[\text{Al}_{12}\text{Co}]-\text{CO}_2$, $[\text{Al}_{12}\text{Ni}]-\text{CO}_2$ and $[\text{Al}_{12}\text{Cu}]-\text{CO}_2$. The ionization energy was obtained through delta-SCF calculations. Adsorption energy denotes the difference in total energy of the system and its isolated, separately relaxed parts (cluster and CO_2 molecule) in their respective lowest-energy spin state. Results in brackets refer to the same quantities computed for the isolated, relaxed clusters. Ground-state CT is analysed via a Hirshfeld scheme[73] as implemented in Octopus.

It can be seen that all $[\text{Al}_{12}\text{M}]-\text{CO}_2$ systems except for $[\text{Al}_{12}\text{Fe}]-\text{CO}_2$ exhibit a low-spin multiplicity as their most favourable spin state. In contrast, the Fe doped system's ground-state is a quintet. When comparing the isolated clusters with their corresponding adsorbed system, it is worth noting that for $[\text{Al}_{12}\text{Co}]$ and $[\text{Al}_{12}\text{Mn}]$, high-spin ground-states (quartet and sextet, respectively) are found despite $[\text{Al}_{12}\text{Co}]-\text{CO}_2$ and $[\text{Al}_{12}\text{Mn}]-\text{CO}_2$ both

¹This chapter is in large parts based on [doi:10.1021/acs.jpca.1c02621](https://doi.org/10.1021/acs.jpca.1c02621): Göbel, A.; Rubio, A. & Lischner, J., Light-Induced Charge Transfer from Transition-Metal-Doped Aluminum Clusters to Carbon Dioxide, *JPC A*, **2021**.

System	Spin-state	Vertical Ionization Energy [eV]	Adsorption Energy [eV]	GS CT into CO_2 [-e]
$[Al_{12}Zr]-CO_2$	singlet (singlet)	6.3 (6.2)	-2.0	+0.36
$[Al_{12}Mn]-CO_2$	doublet (sextet)	6.5 (6.2)	-1.5	+0.28
$[Al_{12}Fe]-CO_2$	quintet (quintet)	6.0 (6.2)	-0.3	-0.08
$[Al_{12}Ru]-CO_2$	singlet (singlet)	6.4 (6.2)	-1.2	+0.31
$[Al_{12}Co]-CO_2$	doublet (quartet)	6.4 (6.3)	-2.0	+0.29
$[Al_{12}Ni]-CO_2$	singlet (singlet)	6.7 (6.4)	-0.7	+0.20
$[Al_{12}Cu]-CO_2$	doublet (doublet)	6.4 (6.5)	-0.3	-0.07

Table 3.3: Electronic ground-state data of $[Al_{12}M]$ with adsorbed CO_2 , values for the isolated clusters are written in brackets. Results include the spin multiplicity, ionization energy, adsorption energy and the ground-state electron transfer (GS CT) into CO_2 (evaluated by Hirshfeld’s scheme). Here, a positive value for GS CT means that electrons are being transferred from the cluster into the CO_2 molecule. Results are obtained with a simple LDA approximation without further corrections.

being doublets. All other clusters retain their spin-state upon CO_2 adsorption. Ionization energies fall in the range of 6.0 eV to 6.7 eV, with $[Al_{12}Fe]-CO_2$ exhibiting the lowest and $[Al_{12}Ni]-CO_2$ the highest value. This range is smaller for the isolated clusters where ionization energies between 6.2 eV and 6.5 eV can be observed. These results are in good agreement with the ionisation energy of isolated $[Al_{12}Cu]$ from literature (5.96 eV).[88] The reason for the small difference can be explained by the different XC functional that has been used in the other study. Comparison of a system’s ionization energy with that of the corresponding isolated cluster shows that all systems except for $[Al_{12}Fe]$ and $[Al_{12}Cu]$ see an increase of the ionization potential upon adsorption. This can be interpreted as an electronic stabilization which can be explained by the Nephelauxetic effect[92]: upon CO_2 adsorption, hybridized states are formed which contain cluster as well as molecular character. This is most significant in systems with ground-state electron transfer and results in an overall reduction of electron-electron repulsion in these states due to an increased delocalization. This then makes spin-pairing more favourable due to the reduced electron-electron repulsion that results from this delocalization. The change in spin-state upon adsorption which is observed in the Co and the Mn-doped clusters can also be explained by this. Due to the aforementioned reduced electron-electron repulsion, low-spin states are energetically favourable over the high-spin multiplicities observed in the isolated clusters. Electronic stabilization upon adsorption seems to be strongest in $[Al_{12}Mn]$ and $[Al_{12}Ni]$. $[Al_{12}Mn]$ also undergoes the most dramatic change in spin-multiplicity upon adsorption.

Adsorption energies of CO_2 to the clusters range from -0.3 eV to -2.0 eV. The weakest adsorptions of CO_2 are observed in $[Al_{12}Fe]-CO_2$ and $[Al_{12}Cu]-CO_2$ which are the two systems that exhibit a linear geometry of the molecule and have the largest adsorption distance. On the other hand, the highest adsorption energies can be found in $[Al_{12}Zr]-CO_2$ and $[Al_{12}Co]-CO_2$ which exhibit some of the lowest adsorption distances. Overall, we noted a rise in adsorption energy with decreasing adsorption distance which can be explained through weaker interactions between cluster and molecule.

3 Results and Discussion

Since the bent CO_2 geometry which we found in $[\text{Al}_{12}\text{Zr}]-\text{CO}_2$, $[\text{Al}_{12}\text{Mn}]-\text{CO}_2$, $[\text{Al}_{12}\text{Ru}]-\text{CO}_2$, $[\text{Al}_{12}\text{Co}]-\text{CO}_2$ and $[\text{Al}_{12}\text{Ni}]-\text{CO}_2$ resembles that of an activated CO_2 molecule, we performed a Hirshfeld analysis[73] of the ground state. This revealed that all systems exhibiting CO_2 angles much different from the 180° found in isolated CO_2 [4] exhibit significant ground-state electron-transfer into the molecule. Only $[\text{Al}_{12}\text{Fe}]-\text{CO}_2$ and $[\text{Al}_{12}\text{Cu}]-\text{CO}_2$ show very small negative values which can be interpreted as electrons being transferred from the molecule into the cluster. The largest amount of charge-transfer can be observed in $[\text{Al}_{12}\text{Zr}]-\text{CO}_2$ (+0.36) which has one of the smallest adsorption distances with 1.9 Å. Only the Mn and Co doped clusters exhibit smaller CO_2 adsorption distances with 1.8 Å (see chapter 3.1).

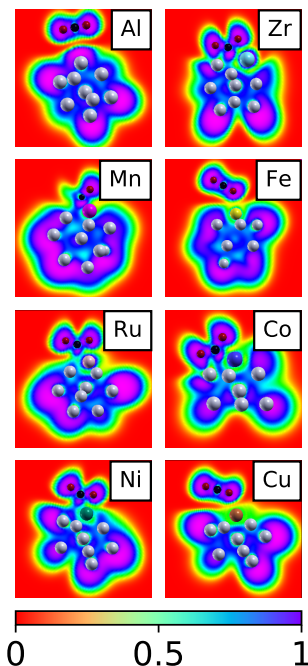


Figure 3.8: Electron Localization Function (ELF) of the transition-metal doped clusters with adsorbed CO_2 . For better comparison, the ELF of a neutral $[\text{Al}_{13}]$ cluster with CO_2 is also displayed (upper left picture). This figure has been published in [93].

We also computed electron-localization functions (ELFs)[94] for all systems as well as neutral $[\text{Al}_{13}]$ with CO_2 in order to investigate the impact of the dopant on the electronic character of the clusters (see Figure 3.8). From this it becomes clear that the most important changes in electronic character are limited to the direct neighbourhood of the dopant. For the systems exhibiting ground-state CT, the ELF exhibits an extra lobe at the carbon atom of CO_2 , which faces towards the cluster. The values of the ELFs in this region are close to unity which shows the highly localized character of these electrons. This can be interpreted as a footprint of the additional charge located at the CO_2 which leads to a change in sign of the partial charge of the carbon atom. This shows that our findings from the ELFs are in good agreement with the so-called "Umpolung" which the carbon atom of CO_2 undergoes upon activation.[4]

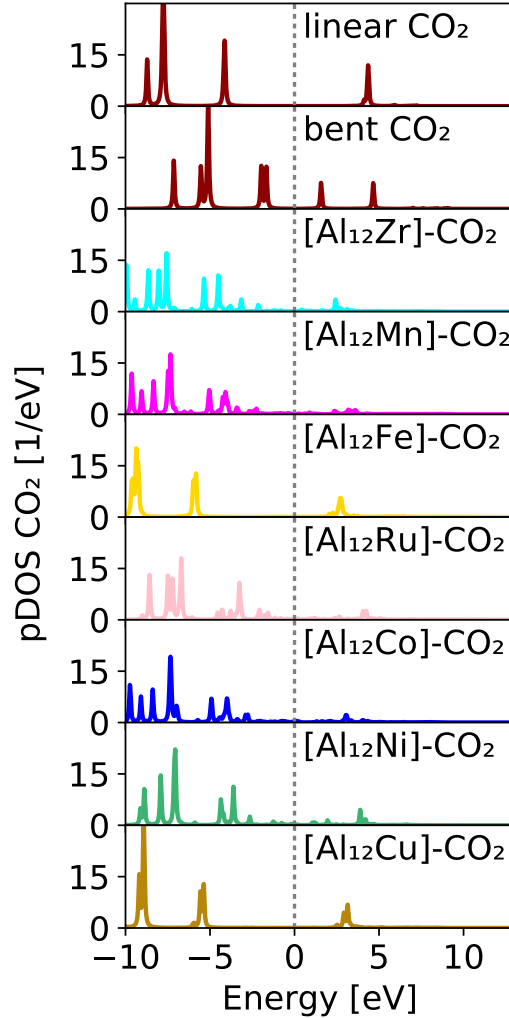


Figure 3.9: DOS projected onto 2s- and 2p-character atomic orbitals of CO_2 for the $[Al_{12}M]-CO_2$ systems. The energy scale is shifted by the system's respective Fermi-level which is denoted by a grey vertical line. For better comparison, the DOS of isolated carbon dioxide is displayed at the top. A broadening of 0.05 eV has been used in all graphs. This figure has been published in [93].

Figure 3.9 shows the density of states (DOS) of isolated CO_2 , bent CO_2 (135°) and all systems projected onto an atomic orbital basis of carbon and oxygen atoms (pDOS). Comparison of the pDOS of linear and bent CO_2 shows that the degenerate states located above the Fermi energy split and one of the states is lowered in energy. The states below the Fermi energy are red-shifted as well. For weakly bound CO_2 , as can be found in $[Al_{12}Fe]-CO_2$ and $[Al_{12}Cu]-CO_2$, the pDOS resembles that of linear CO_2 , exhibiting a big gap between the HOMO and the LUMO (~ 8 eV). In contrast, the other systems exhibit several small peaks close to the Fermi level, containing the extra charge that has been transferred upon adsorption (see ELF and Table 3.3). The reason why the pDOSs do not exactly resemble those of the corresponding bent CO_2 molecule lies in the strong hybridisation between cluster and CO_2 states.

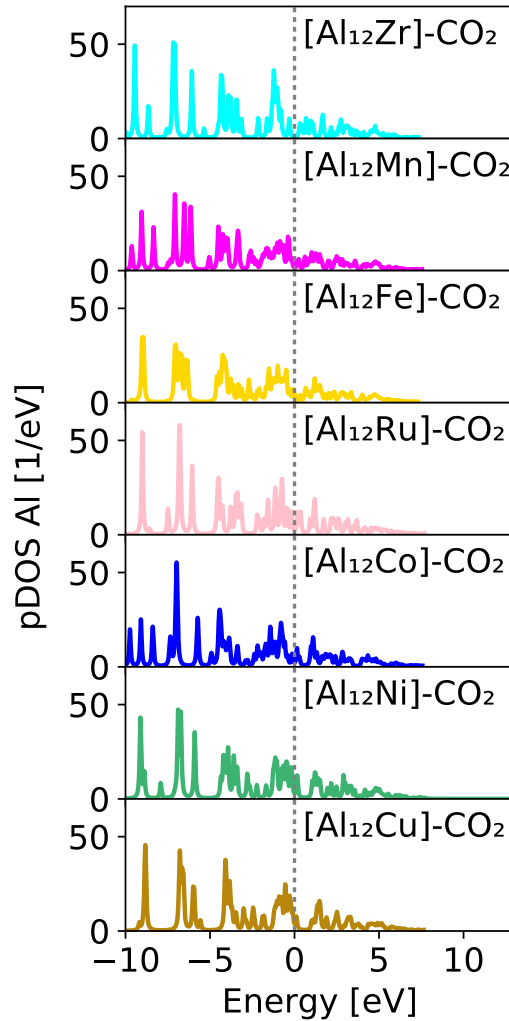


Figure 3.10: DOS projected onto atomic orbitals of Al for the $[Al_{12}M]$ systems. The energy scale is shifted by the system's respective Fermi-level which is denoted by a grey vertical line. A broadening of 0.05 eV has been used in all graphs. This figure has been published in [93].

Figure 3.10 shows the Al projected DOS and Figure 3.11 displays the transition-metal projected DOS for the adsorbed systems. The Al pDOS of all systems is generally very similar. There is many occupied states around the Fermi energy. Only the Zr-doped cluster shows a more distinct peak at about 1 eV which can be explained by the system's high amount of symmetry which results in more degeneracies. Above the Fermi energy there is also multiple small peaks but in the cases of the Co-, Ni- and Cu-doped clusters these appear to be shifted to slightly higher energies.

For the transition-metal pDOS variations among the different systems are more notable. $[Al_{12}Zr]-CO_2$ for example has a high intensity peak shortly above the Fermi energy. $[Al_{12}Mn]-CO_2$ has lots of small evenly spread peaks that are hard to distinguish around the Fermi energy and $[Al_{12}Ni]-CO_2$ exhibits a high intensity peak directly at the Fermi energy. The most striking difference is that the Cu-doped system only exhibits very small peaks around the Fermi energy and the majority of states of the Cu atom seem to be clustered at about -3 eV. We will discuss some implications of these findings when

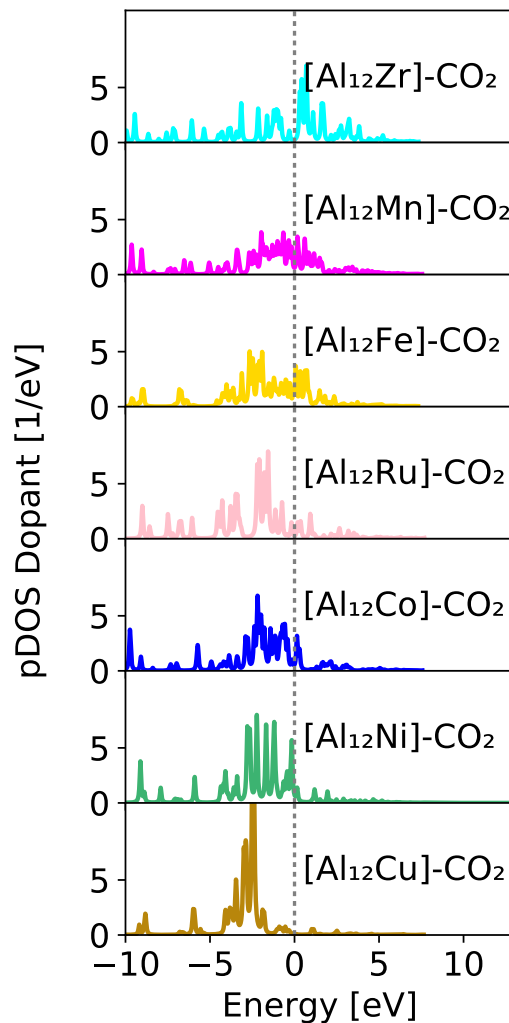


Figure 3.11: DOS projected onto atomic orbitals of the dopant for the $[Al_{12}M]$ systems. The energy scale is shifted by the system's respective Fermi-level which is denoted by a grey vertical line. A broadening of 0.05 eV has been used in all graphs. This figure has been published in [93].

addressing LICT in section 3.2.2.

Table 3.5 displays the KS wave functions of the states which we identified as the CO_2 HOMO and LUMO from our hybridisation analysis conducted on the pDOS. For better comparison, we also calculated the wave functions of a linear CO_2 molecule and one that is bent by 135° (Table 3.4). Our results for the HOMO and LUMO shape of the isolated CO_2 molecule with different angles are in good agreement with literature.[4] In Table 3.5, two basic types of HOMO shapes can be distinguished. One resembles the HOMO of linear CO_2 (this can be found in $[Al_{12}Fe]-CO_2$ and $[Al_{12}Cu]-CO_2$). The other type of HOMO is found in $[Al_{12}Zr]-CO_2$, $[Al_{12}Mn]-CO_2$, $[Al_{12}Ru]-CO_2$, $[Al_{12}Co]-CO_2$ and $[Al_{12}Ni]-CO_2$. Although being the HOMO, its shape is more similar to that of the bent CO_2 molecule's LUMO shape which is another proof of charge-transfer.

3 Results and Discussion

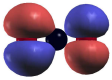
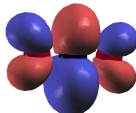
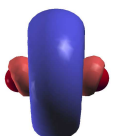
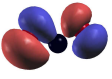
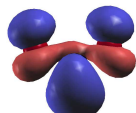
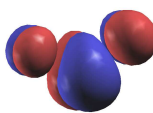
System	HOMO	LUMO	LUMO+1
CO ₂ (linear)			
CO ₂ (bent)			

Table 3.4: CO₂ HOMO and LUMO shapes of a linear and a bent isolated CO₂ molecule.

The angular momentum-resolved Mulliken analysis of the dopant atoms leads to the results displayed in Table 3.6. The partial charges on the transition-metals range from -0.1 for [Al₁₂Fe]-CO₂, [Al₁₂Fe], [Al₁₂Ni]-CO₂ and [Al₁₂Cu] to +0.5 for [Al₁₂Zr]-CO₂. The differences in dopant charge between the systems and their corresponding isolated clusters are marginal. In terms of orbital occupations, all systems exhibit the same trend: the d-states contain roughly one electron more than the configuration of the isolated atom would suggest. The only exception are the Ru and Cu doped clusters where the d-states of the isolated atoms contain one more electron than their position in the periodic table would indicate anyway since e.g. an isolated Cu atom has a full d-shell and a half-occupied s-orbital. For example, Fe is located in the 6th d-group of the periodic table, which should result in 6 d-electrons. However, the Mulliken analysis reveals that the amount of d-electrons is closer to 7 (see Table 3.6). The extra electron with d-character is taken from the s-orbitals.

<i>M</i>	El. conf.	Partial charge	s	p	d	Dopant spin
Zr	[Kr]4d ² 5s ²	+0.5 (+0.4)	8.5 (8.8)	18.4 (18.2)	12.5 (12.6)	0 (0)
Mn	[Ar]3d ⁵ 4s ²	+0.1 (+0.3)	6.5 (6.7)	12.3 (12.3)	6.0 (5.6)	1.2 (4.1)
Fe	[Ar]3d ⁶ 4s ²	-0.1 (-0.1)	6.7 (6.7)	12.6 (12.6)	6.8 (6.7)	2.8 (2.9)
Ru	[Kr]4d ⁷ 5s ¹	0 (0)	8.4 (8.5)	18.5 (18.3)	16.9 (17.2)	0 (0)
Co	[Ar]3d ⁷ 4s ²	0 (+0.1)	6.6 (6.7)	12.5 (12.4)	7.9 (7.9)	0.3 (1.5)
Ni	[Ar]3d ⁸ 4s ²	-0.1 (0)	6.7 (6.7)	12.5 (12.3)	8.9 (8.9)	0 (0)
Cu	[Ar]3d ¹⁰ 4s ¹	0 (-0.1)	6.8 (6.8)	12.5 (12.5)	9.7 (9.7)	0.1 (0.1)

Table 3.6: Angular momentum-resolved Mulliken charges of the dopant atoms in [Al₁₂*M*]-CO₂. Results were obtained with FHI-aims, values for the isolated clusters are displayed in brackets. "El. conf." denotes the electron configuration of the isolated dopant atom and "s", "p" and "d" denote the amount of electrons of the respective character.

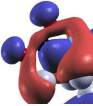
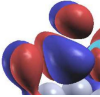
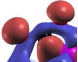
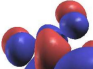

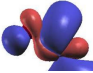
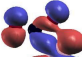

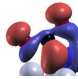
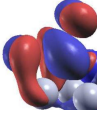
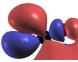
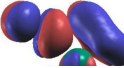


System	HOMO	LUMO
$[Al_{12}Zr]-CO_2$		
$[Al_{12}Mn]-CO_2$		
$[Al_{12}Fe]-CO_2$		
$[Al_{12}Ru]-CO_2$		
$[Al_{12}Co]-CO_2$		
$[Al_{12}Ni]-CO_2$		
$[Al_{12}Cu]-CO_2$		

Table 3.5: CO_2 HOMO and LUMO shapes of $[Al_{12}M]$ clusters with adsorbed CO_2 . For reference, the HOMO and LUMO of a linear and a bent isolated CO_2 molecule are displayed in Table 3.4. For better visibility, the figures display only the section of the wave function that is located around CO_2 .

It is worth noting that the dopant spin (unless the system or cluster is a singlet) equals the total spin of the system minus one (refer to spin states in Table 3.3) except in $[Al_{12}Mn]-CO_2$ where the dopant spin is close to 1 and the ground-state spin-state is a doublet which means that in this case all spin-moment is distributed on the dopant. All other cases, however, reveal that a spin-moment of 1 is distributed among the Al atoms for the clusters. These results are interesting since they show that the catalytic activation is a complicated interplay between the dopant and the Al atoms. This shows that the catalytic activity is not just due to the dopant which is incorporated into some host structure but Al also seems to play a vital role in the CT.

3 Results and Discussion

System	Spin-state	Vertical Ionization Energy/eV	Adsorption Energy/eV	GS CT into CO ₂
[Al ₁₂ Zr]–CO ₂	singlet (singlet)	6.2 (6.2)	-1.7	+0.36
[Al ₁₂ Mn]–CO ₂	quartet (sextet)	6.5 (6.3)	+0.4	+0.28
[Al ₁₂ Fe]–CO ₂	quintet (quintet)	6.2 (6.4)	-0.2	-0.08
[Al ₁₂ Ru]–CO ₂	singlet (singlet)	6.5 (6.3)	-1.1	+0.31
[Al ₁₂ Co]–CO ₂	quartet (quartet)	6.3 (6.5)	-0.9	+0.29
[Al ₁₂ Ni]–CO ₂	singlet (singlet)	6.7 (6.4)	-0.5	+0.40
[Al ₁₂ Cu]–CO ₂	doublet (doublet)	6.4 (6.5)	-0.3	-0.07

Table 3.7: Electronic ground-state data of [Al₁₂M] with adsorbed CO₂, calculated with a Hubbard +U correction[61] of 6 eV, values for the isolated clusters are written in brackets. Results include the spin multiplicity, ionization energy, adsorption energy and the ground-state electron transfer (GS CT) into CO₂ (evaluated by Hirshfeld’s scheme). Results that qualitatively differ from the data obtained without the +U correction are marked in **bold**.

Since all systems discussed here contain d-electrons, we computed the same quantities with a Hubbard +U correction of 6 eV to see if our functional was sufficient to capture the most important correlation effects. Table 3.7 displays the same quantities as Table 3.3 but obtained with a Hubbard +U correction[61] of 6 eV. We have chosen this value since it is well within the range of values that have shown to be successful for different transition-metal oxides.[61] Results that are qualitatively different are highlighted in bold. The main differences can be found with respect to spin-multiplicity in [Al₁₂Mn]–CO₂ and [Al₁₂Co]–CO₂. Interestingly, the +U correction only alters the multiplicity of adsorbed systems while the spin-states of the isolated clusters remain unchanged. It can be seen that the Mn and Co doped systems form a high-spin state upon adsorption when treated with a +U correction. Another notable difference is the electronic destabilization of [Al₁₂Co] upon CO₂ adsorption which can be seen in the decrease of the ionization potential in comparison to the isolated cluster. The adsorption energy of the Mn-doped cluster has a positive sign which can be interpreted as an unstable adsorption product which would result in spontaneous desorption. This is surprising since our relaxed structure appeared to be well converged.

Despite these four differences, the large majority of results is qualitatively in excellent agreement with the results obtained from the uncorrected LDA calculations. Hybridizations calculated from the pDOS(Figures 3.9 and 3.12) as well as absorption spectra (Figure 3.13) are also in good agreement with the LDA results. It is worth noting that +U is an empirical parameter, so it is not a priori clear if the results obtained through this correction are indeed more accurate than those of simple LDA. It could well be that 6 eV is might result in too strong correlation in some systems or might be too weak for others which would then result in unphysical results. Testing different +Us though and finding the best parameter is a task that would go beyond this work and would require experimental data which is not available. In total only four values changed and 5 of the 7 systems remained completely unaffected. We further concluded that the minor discrepancies found do not affect the overall results of CT in a meaningful way which is the focal

point of our work. On this basis we do not include a Hubbard U for the larger systems $[Al_{54}M]-CO_2$ and $[Al_{146}M]-CO_2$.

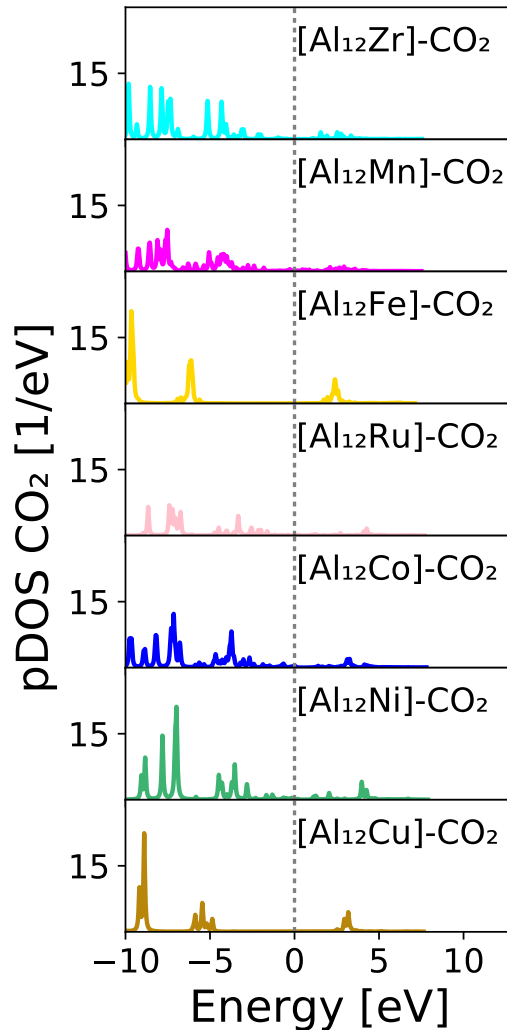


Figure 3.12: LDA +U results for the DOS projected onto 2s- and 2p-character atomic orbitals of CO_2 for the systems. The energy scale is shifted by the system’s respective Fermi-level which is denoted by a grey vertical line. A broadening of 0.05 eV has been used in all graphs. A Hubbard +U correction of 6 eV was applied to all transition-metal doped systems.

3.2.2 Excited State Properties

In the previous subsection we have focused on ground-state properties such as spin-multiplicity, adsorption energies and ground-state electron transfer just to name a few. We found that the bent CO_2 geometries go hand in hand with additional charge located on the carbon dioxide molecule. In this subsection we will focus on excited-state properties like adsorption spectra which we also computed for a Hubbard +U correction of 6 eV. We will establish a method to determine if a cluster is capable of transferring electrons into CO_2 upon excitation without having to integrate over all excited-state densities. We will

justify this approach by comparison of our results to some computed transition densities.

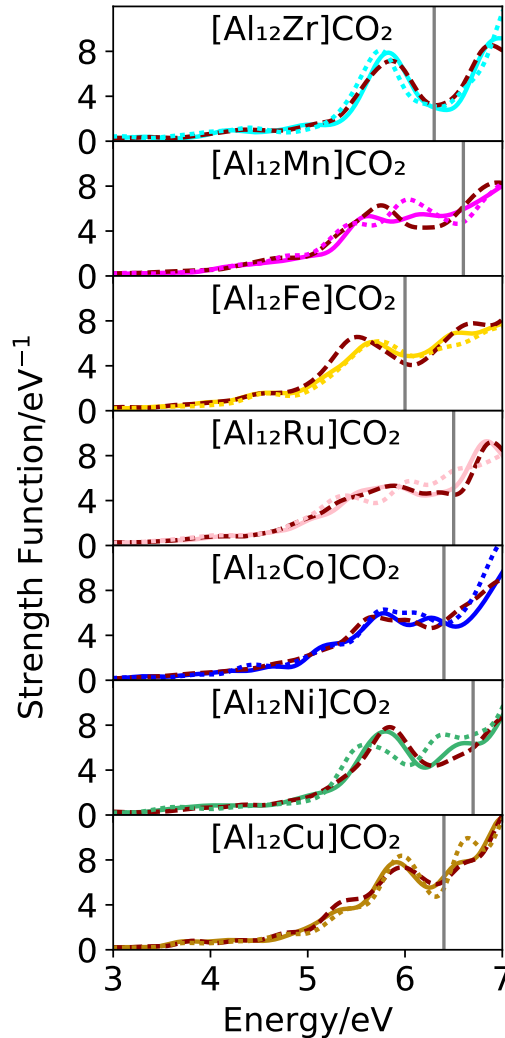


Figure 3.13: Absorption spectra of the isolated clusters (dashed coloured lines) and of the clusters with CO_2 (solid lines). The strength function is proportional to the absorption cross section (see chapter 2, section 2.7). The results for the respective clusters with CO_2 and a Hubbard $+U$ correction of 6 eV are represented by the dark red dashed line in each graph. The vertical grey line marks the first vertical ionization energy of each system.

We calculated absorption spectra using time-propagations. The results for $[\text{Al}_{12}\text{Zr}]-\text{CO}_2$, $[\text{Al}_{12}\text{Mn}]-\text{CO}_2$, $[\text{Al}_{12}\text{Fe}]-\text{CO}_2$, $[\text{Al}_{12}\text{Ru}]-\text{CO}_2$, $[\text{Al}_{12}\text{Co}]-\text{CO}_2$, $[\text{Al}_{12}\text{Ni}]-\text{CO}_2$ and $[\text{Al}_{12}\text{Cu}]-\text{CO}_2$ as well as their respective isolated cluster and the spectra of the systems obtained with a Hubbard U of 6 eV are displayed in Figure 3.13.

All spectra start exhibiting absorption from 3 eV on with the maximum adsorption lying in the ultra-violet region between 5 eV and 6 eV. The exact shapes of the spectra vary with different transition-metal dopants and cluster geometries. $[\text{Al}_{12}\text{Zr}]-\text{CO}_2$ exhibits one strong peak and has a perfectly icosahedral structure while $[\text{Al}_{12}\text{Co}]-\text{CO}_2$ and $[\text{Al}_{12}\text{Cu}]-\text{CO}_2$, which are both highly distorted icosahedra, show a pre-peak to the maximal absorption energy. This is also in good agreement with the dominant peak below the

Fermi energy in the Al pDOS of $[Al_{12}Zr]-CO_2$ while all other clusters show a more even distribution of states in this region. On the other hand, clusters with similar geometries but different dopants like $[Al_{12}Fe]-CO_2$ and $[Al_{12}Ru]-CO_2$ also exhibit different shapes in terms of their peak structure. Comparison of the dashed and the solid lines (corresponding to the isolated clusters and the adsorbed systems, respectively) shows that CO_2 does not affect the adsorption spectra in a major way which can be explained by its large HOMO-LUMO gap (roughly 8.5 eV[95]). However, the differences seem to be biggest for $[Al_{12}Zr]-CO_2$, $[Al_{12}Mn]-CO_2$, $[Al_{12}Ru]-CO_2$, $[Al_{12}Co]-CO_2$ and $[Al_{12}Ni]-CO_2$ which is not surprising since these systems show CO_2 activation and hence the strongest interactions with the molecule. For example, the adsorption of CO_2 leads to a noticeable blue-shift of the main peak in $[Al_{12}Ni]-CO_2$. Comparison to the +U corrected spectra did not lead to significantly different results.

In order to investigate electron-transfer between clusters and CO_2 in the excited state, we also performed linear response TDDFT calculations. The straightforward approach would be to integrate over the density of each excited state within a volume element defined around CO_2 . However, this would require an immense amount of memory and would hence consume a lot of computational resources. This is a reasonable approach if the excitation of interest is known. However, for screening all excitations for possible CT, a different path needs to be taken. We propose another approach that combines the information obtained from solving Casida's equation[77] with the results from the pDOS which will give us a measure for the change in CO_2 charge upon excitation of the system. We call this quantity light-induced charge-transfer (LICT).

In the Casida equation, ω_I are the solutions of the eigenvalue problem with the interpretation of excitation energies. The squares of the Casida matrix eigenvector elements $F_{I,cv}$ can be treated as coefficients of single Kohn-Sham wave functions that give an approximation of the excited state wave function, similar to a linear combination of atomic orbitals (LCAO) approach.[77] To be more precise, a singly excited Slater determinant $|\Psi_{cv}\rangle = a_c^\dagger a_v |\Psi_0\rangle$ can be expressed through the coefficients $C_{I,cv} = \sqrt{(\epsilon_c - \epsilon_v)/\omega_I} F_{I,cv}$. Here, I denotes the excited state, ϵ_c is the eigenenergy of the occupied Kohn-Sham state, ϵ_v is the eigenenergy of the unoccupied Kohn-Sham state, Q_I and Q_0 stand for the amount of charge distributed on CO_2 in the excited state I and in the ground-state, f_I is the oscillator strength and finally, q_c and q_v stand for the amount of charge localized on CO_2 for each occupied and unoccupied Kohn-Sham wave function:

$$LICT_I = f_I(Q_0 - Q_I) = f_I \sum_{cv} (q_c - q_v) |C_{I,cv}|^2. \quad (3.1)$$

The quantities q_c and q_v are obtained from the pDOS by integration over each peak that has been filtered out with a heavy-side function that was narrow enough to separate neighbouring peaks. In order to be able to treat degeneracies and make sure that each state's total charge equals 1, a normalization factor of $\int (pDOS_{peak}/DOS_{peak})dE$ is applied to the integral, with $pDOS_{peak}$ denoting the pDOS of CO_2 and DOS_{peak} standing for the total DOS, both multiplied with the same heavy-side function used to select the peak. It

3 Results and Discussion

should be noted that a positive LICT value refers to electrons being transferred from the cluster into the CO₂ molecule. Since excited state charge-transfer is often analysed using transition densities, we computed these for some distinctive LICT values. The results are displayed in Table 3.8.

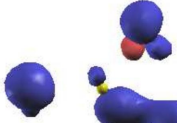


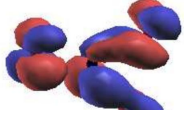
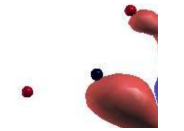

System	Excitation energy [eV]	LICT [e]	Transition density
[Al ₁₂ Mn]–CO ₂	6.33	-0.006	
[Al ₁₂ Co]–CO ₂	5.14	-0.005	
[Al ₁₂ Cu]–CO ₂	1.50	0.000	
[Al ₁₂ Ru]–CO ₂	1.00	0.000	
[Al ₁₂ Zr]–CO ₂	4.02	+0.002	
[Al ₁₂ Fe]–CO ₂	5.47	+0.003	

Table 3.8: Examples of transition densities for large positive, large negative and values of zero for the LICT. For better visibility, the pictures are centred on CO₂. Blue means charge is leaving a region while red means charge in that area is increased.

For the verification of our approach we tested three different extreme cases: We selected large positive values of the LICT, large negative values and values of zero LICT. The pictures are centred on CO₂ with blue meaning that charge is leaving a region compared to the ground state, while red means an increase of charge in the respective area. In both cases of large negative LICT values (first two examples) it can be seen that blue is the

predominant colour around CO_2 . The same can be said for red in the cases of the three large positive LICT examples (last two examples). On the other hand, for zero LICT we can distinguish between two different cases: The third example displays a case, where no change in charge can be seen at CO_2 . The fourth example, on the other hand, exhibits equal amounts of regions that are losing (blue) and regions that are gaining charge (red) at the CO_2 . This can be interpreted as intra-molecular excitations in CO_2 . This illustrates that our method is capable of capturing all of these cases sufficiently and hence should be a reasonable approach to filter out transitions of interest in an efficient way.

Figure 3.14 displays the results from our LICT analysis plotted against the excitation energy. It can be seen that $[Al_{12}Fe]$ and $[Al_{12}Cu]$ only display positive LICT values which means that these systems are only capable of transferring electrons from the cluster into the molecule. This is especially interesting since these systems did not result in ground-state CO_2 activation and electron transfer. Their LUMOs are located far below the Fermi energy (see Figure 3.9), although the $[Al_{12}Fe]-CO_2$ -LUMO is located at a higher energy compared to that of $[Al_{12}Cu]-CO_2$. This explains the onset of LICT for $[Al_{12}Fe]-CO_2$ at lower excitation energies. On the other hand, $[Al_{12}Mn]$, $[Al_{12}Ru]$ and $[Al_{12}Ni]$ mostly exhibit negative LICT values, resulting in electron transfer from the molecule to the clusters. Since all of these systems exhibited ground-state charge-transfer (see Table 3.3), this can be explained as "back-transfer" of the formerly transmitted electrons. This is most dominant in $[Al_{12}Ru]-CO_2$ with back-transfer already occurring for relatively low excitation energies such as ~ 2 eV which is located in the visible region of the optical spectrum. Again, this can be explained by the pDOS (Figure 3.9) with $[Al_{12}Ru]-CO_2$ exhibiting multiple small peaks close to the Fermi energy. The small LICT values at comparably high excitation energies that can be found in $[Al_{12}Mn]-CO_2$ can be explained by the change in spin-multiplicity from sextet to doublet which the system undergoes upon CO_2 adsorption. This makes a back-transfer less favourable compared to other systems like $[Al_{12}Ru]-CO_2$ where the spin-state remains unchanged. The other system that undergoes a change of spin-state upon adsorption is $[Al_{12}Co]-CO_2$, which explains the onset of LICT at comparably high energies. However, in $[Al_{12}Co]-CO_2$, $[Al_{12}Ni]-CO_2$ as well as in $[Al_{12}Zr]-CO_2$, LICT with positive and negative signs can be observed. Both $[Al_{12}Co]-CO_2$ and $[Al_{12}Zr]-CO_2$ only show a small change in ionization energy upon adsorption which indicates that the electrons resulting in further charge-transfer from the cluster into the molecule come from delocalized cluster orbitals. This would result in a lower energy cost due to weaker electron-electron repulsion (analogous to the Nephelauxetic effect[61] discussed above).

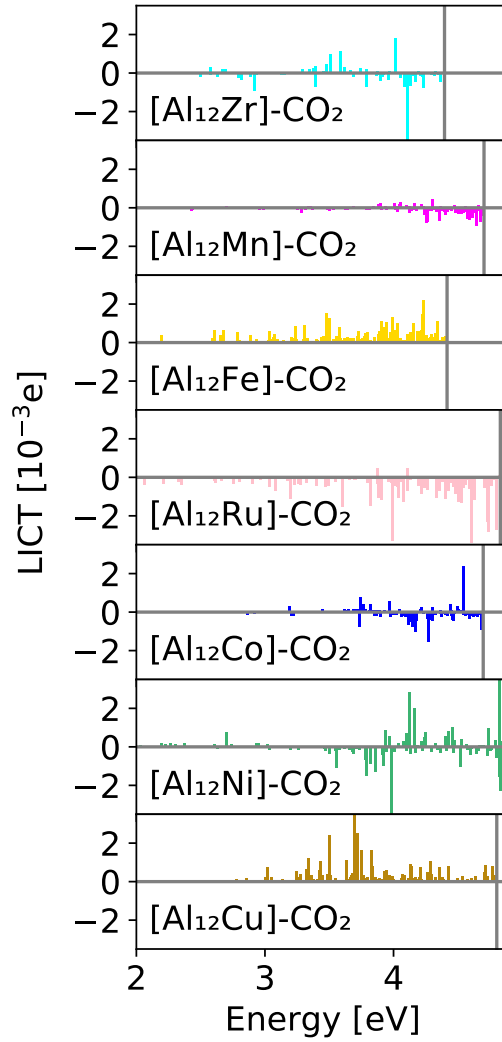


Figure 3.14: Light induced charge-transfer (LICT) in units of elementary charge plotted against its respective Casida excitation energy. The grey vertical lines denote the energy at which the excited states and therefore the LIC T values (as defined in equation 3.1) contain more than 5 % of contributions from states above the vacuum level. This figure has been published in [93].

From Figures 3.10 and 3.11 it can be seen that $[\text{Al}_{12}\text{Ru}]-\text{CO}_2$, $[\text{Al}_{12}\text{Ni}]-\text{CO}_2$ and $[\text{Al}_{12}\text{Co}]-\text{CO}_2$ all exhibit a comparably large peak in the Al pDOS at 1 eV. These systems have in common that they show the largest amounts of back-transfer upon excitation. Below the Fermi energy, especially $[\text{Al}_{12}\text{Ru}]-\text{CO}_2$ shows multiple high intensity peaks at -1 eV. While the Zr-doped cluster exhibits a peak below the Fermi energy that is even higher in intensity than the largest peak in this region from the Ru-doped cluster, it is lower in energy. On the other hand, the Mn-doped cluster's peaks below the Fermi energy in the Al pDOS are much smaller than those of $[\text{Al}_{12}\text{Zr}]-\text{CO}_2$, $[\text{Al}_{12}\text{Ru}]-\text{CO}_2$, $[\text{Al}_{12}\text{Co}]-\text{CO}_2$ and $[\text{Al}_{12}\text{Ni}]-\text{CO}_2$ which are the other clusters which resulted in ground-state activation of CO_2 . This could be an explanation for the overall small LIC T values and the late onset of LIC T in $[\text{Al}_{12}\text{Mn}]-\text{CO}_2$.

For the systems which did not yield activated CO_2 at the ground-state level, there are only small differences in the Al pDOS. However, looking at the transition-metal pDOS

(figure 3.11) yields a possible explanation for the later onset of LICT in $[Al_{12}Cu]-CO_2$: For the Fe-doped cluster, multiple small peaks can be seen around the Fermi-energy. On the other hand, the Cu-doped cluster exhibits a high intensity peak at -2.5 eV in the transition-metal pDOS. This should result in a smaller and sharper energy window in which LICT is taking place. On the other hand, the spreading of the states below the Fermi energy over a larger energy window for $[Al_{12}Fe]-CO_2$ results in a more even distribution of LICT for this system. However, the interplay between Al and transition-metal states seems to be complicated which is enhanced by the high levels of hybridisation. While for the Fe- and Cu-doped systems it is possible to draw conclusion, the nature of the LICT for the other systems is mostly a matter of speculations.

3.2.3 Summary

For five of the seven studied systems ($[Al_{12}Zr]-CO_2$), ($[Al_{12}Mn]-CO_2$), ($[Al_{12}Ru]-CO_2$), ($[Al_{12}Co]-CO_2$) and ($[Al_{12}Ni]-CO_2$)) we observed CO_2 activation, ground-state level CT and electronic stabilization upon CO_2 adsorption. Systems without CO_2 activation ($[Al_{12}Fe]-CO_2$ and $[Al_{12}Cu]-CO_2$) seem to be electronically destabilized by CO_2 . Only ($[Al_{12}Mn]-CO_2$) and ($[Al_{12}Co]-CO_2$) undergo a change in spin-multiplicity upon CO_2 adsorption. All adsorbed systems have a low-spin configuration as their ground state except for the Fe doped cluster which has its most electronically favourable structure as a high-spin configuration, resulting in a quintet. Adsorption energies of CO_2 indicate that adsorption is energetically favourable which is in agreement with the relaxed structures. Adsorption energy increases with decreasing adsorption distance.

Findings are further supported by the ELF, pDOS and HOMO-shapes. The changes in the pDOS of the systems exhibiting ground-state CT compared to that of isolated CO_2 exhibit the energies of the hybridized states that contain the electrons that have been transferred upon the CO_2 molecule. From the ELFs it can be seen that the additional charge is located in a lobe pointing from the carbon atom towards the dopant. These adsorption geometries are expected to mostly result in CO as a product of further reactions due to the steric hindrance of attacks to the carbon atom resulting from the carbon or mixed coordination of the molecule.[96] This CO can then be facilitated in further reactions like Fischer-Tropsch synthesis resulting in a distribution of useful products depending on the catalyst and reaction conditions[97]. The only systems which exhibit oxygen coordination and would therefore be expected to directly yield products like e.g. methanol or formic acid are the Fe- and Cu-doped clusters which makes their LICT especially interesting.

As for the excited state properties, we computed adsorption spectra for adsorbed and isolated systems. Results for all of the calculations with a Hubbard U of +6 eV did not lead to significantly different results. We were able to show that our approach of determining LICT was in good agreement with analysed transition densities. We saw only positive LICT for $[Al_{12}Fe]-CO_2$ and $[Al_{12}Cu]-CO_2$ which are the two systems that did not lead to ground-state CO_2 activation and electron transfer. This means that electrons are being transferred from the cluster onto CO_2 . The onset of this LICT occurs at a lower energy for the Fe-doped cluster than for the Cu-doped cluster. This can be explained by the different

3 Results and Discussion

energies of their transition-metal atom states. The Cu-doped cluster exhibits a clustering of states at a lower energy compared to the more even distribution up to the Fermi energy which can be seen in the Fe-doped cluster. $[\text{Al}_{12}\text{Mn}]-\text{CO}_2$, $[\text{Al}_{12}\text{Ru}]-\text{CO}_2$ and $[\text{Al}_{12}\text{Ni}]-\text{CO}_2$ mostly resulted in electron back-transfer from the molecule onto the cluster with the Ru-doped system exhibiting the lowest energy onset of LICT. The high energy onset of the Mn-doped cluster can be explained by its change in spin-state upon CO_2 adsorption, making electron transfer less favourable. $[\text{Al}_{12}\text{Zr}]-\text{CO}_2$, $[\text{Al}_{12}\text{Ni}]-\text{CO}_2$ and $[\text{Al}_{12}\text{Co}]-\text{CO}_2$ are capable of transferring electrons into both directions upon excitation which can be seen in their positive and negative LICT values.

3.3 Electronic Properties of $[\text{Al}_{54}M]-\text{CO}_2$

The electronic ground-state and excited-state properties of $[\text{Al}_{54}M]-\text{CO}_2$ with M being Zr, Mn, Fe, Ru, Co, Ni and Cu are investigated in this chapter. $[\text{Al}_{54}M]-\text{CO}_2$ is an icosahedral cluster with two atomic shells around the central Al atom. Again, one of the outer atoms is exchanged for a dopant. We computed the same properties as in the previous chapter (chapter 3.2), namely spin multiplicity of the adsorbed and the isolated cluster, ionization energies for the isolated system as well as the adsorbed geometry, adsorption energies, dopant electron configuration, ground-state charge-transfer into CO_2 , pDOS, absorption spectra and LICT. This gives us the opportunity to study the size-dependence of these quantities.

3.3.1 Ground State Properties

In this subsection we will focus on a variety of ground-state properties like spin-multiplicity, adsorption energies, ELF's and the pDOS just to name a few. We will put our combined findings for the medium-sized clusters into perspective considering the results obtained for the small clusters in a separate paragraph at the end of this section.

System	Spin-state	Vertical ionization Energy [eV]	Adsorption Energy [eV]	GS CT into CO_2 [-e]
$[\text{Al}_{54}\text{Zr}]-\text{CO}_2$	singlet (singlet)	5.3 (5.2)	-2.2	+0.38
$[\text{Al}_{54}\text{Mn}]-\text{CO}_2$	doublet (doublet)	5.5 (5.4)	-2.2	+0.29
$[\text{Al}_{54}\text{Fe}]-\text{CO}_2$	singlet (singlet)	5.4 (5.4)	-0.4	-0.07
$[\text{Al}_{54}\text{Ru}]-\text{CO}_2$	singlet (singlet)	5.5 (5.3)	-1.5	+0.45
$[\text{Al}_{54}\text{Co}]-\text{CO}_2$	doublet (doublet)	5.4 (5.3)	-1.5	+0.38
$[\text{Al}_{54}\text{NiO}]-\text{CO}$	singlet (singlet [Al_{54}Ni]) (singlet [Al_{54}NiO])	5.4 (5.3 for [Al_{54}Ni]) (5.4 for [Al_{54}NiO])	-2.7 (for CO_2) -2.2 (for CO)	+0.65 (into CO_2) +0.29 (into CO)
$[\text{Al}_{54}\text{Cu}]-\text{CO}_2$	doublet (doublet)	5.3 (5.3)	-0.1	+0.02

Table 3.9: Electronic ground-state data of $[\text{Al}_{54}M]$ with adsorbed CO_2 , values for the isolated clusters are written in brackets. Results include the spin multiplicity, ionization energy, adsorption energy and the ground-state electron transfer (GS CT) into CO_2 (evaluated by Hirshfeld's scheme). Here, a positive value for GS CT means that electrons are being transferred from the cluster into the CO_2 molecule.

The results for the most favourable spin-state, ionization energy, adsorption energy and ground-state electron transfer are summarized in Table 3.9. The ground-state multiplicity and ionization energies of the isolated relaxed clusters are displayed in brackets. All systems have their most stable configuration in the lowest possible spin-state. This is true for the isolated clusters as well as the adsorbed structures. Ionization energies range from 5.3 eV to 5.5 eV. The small differences between systems can be explained by the

smaller dopant fraction compared to the overall atom number. This evens out differences among the systems. Electronic stabilization due to CO_2 adsorption can be observed in $[Al_{54}Zr]-CO_2$, $[Al_{54}Mn]-CO_2$, $[Al_{54}Ru]-CO_2$, $[Al_{54}Co]-CO_2$ and $[Al_{54}Ni]-CO_2$. No system is electronically destabilized upon CO_2 adsorption, the ionisation energies in the Fe- and Cu-doped systems remain unchanged. However, when it comes to adsorption energies, the values cover a wide range from -0.1 eV to -2.2 eV (or -2.7 eV for adsorption of CO_2 on $[Al_{54}Ni]$). The negative signs indicate stable adsorption which should be the case since the structures have been obtained from geometry relaxations. For the Ni doped cluster, we computed adsorption energies both for CO_2 on $[Al_{54}Ni]$ and CO on $[Al_{54}NiO]$. The difference of 0.5 eV shows that desorption of CO is far more favourable than recombination of CO and the oxygen atom to CO_2 , indicating that the catalyst is being poisoned and will remain oxidized after desorption. It is unclear though how a full oxidation of the surface would impact the catalytic behaviour and if disintegration of CO_2 would still be possible.

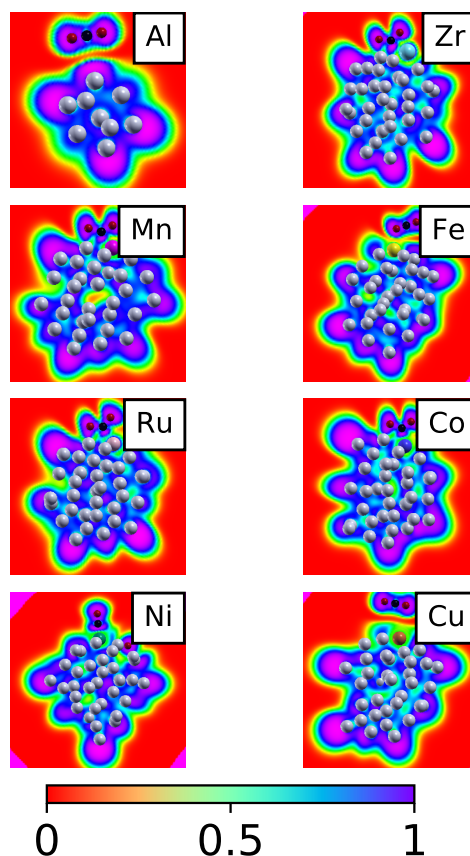


Figure 3.15: Electron Localization Function (ELF) of the transition-metal doped $[Al_{54}M]$ clusters with adsorbed CO_2 . For better comparison, the ELF of a neutral $[Al_{13}]$ cluster with CO_2 is also displayed (upper left picture).

Ground-state charge-transfer from the cluster into CO_2 (and CO for $[Al_{54}Ni]-CO_2$) can be observed for all systems with adsorption distances smaller than 2.0 Å, namely $[Al_{54}Zr]-CO_2$, $[Al_{54}Mn]-CO_2$, $[Al_{54}Ru]-CO_2$, $[Al_{54}Co]-CO_2$ and $[Al_{54}Ni]-CO_2$. It is worth noting that the Fe-doped cluster displays a small negative number of CT while

the Cu-doped cluster, despite its far smaller adsorption distance, exhibits a small positive number for ground-state electron transfer. Since charge-partitioning schemes all have certain flaws, this should be interpreted in a qualitative way, leading to the conclusion that there is no significant ground-state electron transfer.

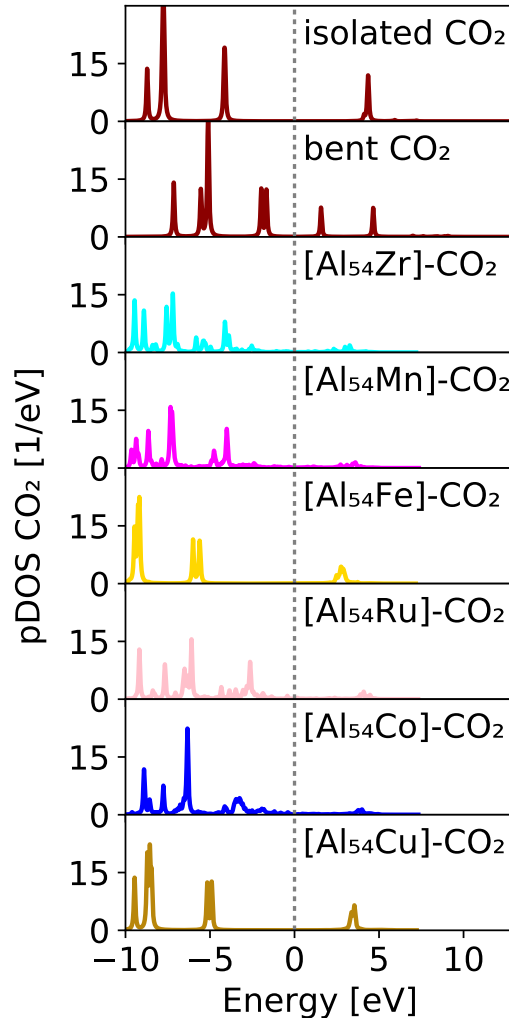


Figure 3.16: DOS projected onto 2s- and 2p-character atomic orbitals of CO_2 for the $[\text{Al}_{54}M]-\text{CO}_2$ systems. The energy scale is shifted by the system’s respective Fermi-level which is denoted by a grey vertical line. For better comparison, the DOSs of isolated linear and bent carbon dioxide are displayed at the top. A broadening of 0.05 eV has been used in all graphs.

Figure 3.15 displays the ELF’s of the medium-sized clusters and $[\text{Al}_{13}]$ with adsorbed CO_2 . The $[\text{Al}_{54}M]-\text{CO}_2$ systems exhibit large regions of highly localized electrons with values close to unity. In contrast to $[\text{Al}_{13}]$ though, delocalized electrons can be found within the clusters. This appears to be most dominant in the Mn- and Fe-doped clusters and can be seen in the appearance of green spots within the cluster which correspond to values of the EF of 0.5. This shows that the electronic character is more delocalized than that of the $[\text{Al}_{12}M]-\text{CO}_2$ systems and although these systems still mostly display localized electrons,

metallic areas appear. This is in good agreement with the increased size and electron number which results in more states and hence a more metal-like character.

In Figure 3.16 the DOS projected onto the 2s- and 2p-character atomic orbitals of carbon and oxygen is plotted. For comparison we also display the DOS of isolated CO_2 . The two systems with larger adsorption distances and linear carbon dioxide geometries, $[Al_{54}Fe]-CO_2$ and $[Al_{54}Cu]-CO_2$, resemble the pDOS of isolated CO_2 , although the degeneracy of the HOMO appears to be slightly broken. All other systems display a multitude of smaller additional peaks below the Fermi level while their peaks above the Fermi energy are smaller than those of $[Al_{54}Fe]-CO_2$ and $[Al_{54}Cu]-CO_2$. $[Al_{54}Ru]-CO_2$ has the pDOS that closest mimicks that of an angles CO_2 molecule, however, the results for $[Al_{54}Zr]-CO_2$, $[Al_{54}Mn]-CO_2$ and $[Al_{54}Co]-CO_2$ also resemble the bent CO_2 pDOS although the hybridisations in these systems seem to be stronger which result in stronger alterations to the pDOS. Due to its different adsorption character, we displayed the results for the pDOS of $[Al_{54}NiO]-CO$ in a separate graph (Figure 3.17). It can be seen that the system's pDOS mostly resembles that of isolated CO with multiple smaller peaks arising which can be explained by the CT into CO which was seen in the Hirshfeld analysis. The LUMO seems to be highly hybridised which results in a much smaller peak intensity above the Fermi level and the states appear to be red-shifted in comparison to those of isolated CO.

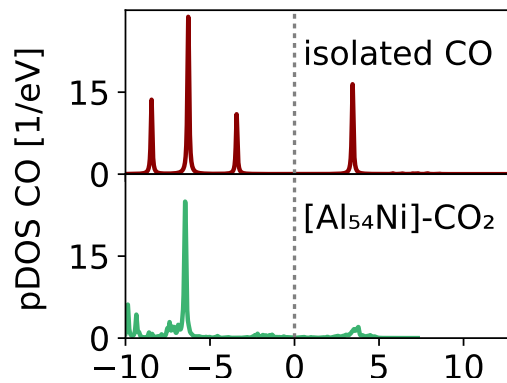


Figure 3.17: DOS projected onto 2s- and 2p-character atomic orbitals of CO for the $[Al_{54}NiO]-CO$ systems. The energy scale is shifted by the system's respective Fermi-level which is denoted by a grey vertical line. For better comparison, the DOS of isolated carbon monoxide is displayed at the top. A broadening of 0.05 eV has been used in all graphs.

We do not display the Al pDOS like in the previous section since it is hard to draw conclusions due to the large amount of states that are close in energy which can be explained by the larger number of atoms in the cluster which results in a DOS that is approaching a continuum. This can also be seen in the ELF which is starting to show more regions of delocalization. Figure 3.18 displays the transition-metal pDOS of the $[Al_{54}M]-CO_2$ systems.

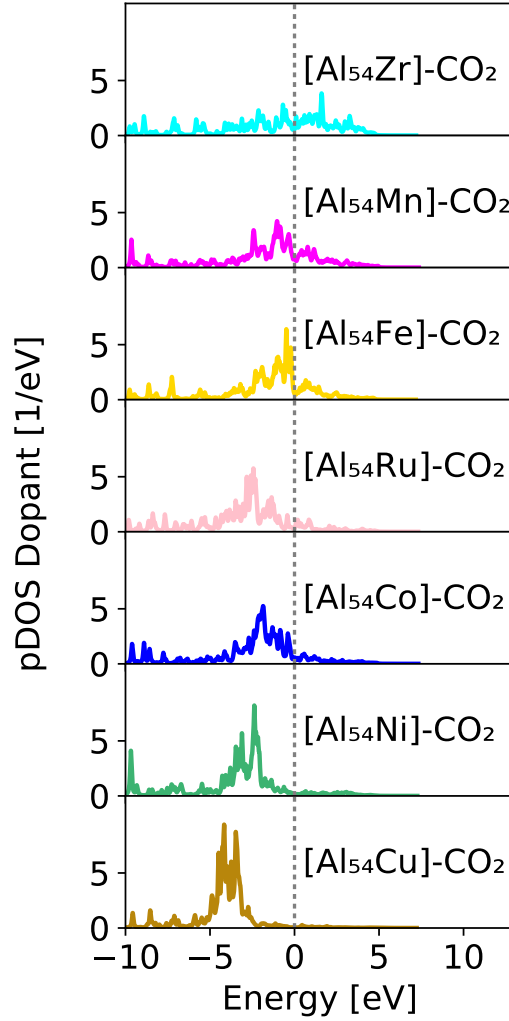


Figure 3.18: DOS projected onto atomic orbitals of the dopant for the $[\text{Al}_{54}M]$ systems. The energy scale is shifted by the system's respective Fermi-level which is denoted by a grey vertical line. A broadening of 0.05 eV has been used in all graphs.

The differences between the dopants are notable. $[\text{Al}_{54}\text{Zr}]\text{-CO}_2$ exhibits many evenly spread peaks with a high intensity peak above the Fermi energy. $[\text{Al}_{54}\text{Mn}]\text{-CO}_2$ and $[\text{Al}_{54}\text{Fe}]\text{-CO}_2$ exhibit many small peaks as well but they seem to be higher in intensity around the Fermi energy. For $[\text{Al}_{54}\text{Ru}]\text{-CO}_2$ and $[\text{Al}_{54}\text{Co}]\text{-CO}_2$ the transition-metal states appear to have their maximum concentration below the Fermi energy at roughly -2.5 eV. For the Ni- and the Cu-doped systems, the maximum of the peaks is shifted to even lower energies (about -4 to -5 eV with the Cu states being the lowest in energy). In the cases of $[\text{Al}_{54}\text{Ni}]\text{-CO}_2$ and $[\text{Al}_{54}\text{Cu}]\text{-CO}_2$ there is no notable peaks above the Fermi energy.

M	El. conf.	Partial charge	s	p	d	Dopant spin
Zr	$[Kr]4d^25s^2$	+0.4 (+0.3)	8.4 (8.5)	18.4 (18.2)	12.8 (13.0)	0 (0)
Mn	$[Ar]3d^54s^2$	-0.1 (-0.1)	6.6 (6.6)	12.4 (12.3)	6.1 (6.2)	0.2 (0.5)
Fe	$[Ar]3d^64s^2$	-0.4 (-0.4)	6.7 (6.7)	12.6 (12.5)	7.2 (7.1)	0 (0)
Ru	$[Kr]4d^75s^1$	-0.1 (-0.1)	8.5 (8.6)	18.6 (18.5)	17.0 (17.1)	0 (0)
Co	$[Ar]3d^74s^2$	-0.3 (-0.3)	6.8 (6.8)	12.6 (12.5)	8.0 (8.0)	0.1 (0.1)
Ni	$[Ar]3d^84s^2$	-0.2 (-0.2)	6.8 (6.8)	12.5 (12.5)	8.9 (8.9)	0 (0)
Cu	$[Ar]3d^{10}4s^1$	-0.3 (-0.3)	6.9 (6.9)	12.8 (12.8)	9.6 (9.6)	0 (0)

Table 3.10: Angular momentum-resolved Mulliken charges of the dopant atoms in $[Al_{54}M]-CO_2$. Results were obtained with FHI-aims, values for the isolated clusters are displayed in brackets. "El. conf." denotes the electron configuration of the isolated dopant atom and "s", "p" and "d" denote the amount of electrons of the respective character.

Table 3.10 shows the results from the angular momentum-resolved Mulliken analysis for the adsorbed systems and the isolated clusters. Partial dopant charges range from -0.4 in $[Al_{54}Fe]-CO_2$ and $[Al_{54}Fe]$ to +0.4 in $[Al_{54}Zr]-CO_2$. Changes in dopant charge upon adsorption are negligible. In terms of electron configuration of the dopant it can be seen that all systems follow the principle that the amount of d-electrons equals the position in the d-period plus one. The spin located on the dopant is reduced by one compared to the total spin-moment of the cluster or adsorbed system (unless it is a singlet, then it remains without spin moment).

3.3.2 Excited State Properties

In this subsection we will discuss the absorption spectra obtained from time-propagations and perform the same LICT analysis as in 3.2. The combined results will be compared to the small clusters in a separate subsection at the end of this section.

For the medium-sized systems we computed spectra from time-propagations which are displayed in Figure 3.19. The onset of absorption is located between 3 eV and 4 eV. The maximum of the main absorption peak is located at about 8 eV which is above the respective ionization energy of all structures. All clusters exhibit highly distorted icosahedral geometries which result in shoulders and double peaks, depending on the structure and the dopant. Interestingly, $[Al_{54}NiO]-CO$ does not deviate from the other systems in terms of absorption despite its different adsorption behaviour. This can be explained by the weak adsorption of CO in this spectral region.

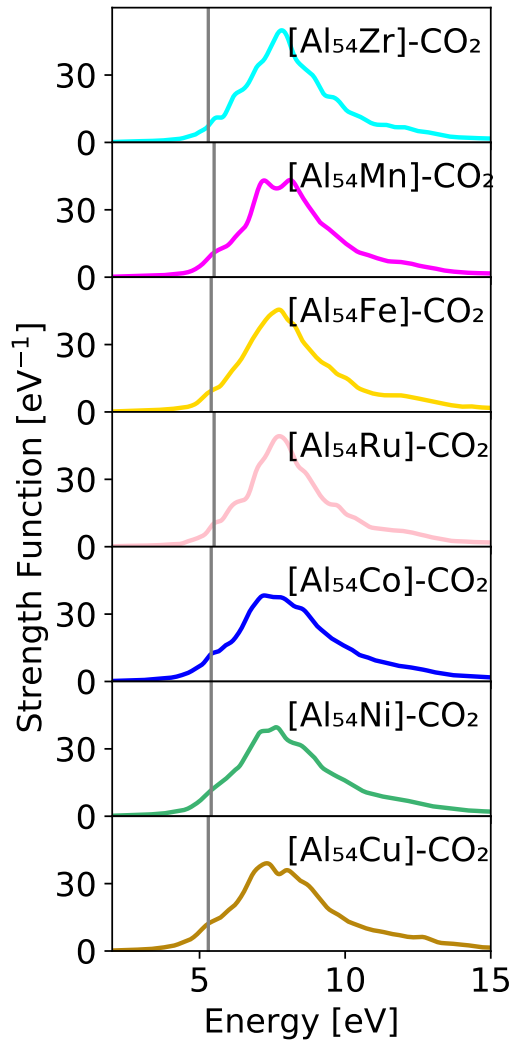


Figure 3.19: Absorption spectra of the the $[\text{Al}_{54}M]$ clusters with CO_2 . The vertical grey line marks the first vertical ionization energy of each system.

Figure 3.20 displays the results of the LICT analysis. It exhibits significant CT excitations starting from 2 eV on for systems with adsorbed CO_2 . The LICT analysis of the Ni-doped cluster was carried out for transitions into CO instead of CO_2 . It is worth noting that LICT values for the Ni-doped cluster are about two orders of magnitude larger which can be explained by the smaller stability of CO in comparison to CO_2 (for comparison: CO can be directly used as "synthesis gas" in chemical reactions like Fischer-Tropsch while CO_2 needs to undergo activation before it can be facilitated as a carbon source[4, 97]). $[\text{Al}_{54}\text{Fe}]-\text{CO}_2$ and $[\text{Al}_{54}\text{Cu}]-\text{CO}_2$ only display positive LICT values. Interestingly, the Fe-doped cluster exhibits notable charge-transfer excitations into CO_2 from 2.5 eV on while the Cu-doped cluster's excitations start above 3 eV. This behaviour can be explained by the different adsorption distances: The Fe-doped cluster has a moderate adsorption distance of 2.3 Å while the Cu-doped cluster has a large distance of 3.7 Å, making electron-transfer less likely and energetically more expensive. On the other hand, the Cu-doped cluster also displays a large gap between its highest occupied transition-metal state and the Fermi energy which could further complicate charge-transfer if the transition-metal electrons play a crucial role within the process. $[\text{Al}_{54}\text{Mn}]-\text{CO}_2$, $[\text{Al}_{54}\text{Ru}]-\text{CO}_2$ and

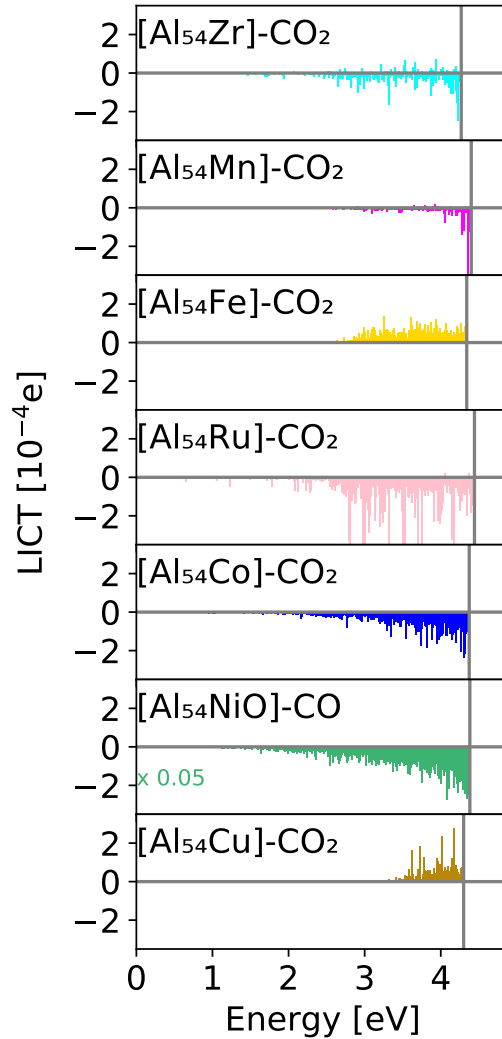


Figure 3.20: Light induced charge-transfer (LICT) in units of elementary charge plotted against its respective Casida excitation energy. The grey vertical lines denote the energy at which the excited states and therefore the LIC T values (as defined in equation 3.1) contain more than 5 % of contributions from states above the vacuum level.

$[Al_{54}Co]-CO_2$ in contrast predominantly exhibit negative LIC T values. In the case of the Mn-doped cluster it is worth noting that the onset of larger LIC T values is at a much higher energy (3.5 eV) as that of the other systems that exhibit ground-state CO_2 activation. The origin of this can not be explained by the adsorption distance since with 1.9 Å, the Mn-doped system has one of the smallest distances of all clusters. $[Al_{54}Mn]-CO_2$ also does not undergo a change of spin state upon adsorption which we suspected to be the reason for the high energy LIC T onset in $[Al_{12}Mn]-CO_2$. The transition-metal pDOS of the Mn-doped cluster does not show a large gap between the highest occupied transition-metal state and the Fermi energy like in the case of the Cu-doped cluster. The reason for the onset of LIC T at higher energies in $[Al_{54}Mn]-CO_2$ has to have a different origin which is not clear at this point. The only medium sized system that displays both positive and negative LIC T values is $[Al_{54}Zr]-CO_2$ which could be a result of the evenly spread peaks in the transition-metal dopant pDOS that reach beyond the Fermi energy.

3.3.3 Comparison of the results to $[\text{Al}_{12}M]-\text{CO}_2$

In this subsection we will compare our combined results of the $[\text{Al}_{54}M]-\text{CO}_2$ systems to the same quantities obtained for the $[\text{Al}_{12}M]-\text{CO}_2$ systems. We will discuss if general concepts can be derived from our findings and what effects the cluster size has on the physical properties and catalytic behaviour. We found that LICT is roughly one order of magnitude smaller than in the $[\text{Al}_{12}M]-\text{CO}_2$ systems but there are more transitions. For a better comparison, we will sum the LICT over transitions for each system and discuss the implications of these findings on possible future catalytic applications.

In terms of structures, $[\text{Al}_{54}\text{Fe}]-\text{CO}_2$ and $[\text{Al}_{54}\text{Cu}]-\text{CO}_2$, like their smaller counterparts, exhibit linear CO_2 geometries. The other systems lead to bent CO_2 structures similar to the ones observed in $[\text{Al}_{12}M]-\text{CO}_2$ with M being either Zr, Mn, Ru and Co. The main difference between the medium-sized clusters and the small systems appears in the adsorption geometry of $[\text{Al}_{54}\text{Ni}]-\text{CO}_2$. Instead of just activating CO_2 , leading to a bent geometry, adsorption of CO_2 on $[\text{Al}_{54}\text{Ni}]$ results in dissociation of the molecule, meaning the surface of the cluster becomes oxidized and CO is adsorbed to the dopant. While for $[\text{Al}_{12}\text{Mn}]$, $[\text{Al}_{12}\text{Fe}]$ and $[\text{Al}_{12}\text{Co}]$ high spin configurations were most favourable (see chapter 3.2, Table 3.3), for $[\text{Al}_{54}M]$ only low-spin configurations could be observed. In the group of $[\text{Al}_{12}M]-\text{CO}_2$ systems, $[\text{Al}_{12}\text{Fe}]-\text{CO}_2$ was the only adsorbed system that had a high-spin configuration. For the bigger $[\text{Al}_{54}M]-\text{CO}_2$ systems, all ground-state configurations found are most favourable in the lowest possible spin state.

While ionization energies of the small systems fell into a range of 6.0 eV to 6.7 eV, ionization energies for $[\text{Al}_{54}M]$ systems (adsorbed and isolated) are shifted to lower energies (5.3 eV to 5.5 eV) and differences among the systems are generally smaller. Electronic stabilization through CO_2 activation can still be observed but appears to be weaker. This could be due to the larger cluster size which is capable of stabilizing unfavourable charges better since they can be delocalized over a larger area. Adsorption energies of $[\text{Al}_{12}M]-\text{CO}_2$ systems varied between -0.3 eV and -2.0 eV. In $[\text{Al}_{54}M]-\text{CO}_2$, a wider range of -0.1 eV to -2.2 eV (or -2.7 eV for CO_2 adsorption on $[\text{Al}_{54}\text{Ni}]$) can be observed. The reduction of differences in these values can be explained by the dopant fraction: While in $[\text{Al}_{12}M]-\text{CO}_2$ the dopant content resembled 1/13th (=8%) of the cluster, in the medium-sized systems it is only 1/55th (= 2%) which is about a quarter of the fraction of the small systems. As for the ground-state electron transfer, the results agree with the findings for $[\text{Al}_{12}M]$. All systems except for $[\text{Al}_{54}\text{Fe}]-\text{CO}_2$ and $[\text{Al}_{54}\text{Cu}]-\text{CO}_2$ are capable of ground-state level charge-transfer from the cluster into CO_2 (or CO in the case of $[\text{Al}_{54}\text{Ni}]-\text{CO}_2$). Results for the CO_2 pDOS show no major differences between the small and the medium-sized clusters except for $[\text{Al}_{54}\text{Ni}]-\text{CO}_2$. This can be explained by the dissociation of CO_2 on the cluster surface. As a result, the pDOS resembles that of CO (see Figure 3.17). The results of the transition-metal pDOS are also very similar between the different sized systems except for the Ni-doped clusters. For $[\text{Al}_{54}\text{Ni}]-\text{CO}_2$ more high-intensity peaks below the Fermi energy appear which are probably a result of strong hybridisations with the dissociated CO_2 molecule. Comparison of the results obtained through the Mulliken analysis exhibits the same trends in terms of electron-configuration: There is always one

more d-electron on the dopant than its position in the d-period. For the medium-sized clusters there is also no exception from the principle that the dopant-spin is the total spin minus one unless the total spin is a singlet, in this case the spin located on the dopant is also zero. In terms of dopant charge there is only minor differences in most cases between the small and medium-sized clusters. The exceptions are $[Al_{54}Mn]$, $[Al_{54}Fe]-CO_2$, $[Al_{54}Fe]$, $[Al_{54}Co]-CO_2$ and $[Al_{54}Co]$ which all exhibit an increase in dopant charge compared to the smaller systems.

In terms of absorption spectra (see Figure 3.19), it can be seen that absorption generally is much more intense than in the smaller systems which can be explained by the increased number of electrons resulting in more possible transitions. The onset of the absorption is located at similar energies like that of the $[Al_{12}M]-CO_2$ systems. Nevertheless, the structure of the absorption features is very different which can be explained by the different geometries (see Chapter 3.1). The maximum of the first absorption peak for the $[Al_{54}M]-CO_2$ systems is blue shifted by about 2 eV in comparison to that of the $[Al_{12}M]-CO_2$ systems. This in combination with the red-shift of the ionization energies results in the first absorption maximum lying outside of the window of interest for LICT studies. This does not necessarily mean though that LICT values are generally smaller since the large number of electrons can compensate this trend. Indeed, the dipole strength function of $[Al_{54}M]-CO_2$ systems reaches values of roughly 10 eV^{-1} at energies smaller than the first ionisation energy which is comparable to the magnitude of the first absorption maxima in $[Al_{12}M]-CO_2$.

Dopant	System	LICT sum [e]
Zr	$[Al_{12}Zr]-CO_2$	-0.0065
	$[Al_{54}Zr]-CO_2$	-0.0100
Mn	$[Al_{12}Mn]-CO_2$	-0.0149
	$[Al_{54}Mn]-CO_2$	-0.0110
Fe	$[Al_{12}Fe]-CO_2$	+0.0571
	$[Al_{54}Fe]-CO_2$	+0.0243
Ru	$[Al_{12}Ru]-CO_2$	-0.0575
	$[Al_{54}Ru]-CO_2$	-0.0419
Co	$[Al_{12}Co]-CO_2$	-0.0101
	$[Al_{54}Co]-CO_2$	-0.0522
Ni	$[Al_{12}Ni]-CO_2$	+0.0007
	$[Al_{54}Ni]-CO_2$	-1.2990 (CO!)
Cu	$[Al_{12}Cu]-CO_2$	+0.0512
	$[Al_{54}Cu]-CO_2$	+0.0186

Table 3.11: Summation over all LICT values of a system.

For the LICT analysis, it can be seen that—just like for the smaller clusters—systems without CO_2 activation only exhibit charge-transfer into CO_2 and systems with previous CO_2 activation are more likely to perform back-transfer of electrons from the CO_2 molecule onto the cluster. It is worth noting that for the medium-sized clusters this trend seems to be more rigid since only one system ($[Al_{54}Zr]-CO_2$) displays both positive and negative LICT

values. Interestingly, the positive values are much smaller than the negative ones which could not be observed for the smaller systems. Both Zr-doped systems, $[\text{Al}_{12}\text{Zr}]-\text{CO}_2$ and $[\text{Al}_{54}\text{Zr}]-\text{CO}_2$, exhibit positive and negative LICT. On the other hand, both Mn-doped systems, $[\text{Al}_{12}\text{Mn}]-\text{CO}_2$ and $[\text{Al}_{54}\text{Mn}]-\text{CO}_2$, have an onset of LICT at high energies. It is also worth noting that the LICT spectrum of all $[\text{Al}_{54}M]-\text{CO}_2$ systems shows more peaks due to the increased amount of electrons and resulting excitations. The magnitude of LICT is smaller than in the $[\text{Al}_{12}M]-\text{CO}_2$ systems by a factor of 10. This does not mean that fewer electrons will be transferred upon excitation though since the density of LICT per energy window is higher and electromagnetic pulses are never infinitely sharp in terms of frequency. For better comparison, we summed over the LICT of each system and compared the results (see Figure 3.11). It can be seen that the results are qualitatively comparable except for the case of the Ni-doped systems, which again can be explained by the dissociation of CO_2 on $[\text{Al}_{54}\text{Ni}]$ (note that we are not even comparing the same value in this case: for the medium-sized system, LICT into CO is considered while for the small system LICT into CO_2 is calculated!). Interestingly, most of the $[\text{Al}_{54}M]-\text{CO}_2$ systems start exhibiting LICT at much lower frequencies than their smaller counter parts: While $[\text{Al}_{12}\text{Co}]-\text{CO}_2$ for example started showing LICT from 3 eV on, $[\text{Al}_{12}\text{Co}]-\text{CO}_2$ already has noticeable LICT from 2 eV on which is well in the lower energy range of the visible spectrum (orange). Since we use a local XC functional this value can be shifted to the accurate result. However, the comparison of the different systems in terms of energy should be valid. The threshold at which more than 5% of contributions are from above the vacuum level is about 1 eV smaller in $[\text{Al}_{54}M]-\text{CO}_2$ compared to the smaller systems which can be explained by the smaller ionization energies.

3.3.4 Summary

The medium-sized clusters exhibit the same trends that could be observed in their smaller counter-parts. For the $[\text{Al}_{54}M]-\text{CO}_2$ systems ionization energies are red-shifted, adsorption energies are generally also shifted to smaller energies and no high-spin ground-states could be observed. Systems which exhibit significant ground-state CT show predominantly negative LICT values and systems which show weak CO_2 adsorption and no ground-state CT can transfer electrons into CO_2 upon excitation. Despite the location of the main absorption peak above the first ionization energy, the medium-sized clusters result in comparable LICT values upon summation over all excitations as their smaller counter-parts due to the increased amount of electrons and possible excitations. Similar to the smaller clusters, $[\text{Al}_{54}\text{Zr}]-\text{CO}_2$ exhibits both positive and negative LICT values. $[\text{Al}_{54}\text{Mn}]-\text{CO}_2$ just like $[\text{Al}_{12}\text{Mn}]-\text{CO}_2$ shows an onset of LICT at higher energies than the other systems. There is some deviations from the smaller clusters which manifest in the different adsorption behaviour of $[\text{Al}_{54}\text{NiO}]-\text{CO}$ and its different properties arising from it. Overall though it becomes clear that the $[\text{Al}_{54}M]-\text{CO}_2$ systems show similar trends like the smaller clusters and point out the catalytic activity of small doped Al clusters for carbon dioxide facilitation in renewable energies. Our work paves the way for better understanding of catalysts and gives hints at which systems are of interest to synthesize for further studies.

3.4 Electronic Properties of $[\text{Al}_{146}M]-\text{CO}_2$

In this chapter we explore the electronic structure of $[\text{Al}_{146}M]-\text{CO}_2$ with M denoting Zr, Mn, Ru, Co, Ni and Cu. We study the spin multiplicities and ionization potentials of the adsorbed and isolated systems as well as the adsorption energies, dopant electron configurations and the ground-state charge-transfer. We compare the results to those of $[\text{Al}_{12}M]-\text{CO}_2$ and $[\text{Al}_{54}M]-\text{CO}_2$ and discuss trends observed across the different sizes.

3.4.1 Ground State Properties

In this subsection we will look at the static properties of the biggest systems in our study, namely $[\text{Al}_{146}M]-\text{CO}_2$. Again we will discuss ground-state spin-multiplicities and ionization potentials of the isolated clusters as well as the adsorbed systems, look at adsorption energies, investigate if ground-state CT is taking place and compute the total DOS of each system projected onto an atomic orbital basis of CO_2 .

System	Spin-state	Ionization Energy/eV	Adsorption Energy/eV	GS CT into CO_2
$[\text{Al}_{146}\text{Zr}]-\text{CO}_2$	singlet (singlet)	5.2 (5.2)	-1.9	+0.33
$[\text{Al}_{146}\text{Mn}]-\text{CO}_2$	doublet (quartet)	5.2 (5.2)	-2.0	+0.29
$[\text{Al}_{146}\text{Ru}]-\text{CO}_2$	singlet (singlet)	5.3 (5.2)	-1.5	+0.36
$[\text{Al}_{146}\text{Co}]-\text{CO}_2$	quartet (quartet)	5.1 (5.1)	-1.5	+0.30
$[\text{Al}_{146}\text{Ni}]-\text{CO}_2$	singlet (singlet)	5.3 (5.2)	-1.3	+0.35
$[\text{Al}_{146}\text{Cu}]-\text{CO}_2$	doublet (doublet)	5.2 (5.2)	-0.1	+0.02

Table 3.12: Electronic ground-state data of $[\text{Al}_{146}M]$ with adsorbed CO_2 , values for the isolated clusters are written in brackets. Results include the spin multiplicity, ionization energy, adsorption energy and the ground-state electron transfer (GS CT) into CO_2 (evaluated by Hirshfeld’s scheme as implemented in FHI-aims).

Table 3.12 displays the most favourable spin-state, the first ionization energy, the adsorption energy and the ground-state CT for the $[\text{Al}_{146}M]-\text{CO}_2$ systems. Again, results for the isolated clusters are displayed in brackets. All systems except for the Co-doped cluster have a low-spin ground-state. In the case of the isolated clusters, all systems except for $[\text{Al}_{146}\text{Mn}]$ and $[\text{Al}_{146}\text{Co}]$ are most favourable in their lowest possible spin-multiplicity. Ionization energies range from 5.1 eV ($[\text{Al}_{146}\text{Co}]-\text{CO}_2$ and $[\text{Al}_{146}\text{Co}]$) to 5.3 eV in $[\text{Al}_{146}\text{Ru}]-\text{CO}_2$ and $[\text{Al}_{146}\text{Ni}]-\text{CO}_2$. The ionization energies of the isolated clusters is 5.2 eV except for $[\text{Al}_{146}\text{Co}]$ where it is 5.1 eV. Here it is worth noting that the Co-doped cluster is the only system that has a high-spin configuration in its adsorbed form. Adsorption energies range from -0.1 eV ($[\text{Al}_{146}\text{Cu}]-\text{CO}_2$) to -2.0 eV ($[\text{Al}_{146}\text{Mn}]-\text{CO}_2$). The small adsorption energy of the Cu-doped system can be explained by its large adsorption distance (3.7 Å) but interestingly, the Mn-doped system does not have the smallest adsorption distance but exhibits the highest adsorption energy. Indeed, the smallest adsorption distance which is observed in the Ni-doped cluster only leads to a moderate

adsorption energy, indicating that interactions between the cluster and the molecule are weaker than in the other systems. Significant ground-state charge-transfer again is observed in all systems with adsorption distances below 2.3 Å.

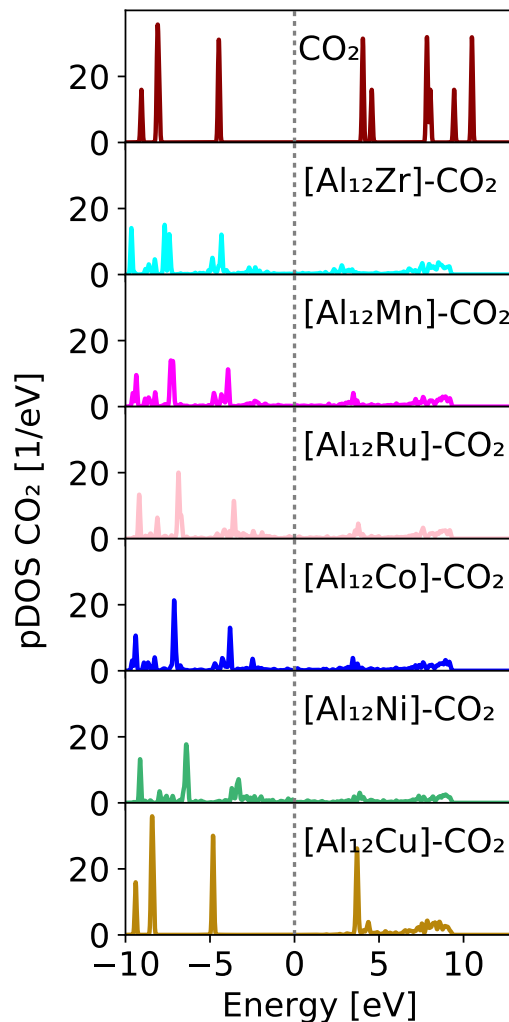


Figure 3.21: DOS projected onto s-, p-, d-, f- and g-character atomic orbitals of CO_2 for the $[Al_{146}M]-CO_2$ systems. The energy scale is shifted by the system's respective Fermi-level which is denoted by a grey vertical line. For better comparison, the DOS of isolated carbon dioxide is displayed at the top. A broadening of 0.05 eV has been used in all graphs.

Figure 3.21 displays the DOS projected onto s-, p-, d-, f- and g-character atomic orbitals of CO_2 for the $[Al_{146}M]-CO_2$ systems. The Cu-doped cluster accurately resembles the CO_2 DOS which can be explained by the large adsorption distance of 3.7 Å which results in very weak interactions between cluster and molecule (also see adsorption energy, Table 3.12). For all other systems, small additional peaks below the Fermi energy can be seen. Differences between the respective pDOSs of all systems except for the Cu-doped cluster are very small which can be explained by the similar geometries (all $[Al_{146}M]-CO_2$ systems exhibit almost perfect icosahedral geometry).

M	El. conf.	Partial charge	s	p	d	Dopant spin
Zr	[Kr]4d ² 5s ²	+0.3 (+0.3)	8.4 (8.6)	18.4 (18.2)	12.7 (12.9)	0 (0)
Mn	[Ar]3d ⁵ 4s ²	-0.1 (0)	6.7 (6.7)	12.4 (12.3)	6.1 (6.0)	1.0 (2.3)
Ru	[Kr]4d ⁷ 5s ¹	-0.2 (-0.2)	8.5 (8.6)	18.6 (18.5)	17.0 (17.1)	0 (0)
Co	[Ar]3d ⁷ 4s ²	-0.3 (-0.2)	6.8 (6.8)	12.6 (12.4)	8.0 (8.0)	0.1 (0.4)
Ni	[Ar]3d ⁸ 4s ²	-0.3 (-0.2)	6.9 (6.9)	12.6 (12.5)	8.8 (8.9)	0 (0)
Cu	[Ar]3d ¹⁰ 4s ¹	-0.2 (-0.2)	6.9 (6.9)	12.7 (12.7)	9.7 (9.7)	0 (0)

Table 3.13: Angular momentum-resolved Mulliken charges of the dopant atoms in $[\text{Al}_{146}M]-\text{CO}_2$. Results were obtained with FHI-aims, values for the isolated clusters are displayed in brackets. "El. conf." denotes the electron configuration of the isolated dopant atom and "s", "p" and "d" denote the amount of electrons of the respective character.

Table 3.13 displays the results of the Mulliken analysis for $[\text{Al}_{146}M]-\text{CO}_2$ and $[\text{Al}_{146}M]$. Dopant charges range from -0.3 in $[\text{Al}_{146}\text{Co}]-\text{CO}_2$ and $[\text{Al}_{146}\text{Ni}]-\text{CO}_2$ to +0.3 in $[\text{Al}_{146}\text{Zr}]-\text{CO}_2$ and $[\text{Al}_{146}\text{Zr}]$. The amount of d-electrons in all systems equals roughly the position in the d-period plus one. In terms of dopant spin it can be noticed that in all adsorbed systems and clusters except for those containing Mn the spin located on the dopant is close to zero, even if the structure has a spin-state that is not a singlet. In the case of $[\text{Al}_{146}\text{Mn}]-\text{CO}_2$, the overall spin-state is a doublet and the system's entire spin is located on the dopant and for $[\text{Al}_{146}\text{Mn}]$ which is a quartet most of the spin is located on Mn.

3.4.2 Comparison of the results to $[\text{Al}_{12}M]-\text{CO}_2$ and $[\text{Al}_{54}M]-\text{CO}_2$

In this section we will discuss how the static properties are affected by cluster size. Therefore we compare all of our results to those obtained previously for the $[\text{Al}_{12}M]-\text{CO}_2$ and $[\text{Al}_{54}M]-\text{CO}_2$ systems (see sections 3.2 and 3.3). We will discuss whether there are general concepts that can be applied to all of the studied aluminium clusters and possibly even transferred to bigger systems than the ones we investigated in this work.

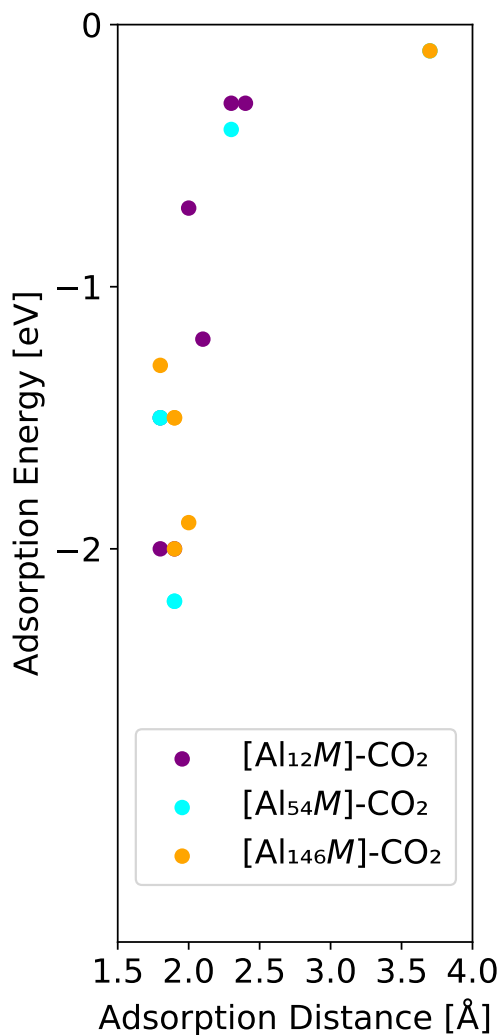


Figure 3.22: Adsorption energy plotted against the respective adsorption distance. The results for $[Al_{12}M]-CO_2$ are displayed in purple, $[Al_{54}M]-CO_2$ is indicated in turquoise and $[Al_{146}M]-CO_2$ is colour-coded in orange.

For the largest clusters, high-spin ground-states can be observed again. It is worth noting that those appear for Co- and Mn-doped clusters just like in the smallest systems. Nevertheless, for $[Al_{146}Co]-CO_2$ unlike for $[Al_{12}Co]-CO_2$, a high-spin ground-state is observed. Since we were not able to obtain a converged geometry for $[Al_{146}Fe]-CO_2$, we cannot evaluate whether this system has a high-spin configuration as its ground-state just like $[Al_{12}Fe]-CO_2$. The trend of the vertical ionization potentials approaching one another with increasing size continues for the largest clusters in our study. This becomes most obvious when looking at the ionization energies of the isolated clusters which are almost all the same. The general red-shift of all ionization energies continues but is less pronounced since it is slowly approaching the classical regime (for comparison: work function of a poly-crystalline Al film on quartz = 4.28 eV[98]) with increasing cluster-size and with each added cluster shell, the overall change in atom number to the previous cluster size becomes smaller.

Figure 3.22 displays the adsorption energies plotted against the corresponding adsorption distance. It can be seen that, with increasing adsorption distance, the adsorption

3 Results and Discussion

energy approaches 0 eV. This behaviour is expected since interactions between CO_2 and the cluster should get weaker with larger distance. This trend does not seem to be linear but appears to be asymptotic which can be explained by the decay of the density which should follow $\frac{1}{r}$. Since we are using a local functional in our simulations, this is not exactly true, but the decay of the density still has an asymptotic behaviour since it decays exponentially. All systems, $[\text{Al}_{12}M]-\text{CO}_2$ (purple dots), $[\text{Al}_{54}M]-\text{CO}_2$ (turquoise dots) and $[\text{Al}_{146}M]-\text{CO}_2$ (orange dots), seem to follow this trend. However, it appears that at similar adsorption distance the largest clusters result in stronger adsorption. Due to the few results it is difficult to tell though if this is really a significant trend or appears due to the small number of systems studied.

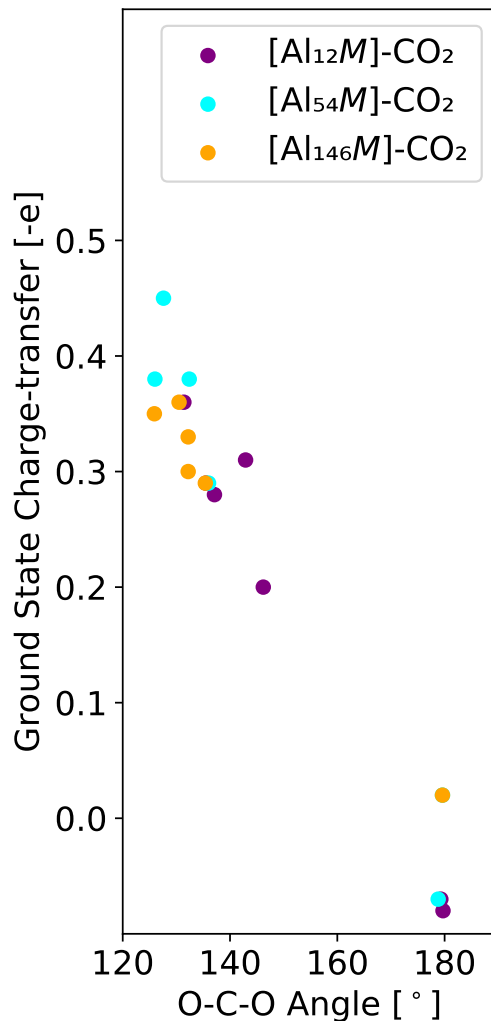


Figure 3.23: Ground-state charge-transfer plotted against the respective adsorption angle. The results for $[\text{Al}_{12}M]-\text{CO}_2$ are displayed in purple, $[\text{Al}_{54}M]-\text{CO}_2$ is indicated in turquoise and $[\text{Al}_{146}M]-\text{CO}_2$ is colour-coded in orange.

Ground-state CT for $[\text{Al}_{146}M]-\text{CO}_2$ is on a comparable scale to that of the smaller clusters. When comparing the pDOS-plots for the different cluster-sizes it is important to note that the peaks appearing well above the Fermi level for the $[\text{Al}_{146}M]-\text{CO}_2$ systems are

a results of the bigger atomic orbital basis onto which the DOS was projected due to the use of a different code and should hence not be taken into account. The remaining peaks are very similar to the smaller clusters as a result of the comparable adsorption geometry. Comparison of the Mulliken analysis to the smaller clusters exhibits the same rule previously observed in terms of electron configuration: There is always one d-electron more than the position of the element in the d-period. Dopant charges only show marginal differences to those computed for the medium-sized clusters. The observation that, unless a cluster or system is a singlet, the spin moment of the dopant equals the total spin moment minus one could be observed throughout all sizes with very few exceptions. Finally, we compare the ground-state CT of all systems with the O-C-O angle of the CO_2 molecule in its adsorbed geometry. The results are displayed in figure 3.23. Again, values of the $[Al_{12}M]-CO_2$ systems are indicated by purple dots while turquoise and orange stand for the medium- and large-sized systems, respectively. It can be seen that there is no notable differences in terms of system size. However, there seems to be a clear connection between the O-C-O angle and the transferred charge. For smaller angles, the amount of electrons located on CO_2 is increased by 0.2 to 0.45 depending on the system and angle. On the other hand, systems with linear CO_2 molecules show values of charge-transfer that are close to zero.

3.4.3 Summary

The trends observed in the small and medium clusters also appear to be valid for the large systems. Ionization energies only show a small reduction in comparison to the medium-sized clusters and differences in terms of these quantities in between different dopants become much smaller with increasing system size. The DOS projected onto an atomic orbital basis is mainly unaffected by the cluster-size as long as the local environment does not change in a major way like in the case of $[Al_{54}NiO]-CO$ (see section 3.3). Adsorption energies vary over different cluster sizes and no clear trend with respect to the dopant can be observed. However, adsorption energy is governed by the adsorption distance of CO_2 . For the large clusters, electrons are transferred at ground-state level for all systems except for the Cu doped cluster. In our study, Cu-doping did not lead to ground-state level CO_2 activation in any case. In terms of spin-multiplicity there is no strong rule that can be derived but it appears that strongly adsorbed geometries are far less likely to have a high-spin electronic ground-state. High-spin ground-states were only observed for systems containing either Mn, Fe or Co. The electron configuration of the dopant-atoms seems to occur according to the same principle as in the small- and medium-sized clusters although $[Al_{146}Mn]-CO_2$ poses the only exception seen across all system sizes.

4 Conclusion and Outlook

We have studied a wide variety of small, atomically defined aluminium clusters with different dopants. We focused on the systems' ability to adsorb and activate CO_2 which is a crucial step in the chemical conversion of carbon dioxide to useful chemicals. We evaluated the relaxed structures with respect to the CO_2 -cluster adsorption distance and O-C-O angle as an indicator of CO_2 activation. We found that adsorption distances for the neutral and negative $[\text{Al}_{13}]$ clusters without dopants were among the largest distances of any system from our study with 3.6 Å. Only the medium-sized and large Cu-doped clusters exhibited a slightly larger adsorption distance with 3.7 Å. This shows that introducing dopants into these Al systems can lead to dramatically improved CO_2 adsorption. Only for some transition-metal dopants, adsorption distances below 2.3 Å could be observed which all resulted in O-C-O angles significantly smaller than 180°. On the other hand, adsorption distances above 2.3 Å exhibited linear CO_2 geometries without exception and were found in all d-metal-free doped systems. We concluded that there is a critical adsorption distance for CO_2 activation which can only be achieved by transition-metal dopants. We found results to be highly sensitive to spin, charge, dopant and cluster size. For the negatively charged small clusters, we found Zr, Ru, Co, Ni, and Ti as dopants to result in activation. For the small neutral clusters, Zr, Mn, Ru, Co and Ni led to bent O-C-O angles. For the neutral medium-sized and large clusters, the dopants that resulted in CO_2 activation for the neutral $[\text{Al}_{12}M]-\text{CO}_2$ systems also exhibited bent O-C-O angles. Only the case of $[\text{Al}_{54}\text{Ni}]-\text{CO}_2$ was special since the CO_2 molecule dissociated on the cluster surface upon adsorption. Overall we found that, independent of charge or size, Zr-, Ru- and Co-doped systems always exhibited CO_2 activation without exception. The largest clusters all exhibited almost perfect icosahedral geometries while smaller clusters often appeared to be distorted icosahedra.

Through a more detailed investigation of the neutral $[\text{Al}_{12}M]-\text{CO}_2$ systems with $M = \text{Zr}, \text{Mn}, \text{Fe}, \text{Ru}, \text{Co}, \text{Ni}$ and Cu , we found that the systems which resulted in CO_2 activation ($M = \text{Zr}, \text{Mn}, \text{Ru}, \text{Co}$ and Ni) were electronically stabilized upon adsorption of CO_2 while the Fe- and Cu-doped clusters seem to be electronically destabilized by the presence of CO_2 . Interestingly, $[\text{Al}_{12}\text{Mn}]$ and $[\text{Al}_{12}\text{Co}]$ change their spin state upon adsorption and transition from a high-spin to a low-spin state. The only system exhibiting a high-spin state in its adsorbed configuration was the Fe-doped cluster. Through different methods of analysing the charge distribution, we were able to show that the bent O-C-O angles indeed are a result of additional charge which is located on the CO_2 molecule. We defined a measure for charge-transfer upon excitation which we called LICT. We were able to show that this is in good agreement with transition-densities obtained from Casida calculations. Systems which resulted in activated CO_2 in the ground-state mostly led to back-transfer

4 Conclusion and Outlook

of the excess charge distributed on carbon dioxide upon excitation while those systems that exhibited linear CO_2 geometries solely transferred charge into the molecule upon excitation. However, $[\text{Al}_{12}\text{Zr}]-\text{CO}_2$, $[\text{Al}_{12}\text{Ni}]-\text{CO}_2$ and $[\text{Al}_{12}\text{Co}]-\text{CO}_2$ did exhibit smaller positive LICT values as well which are associated with the transfer of additional electrons into CO_2 .

The medium-sized clusters exhibited the same trends as the smaller systems, however, there were some minor differences. For example, all $[\text{Al}_{54}M]-\text{CO}_2$ systems exhibited a low-spin configuration as their most favourable state. Ionization energies were red-shifted in comparison to the small clusters and adsorption between cluster and molecule was generally stronger than in the $[\text{Al}_{12}M]-\text{CO}_2$ systems. The onset of LICT is also red-shifted and, in contrast to the small clusters, is located in the visible region of light for the medium-sized clusters. Here it is worth noting though that the exact excitation energies are probably shifted relative to our results due to errors arising from the local XC functional. Again, systems which exhibit ground-state charge-transfer mainly display negative LICT values while systems without significant ground-state charge-transfer tend to have mainly positive LICT values which indicate transfer of electrons from the cluster into the CO_2 molecule. Comparison of the overall LICT of a system to that of its smaller counterpart yields results that are of the same order of magnitude.

For the largest clusters we only studied ground-state properties. The main differences between $[\text{Al}_{146}M]-\text{CO}_2$ and $[\text{Al}_{54}M]-\text{CO}_2$ was the reappearance of high-spin ground-states. In general, trends observed for small and medium-sized clusters largely remained, although adsorption strength was not generally increased but in some cases weakened in comparison to the smaller systems. Ionization energies in $[\text{Al}_{146}M]-\text{CO}_2$ were very similar despite the different dopants which can be explained by the smaller overall fraction of dopant compared to the smaller systems. The C and O projected DOS remained mainly unaffected throughout all cluster sizes unless the local environment of CO_2 underwent a significant change like in the case of $[\text{Al}_{54}\text{Ni}]-\text{CO}_2$. The shorter the adsorption distance, the stronger the adsorption. However, no differences with respect to the different system sizes can be observed within this. The same applies to the connection between ground-state charge-transfer and the O-C-O angle. Although smaller angles correspond to larger amounts of charge-transfer, no clear trend with respect to system size can be observed. All systems with only one exception showed the same electronic dopant structure: The dopant always contained one electron more with d-character and one less with s-character than its position in the periodic table would indicate. High-spin ground-states were only observed for systems that contained either Mn, Fe or Co.

The adsorption geometries obtained throughout all cluster sizes (with few exceptions) can be expected to predominantly yield CO as a product due to the steric hindrance of attacks to the carbon atom which result from the adsorption geometries. However, this CO gas could then be used in e.g. a Fischer-Tropsch synthesis in combination with H_2 to obtain useful products.[97] Our results give further insights into atomically defined aluminium catalysts and point out some interesting findings that could help pave the way for future studies. Future work could focus on the dynamics of the LICT process to compare the different systems with respect to their charge-transfer rates and study if the systems remain stable upon excitation or e.g. CO_2 dissociates throughout the process. It would be interesting to see if larger Zr-, Ru- or Co-doped aluminium clusters could be

synthesised and would exhibit the catalytic potential in experiments which our findings hint at. It would also be of interest to investigate how the systems are affected by oxidation or protecting ligands and if the clusters exhibiting a high-spin ground-state are magnetic and hence could be easily recovered from the reaction batch. In this regard it could also be of interest to study correlation in these systems and see how certain parameters are affected by e.g. different +U corrections. Our results are promising since despite smaller differences between different cluster-sizes, some trends could be extracted and remained mainly unchanged throughout the systems. We think that our systematic study has given valuable insights into new chances for catalyst design and helps to understand the effects of different dopants on aluminium cluster properties in a better way. Although we did not answer all questions, our work is a fundament on which future research can build and hopefully shed more light onto the catalytic processes which govern CO₂ activation.

5 Computational Details

In the following chapter, the details necessary to reproduce the results presented in this thesis are shown. Since this chapter is meant for the reader who wants to quickly find a certain parameter, we present the data (if possible) in the form of tables and listed by calculation type.

5.1 Geometry Optimizations

In this section we focus on the details of the calculations from which the structures of the clusters studied were produced. We will start with the relaxations of the smallest clusters, continue with the details used for the medium-sized and large clusters and finish by describing how the ground-state geometry was found in the pool of structures that was generated.

First, we studied small neutral and singly negatively charged aluminium clusters' geometries in the neighbourhood of CO_2 . Therefore we started from icosahedral $[\text{Al}_{13}]^-$ with a CO_2 molecule placed in the vicinity of the cluster. The molecular axis is perpendicular to the axis formed by the central aluminium atom and the cluster atom that is closest to the CO_2 . The distance between the outer cluster atom and the carbon atom is chosen to be 2.7 \AA which is the same as the distance of the outer shell atoms to the central atoms. This value has been found by Casanova et al.[82] from their relaxations of $[\text{Al}_{13}]^-$ on a PBE0 level which should give us a reasonable starting point. The same initial geometries are created for clusters with dopants. The initial geometry is illustrated in figure 5.1. We exchange the outer aluminium atom that is closest to CO_2 for one of the following atoms: B, C, H, N, O, P, S, Si, Zr, Mn, Fe, Ru, Co, Ni, Cu, Ti, Pd, Rh, Ag or Au. From these initial geometries we performed relaxations for the singly negatively charged systems and their neutral counter parts. We denote these systems by $[\text{Al}_{12}M]-\text{CO}_2$ and $([\text{Al}_{12}M]-\text{CO}_2)^-$ with M being the placeholder for the dopant.

From these starting geometries we relax the atomic positions using both spin-polarized and spin-unpolarized DFT with a PBE exchange-correlation functional[99] and a Grimme-d2 correction[100] to account for van-der-Waals interactions. These calculations are carried out in the Quantum Espresso software package[101] with ultra-soft GBRV PPs[102]. As wave function cut-off and charge density cut-off we used 40 Ry and 200 Ry, respectively,

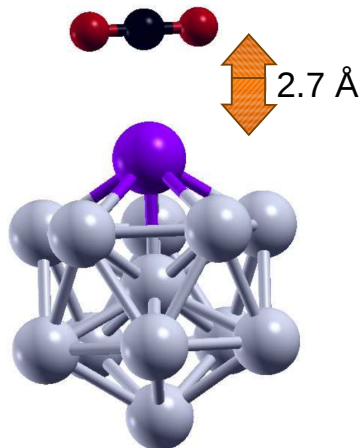


Figure 5.1: Starting geometry for the relaxations. Atom colours: Grey = aluminium, black = carbon, red = oxygen, purple = M .

which are the suggested cut-offs from the original publication of the PPs[102]. The simulation box was cubic with an edge length of 45 \AA . A Gaussian smearing of 0.001 Ry was used and the calculations were considered converged when the forces were smaller than 10^{-3} eV/\AA . From this preselection of clusters the lowest-energy structures were picked and compared with respect to their CO_2 -adsorption distance and O-C-O bond angle. The adsorption distance was defined as the smallest distance between any cluster and any CO_2 atom. From the neutral clusters we selected the seven systems that exhibited the smallest adsorption distances. In particular, we selected the Zr, Mn, Fe, Ru, Co, Ni and Cu doped $[\text{Al}_{12}M]-\text{CO}_2$ systems.

The obtained relaxed structures were then used as initial geometries in a spin-polarized calculation with the same parameters as described previously. We found the results to be highly dependent on the computational settings, like choice of basis, exchange-correlation functional and spin-polarization. In order to test the PP basis, we carried out relaxations starting from the initial geometries as well as the results from the Quantum Espresso calculations using FHI-aims[103, 104]. Here we also used PBE as exchange correlation functional and chose second tier basis functions of numerical localized orbitals to be our basis.

The pool of candidate structures that was obtained through this routine (meaning from the FHI-aims and quantum espresso relaxations) was then used to find the lowest energy structure. Therefore, all results from the Quantum Espresso and FHI-aims relaxations were calculated in the Octopus code[105, 106, 107, 108] in all possible spin states using the local density approximation (LDA) and the implemented norm-conserving Hartwigsen-Goedecker-Hutter PPs[109] (including semi-core states for the transition metal atoms). The total energies were then compared and the lowest energy configuration was chosen. Isolated cluster geometries for the computation of their electronic properties were obtained by relaxations with Quantum Espresso and FHI-aims, starting from the lowest energy configuration of the adsorbed system with removed CO_2 . For the bigger clusters, the starting point was the icosahedral doped cluster and CO_2 was located in the proximity of the dopant. As CO_2 distance and geometry, we chose the one which we found to be the ground-state in the smaller systems. From this starting point a relaxation using FHI-aims

as described above was performed.

5.2 Ground State and Excited State Properties

In the previous section we described how we found the ground-state geometries of the systems. In this section we will focus on the details of the calculations that were then carried out with these structures.

System	Grid (IP) [Å]	Box (IP)[Å]	Grid (AE) [Å]	Box (AE) [Å]	Grid (DOS) [Å]	Box (DOS) [Å]
[Al ₁₂ Zr]–CO ₂	0.18	5	0.06	5	0.16	9
[Al ₁₂ Mn]–CO ₂	0.14	6	0.06	5	0.14	9
[Al ₁₂ Fe]–CO ₂	0.18	5	0.06	5	0.16	9
[Al ₁₂ Ru]–CO ₂	0.20	6	0.06	5	0.18	9
[Al ₁₂ Co]–CO ₂	0.16	5	0.06	5	0.14	9
[Al ₁₂ Ni]–CO ₂	0.12	5	0.06	5	0.14	9
[Al ₁₂ Cu]–CO ₂	0.16	5	0.06	5	0.14	9

Table 5.1: Calculation parameters used for determining the vertical ionization energy ("IP"), adsorption energy and most favourable spin-state ("AE") and computation of DOS, pDOS, ELF, ground-state electron transfer and Casida calculations ("DOS"). "Grid" denotes the spacing of points on the real-space grid while "Box" denotes the radius of the minimum box. In the calculation of the ELF of [Al₁₃]–CO₂, a smearing of 0.1 eV was used to achieve convergence.

Mulliken analysis data was obtained using FHI-aims with a pz-LDA XC-functional, second-tier basis functions and spin-polarized calculations. All other ground state calculations were performed with Octopus on an LDA theory level. The density was converged up to a relative accuracy of 10^{-7} (defined as the inverse electron number of the problem multiplied by the absolute density convergence) and the grid-spacing and box radii of the minimum box shape were converged with respect to the quantity of interest. For the [Al₁₂M]–CO₂ systems we also carried out LDA+U calculations with a Hubbard U of 6 eV. The minimum convergence parameters for ground state properties and Casida calculations that we found to be sufficient and used to produce the results in this thesis can be found in Table 5.1. For Casida spectra of the medium sized clusters, [Al_{5,4}M]–CO₂, we only considered transitions between states that had an energy difference smaller than 10 eV since this should be sufficient for our purposes because ionization energies of these systems range from 5.2 eV to 5.5 eV (see chapter 3.3). To determine the amount of charge for each state that is located on CO₂, we performed a pDOS calculation (projection of the density of states (DOS) onto an atomic orbital basis) for the energy range between -35 eV and 3 eV with a Gaussian smearing of 0.001 eV and an energy grid of 150,000 points within the energy frame using Octopus. We then sum the pDOS over the atoms of CO₂ and multiply

the result with a top-hat function of width 0.001 which is centred around each peak at a time, then we integrate the result over the energy. In order to account for degeneracies and avoid over representation of these states, we divide this result by the integral over the total DOS computed on the same energy grid and multiplied with the same top-hat function. This normalized result is then the basis for our consecutive analysis of the light induced charge-transfer (LICT). Casida calculations were performed with 100 unoccupied spin-down and 100 unoccupied spin-up states.

We also carried out time-dependent density functional theory (TDDFT) calculations in order to obtain excited state properties like adsorption spectra. Therefore we used a Casida formalism as well as time-propagations with ALDA. For the spectra obtained from time-propagations, we chose the time-step sufficiently small to ensure a high level of total-energy conservation over the propagation time of 13.164 fs. The minimal convergence parameters that were used for the time-propagations in this thesis can be found in Table 5.2.

System	Time [1/eV]	Step	Grid [\AA]	Box Radius [\AA]	kick strength [1/ \AA]
[Al ₁₂ Zr]–CO ₂	0.001		0.26	8.0	0.01
[Al ₁₂ Mn]–CO ₂	0.001		0.18	8.0	0.01
[Al ₁₂ Fe]–CO ₂	0.001		0.22	8.0	0.01
[Al ₁₂ Ru]–CO ₂	0.001		0.32	8.0	0.01
[Al ₁₂ Co]–CO ₂	0.001		0.20	9.0	0.01
[Al ₁₂ Ni]–CO ₂	0.001		0.18	8.0	0.01
[Al ₁₂ Cu]–CO ₂	0.001		0.18	13.0	0.01

Table 5.2: Minimal convergence Parameters found for computation of the absorption spectra from time-propagations.

Ground state charge transfer was determined by a Hirshfeld-analysis[73]. Since this is only implemented in Octopus for time-dependent calculations, we performed a time-propagation without any perturbation and one time step and used the result for time=0. For computational feasibility reasons, the biggest clusters were calculated using FHI-aims with a pz-LDA XC-functional, second-tier basis functions and spin-polarized calculations. Ground-state charge-transfer again was determined by a Hirshfeld analysis (as implemented in FHI-aims).

Bibliography

- [1] S. Solomon, G.-K. Plattner, R. Knutti, and P. Friedlingstein. Irreversible climate change due to carbon dioxide emissions. *Proceedings of the national academy of sciences*, 106(6):1704–1709, 2009.
- [2] R. Schmalensee, T. M. Stoker, and R. A. Judson. World carbon dioxide emissions: 1950–2050. *Review of Economics and Statistics*, 80(1):15–27, 1998.
- [3] R. Smale, M. Hartley, C. Hepburn, J. Ward, and M. Grubb. The impact of CO₂ emissions trading on firm profits and market prices. *Climate Policy*, 6(1):31–48, 2006.
- [4] A. Álvarez, M. Borges, J. J. Corral-Pérez, J. G. Olcina, L. Hu, D. Cornu, R. Huang, D. Stoian, and A. Urakawa. CO₂ activation over catalytic surfaces. *ChemPhysChem*, 18(22):3135–3141, 2017.
- [5] X. Chang, T. Wang, and J. Gong. CO₂ photo-reduction: insights into CO₂ activation and reaction on surfaces of photocatalysts. *Energy & Environmental Science*, 9(7):2177–2196, 2016.
- [6] S. Remiro-Buenamañana and H. García. Photoassisted CO₂ conversion to fuels. *ChemCatChem*, 11(1):342–356, 2019.
- [7] U. Rodemerck, M. Holeña, E. Wagner, Q. Smejkal, A. Barkschat, and M. Baerns. Catalyst development for CO₂ hydrogenation to fuels. *ChemCatChem*, 5(7):1948–1955, 2013.
- [8] B. Kumar, M. Llorente, J. Froehlich, T. Dang, A. Sathrum, and C. P. Kubiak. Photochemical and photoelectrochemical reduction of CO₂. *Annual review of physical chemistry*, 63:541–569, 2012.
- [9] H. Puliyalil, D. L. Jurković, V. D. B. C. Dasireddy, and B. Likozar. A review of plasma-assisted catalytic conversion of gaseous carbon dioxide and methane into value-added platform chemicals and fuels. *RSC advances*, 8(48):27481–27508, 2018.
- [10] F. Hussin and M. K. Aroua. Recent development in the electrochemical conversion of carbon dioxide: Short review. In *AIP Conference Proceedings*, volume 2124, page 030017. AIP Publishing LLC, 2019.
- [11] E. T. Kho, T. H. Tan, E. Lovell, R. J. Wong, J. Scott, and R. Amal. A review on

- photo-thermal catalytic conversion of carbon dioxide. *Green Energy & Environment*, 2(3):204–217, 2017.
- [12] M. E. Dry. High quality diesel via the Fischer-Tropsch process—a review. *Journal of Chemical Technology & Biotechnology: International Research in Process, Environmental & Clean Technology*, 77(1):43–50, 2002.
- [13] N. Podrojková, V. Sans, A. Oriňak, and R. Oriňaková. Recent developments in the modelling of heterogeneous catalysts for CO₂ conversion to chemicals. *Chem-CatChem*, 12(7):1802–1825, 2020.
- [14] C.-H. Huang, C.-S. Tan, and et al. A review: CO₂ utilization. *Aerosol and Air Quality Research*, 14(2):480–499, 2014.
- [15] J. Albero, E. Dominguez, A. Corma, and H. García. Continuous flow photoassisted CO₂ methanation. *Sustainable Energy & Fuels*, 1(6):1303–1307, 2017.
- [16] W. A. Herrmann and B. Cornils. Organometallic Homogeneous Catalysis—Quo vadis? *Angewandte Chemie International Edition in English*, 36(10):1048–1067, 1997.
- [17] W. Wang, S. Wang, X. Ma, and J. Gong. Recent advances in catalytic hydrogenation of carbon dioxide. *Chemical Society Reviews*, 40(7):3703–3727, 2011.
- [18] P. W. N. M. Van Leeuwen. *Homogeneous catalysis: understanding the art*. Springer Science & Business Media, 2006.
- [19] D. J. Cole-Hamilton. Homogeneous catalysis—new approaches to catalyst separation, recovery, and recycling. *Science*, 299(5613):1702–1706, 2003.
- [20] C. Costentin, G. Passard, M. Robert, and J.-M. Savéant. Ultraefficient homogeneous catalyst for the CO₂ to CO electrochemical conversion. *Proceedings of the National Academy of Sciences*, 111(42):14990–14994, 2014.
- [21] E. Graf and W. Leitner. Direct formation of formic acid from carbon dioxide and dihydrogen using the [Rh (cod) Cl]₂–Ph₂P (CH₂)₄PPh₂ catalyst system. *Journal of the Chemical Society, Chemical Communications*, (8):623–624, 1992.
- [22] J. Kothandaraman, A. Goepfert, M. Czaun, G. A. Olah, and G. K. S. Prakash. Conversion of CO₂ from air into methanol using a polyamine and a homogeneous ruthenium catalyst. *Journal of the American Chemical Society*, 138(3):778–781, 2016.
- [23] T. Ouyang, C. Hou, J.-W. Wang, W.-J. Liu, D.-C. Zhong, Z.-F. Ke, and T.-B. Lu. A highly selective and robust Co (II)-based homogeneous catalyst for reduction of CO₂ to CO in CH₃CN/H₂O solution driven by visible light. *Inorganic chemistry*, 56(13):7307–7311, 2017.

Bibliography

- [24] J. M. Thomas and W. J. Thomas. *Principles and practice of heterogeneous catalysis*. John Wiley & Sons, 2014.
- [25] P. S. S. Prasad, J. W. Bae, K.-W. Jun, and K.-W. Lee. Fischer-Tropsch synthesis by carbon dioxide hydrogenation on Fe-based catalysts. *Catalysis surveys from Asia*, 12(3):170–183, 2008.
- [26] J. Nakamura, Y. Choi, and T. Fujitani. On the issue of the active site and the role of ZnO in Cu/ZnO methanol synthesis catalysts. *Topics in catalysis*, 22(3):277–285, 2003.
- [27] F.-W. Chang, T.-J. Hsiao, and J.-D. Shih. Hydrogenation of CO₂ over a rice husk ash supported nickel catalyst prepared by deposition-precipitation. *Industrial & engineering chemistry research*, 37(10):3838–3845, 1998.
- [28] Y. Du, H. Sheng, D. Astruc, and M. Zhu. Atomically precise noble metal nanoclusters as efficient catalysts: a bridge between structure and properties. *Chemical reviews*, 120(2):526–622, 2019.
- [29] Q. Tang, Y. Lee, D.-Y. Li, W. Choi, C. W. Liu, D. Lee, and D.-E. Jiang. Lattice-hydride mechanism in electrocatalytic CO₂ reduction by structurally precise copper-hydride nanoclusters. *Journal of the American Chemical Society*, 139(28):9728–9736, 2017.
- [30] G. Li and R. Jin. Atomically precise gold nanoclusters as new model catalysts. *Accounts of chemical research*, 46(8):1749–1758, 2013.
- [31] D. R. Kauffman, D. Alfonso, C. Matranga, P. Ohodnicki, X. Deng, R. C. Siva, C. Zeng, and R. Jin. Probing active site chemistry with differently charged Au₂₅^q nanoclusters (q = -1, 0, +1). *Chemical Science*, 5(8):3151–3157, 2014.
- [32] W. Fei, S. Antonello, T. Dainese, A. Dolmella, M. Lahtinen, K. Rissanen, A. Venzo, and F. Maran. Metal Doping of Au₂₅(SR)₁₈⁻-Clusters: Insights and Hindsight. *Journal of the American Chemical Society*, 141(40):16033–16045, 2019.
- [33] A. Moscatelli. Plasmonics: the aluminium rush. *Nature nanotechnology*, 7(12):778, 2012.
- [34] M. W. Knight, N. S. King, L. Liu, H. O. Everitt, P. Nordlander, and N. J. Halas. Aluminum for plasmonics. *ACS nano*, 8(1):834–840, 2014.
- [35] C. Clavero. Plasmon-induced hot-electron generation at nanoparticle/metal-oxide interfaces for photovoltaic and photocatalytic devices. *Nature Photonics*, 8(2):95–103, 2014.
- [36] J. A. González, V. Lopez, A. Bautista, E. Otero, and X. R. Nóvoa. Characterization of porous aluminium oxide films from ac impedance measurements. *Journal of applied Electrochemistry*, 29(2):229–238, 1999.

- [37] H. Robotjazi, H. Zhao, D. F. Swearer, N. J. Hogan, L. Zhou, A. Alabastri, M. J. McClain, P. Nordlander, and N. J. Halas. Plasmon-induced selective carbon dioxide conversion on earth-abundant aluminum-cuprous oxide antenna-reactor nanoparticles. *Nature communications*, 8(1):1–10, 2017.
- [38] D. F. Swearer, R. K. Leary, R. Newell, S. Yazdi, H. Robotjazi, Y. Zhang, D. Renard, P. Nordlander, P. A. Midgley, and N. J. Halas. Transition-metal decorated aluminum nanocrystals. *ACS nano*, 11(10):10281–10288, 2017.
- [39] J.-Y. Zhao, Y. Zhang, F.-Q. Zhao, and X.-H. Ju. Adsorption of Carbon Dioxide on Al_{12}X Clusters Studied by Density Functional Theory: Effect of Charge and Doping. *The Journal of Physical Chemistry A*, 117(47):12519–12528, 2013.
- [40] J.-Y. Zhao, F.-Q. Zhao, S.-Y. Xu, and X.-H. Ju. Theoretical study of the geometries and decomposition energies of CO_2 on Al_{12}X : Doping effect of Al_{12}X . *Journal of Molecular Graphics and Modelling*, 48:9–17, 2014.
- [41] W. Kohn. Nobel Lecture: Electronic structure of matter—wave functions and density functionals. *Reviews of Modern Physics*, 71(5):1253, 1999.
- [42] C. Fiolhais, F. Nogueira, and M. Marques. *A Primer in Density Functional Theory*. Springer-Verlag, 2003.
- [43] P. Giannozzi. *Density Functional Theory for Electronic Structure Calculations*. Universita di Pisa, 2002.
- [44] W. Koch and M. C. Holthausen. *A Chemist’s guide to Density Functional Theory*. Wiley-VCH Verlag GmbH, 2001.
- [45] P. E. Blöchl. *Theory and Practice of Dneisty-Functional Theory*. Institute for Theoretical Physics, Clausthal University of Technology, 2011.
- [46] E. J. Baerends and O. V. Gritsenko. A quantum chemical view of density functional theory. *The Journal of Physical Chemistry A*, 101(30):5383–5403, 1997.
- [47] R. Stowasser and R. Hoffmann. What do the Kohn-Sham orbitals and eigenvalues mean? *Journal of the american chemical society*, 121(14):3414–3420, 1999.
- [48] R. M. Martin. *Electronic Structure: Basic Theory and Practical Methods*. Cambridge University, Cambridge, 2004.
- [49] A. T. Hagler. Force field development phase II: Relaxation of physics-based criteria... or inclusion of more rigorous physics into the representation of molecular energetics. *Journal of computer-aided molecular design*, 33(2):205–264, 2019.
- [50] R. P. Feynman. Forces in molecules. *Physical review*, 56(4):340, 1939.
- [51] W. L. Price. Global optimization by controlled random search. *Journal of Opti-*

Bibliography

- mization Theory and Applications*, 40(3):333–348, 1983.
- [52] M. D. Intriligator. *Mathematical optimization and economic theory*. SIAM, 2002.
- [53] A. M. Bagirov and A. M. Rubinov. Global optimization of marginal functions with applications to economic equilibrium. *Journal of Global Optimization*, 20(3):215–237, 2001.
- [54] A. Törn and A. Zilinskas. *Global optimization*. Springer, 1989.
- [55] R. Horst and P. M. Pardalos. *Handbook of global optimization*, volume 2. Springer Science & Business Media, 2013.
- [56] P. M. Pardalos and J. B. Rosen. *Constrained global optimization: algorithms and applications*. Springer, 1987.
- [57] J. P. Perdew and A. Zunger. Self-interaction correction to density-functional approximations for many-electron systems. *Physical Review B*, 23(10):5048, 1981.
- [58] J. Guan, P. Duffy, J. T. Carter, D. P. Chong, K. C. Casida, M. E. Casida, and M. Wrinn. Comparison of local-density and Hartree–Fock calculations of molecular polarizabilities and hyperpolarizabilities. *The Journal of chemical physics*, 98(6):4753–4765, 1993.
- [59] A. J. Cohen, P. Mori-Sánchez, and W. Yang. Insights into current limitations of density functional theory. *Science*, 321(5890):792–794, 2008.
- [60] D. Koller, P. Blaha, and F. Tran. Hybrid functionals for solids with an optimized Hartree–Fock mixing parameter. *Journal of Physics: Condensed Matter*, 25(43):435503, 2013.
- [61] V. I. Anisimov, J. Zaanen, and O. K. Andersen. Band theory and Mott insulators: Hubbard U instead of Stoner I. *Physical Review B*, 44(3):943, 1991.
- [62] S. Goedecker and C. J. Umrigar. Critical assessment of the self-interaction-corrected–local-density-functional method and its algorithmic implementation. *Physical Review A*, 55(3):1765, 1997.
- [63] E. Pavarini, E. Koch, F. Anders, and M. Jarrell. *Correlated Electrons: From Models to Materials (Modeling and Simulation Vol. 2)*. Forschungszentrum Jülich, 2012.
- [64] H. Rydberg, M. Dion, N. Jacobson, E. Schröder, P. Hyldgaard, S. I. Simak, D. C. Langreth, and B. I. Lundqvist. Van der Waals density functional for layered structures. *Physical review letters*, 91(12):126402, 2003.
- [65] E. R. Johnson, I. D. Mackie, and G. A. DiLabio. Dispersion interactions in density-functional theory. *Journal of Physical Organic Chemistry*, 22(12):1127–1135, 2009.
- [66] S. Grimme. Density functional theory with London dispersion corrections. *Wiley*

- Interdisciplinary Reviews: Computational Molecular Science*, 1(2):211–228, 2011.
- [67] S. Grimme. Semiempirical GGA-type density functional constructed with a long-range dispersion correction. *Journal of computational chemistry*, 27(15):1787–1799, 2006.
- [68] J. F. Janak. A limitation on the pseudopotential method. *Solid State Communications*, 20(2):151–153, 1976.
- [69] U. Von Barth and C. D. Gelatt. Validity of the frozen-core approximation and pseudopotential theory for cohesive energy calculations. *Physical Review B*, 21(6):2222, 1980.
- [70] D. Jacquemin, T. Le Bahers, C. Adamo, and I. Ciofini. What is the “best” atomic charge model to describe through-space charge-transfer excitations? *Physical Chemistry Chemical Physics*, 14(16):5383–5388, 2012.
- [71] C. Fonseca Guerra, J.-W. Handgraaf, E. J. Baerends, and F. M. Bickelhaupt. Voronoi deformation density (VDD) charges: Assessment of the Mulliken, Bader, Hirshfeld, Weinhold, and VDD methods for charge analysis. *Journal of computational chemistry*, 25(2):189–210, 2004.
- [72] R. S. Mulliken. Electronic population analysis on LCAO–MO molecular wave functions. I. *The Journal of Chemical Physics*, 23(10):1833–1840, 1955.
- [73] F. L. Hirshfeld. Bonded-atom fragments for describing molecular charge densities. *Theoretica chimica acta*, 44:129, 1977.
- [74] R. F. W. Bader, P. M. Beddall, and P. E. Cade. Partitioning and characterization of molecular charge distributions. *Journal of the American Chemical Society*, 93(13):3095–3107, 1971.
- [75] C. A. Guido, P. Cortona, B. Mennucci, and C. Adamo. On the metric of charge transfer molecular excitations: a simple chemical descriptor. *Journal of chemical theory and computation*, 9(7):3118–3126, 2013.
- [76] F. Giustino. *Materials Modelling using Density Functional Theory*. Oxford University Press, 2014.
- [77] M. E. Casida. Time-dependent density functional response theory for molecules. In *Recent Advances In Density Functional Methods: (Part I)*, pages 155–192. World Scientific, 1995.
- [78] W. G. Schmidt. *Quantum Chemistry*. Universität Paderborn, 2016.
- [79] H. Appel, E. K. U. Gross, and K. Burke. Excitations in time-dependent density-functional theory. *Physical review letters*, 90(4):043005, 2003.

Bibliography

- [80] M. Rohlfing and S. G. Louie. Electron-hole excitations and optical spectra from first principles. *Physical Review B*, 62(8):4927, 2000.
- [81] M. L. Tiago and J. R. Chelikowsky. First-principles GW–BSE excitations in organic molecules. *Solid state communications*, 136(6):333–337, 2005.
- [82] D. Casanova, J. M. Matxain, and J. M. Ugalde. Plasmonic resonances in the Al_{13}^- -cluster: Quantification and origin of exciton collectivity. *The Journal of Physical Chemistry C*, 120(23):12742–12750, 2016.
- [83] Z. Lin, T. Slee, and D. M. P. Mingos. A structural jellium model of cluster electronic structure. *Chemical physics*, 142(2):321–334, 1990.
- [84] A. B. Vidal, L. Feria, J. Evans, Y. Takahashi, P. Liu, K. Nakamura, F. Illas, and J. A. Rodriguez. CO_2 activation and methanol synthesis on novel Au/TiC and Cu/TiC catalysts. *The journal of physical chemistry letters*, 3(16):2275–2280, 2012.
- [85] M.-M. Millet, G. Algara-Siller, S. Wrabetz, A. Mazheika, F. Girgsdies, D. Teschner, F. Seitz, A. Tarasov, S. V. Levchenko, R. Schloegl, and et al. Ni single atom catalysts for CO_2 activation. *Journal of the American Chemical Society*, 141(6):2451–2461, 2019.
- [86] J. P. Krogman, B. M. Foxman, and C. M. Thomas. Activation of CO_2 by a heterobimetallic Zr/Co complex. *Journal of the American Chemical Society*, 133(37):14582–14585, 2011.
- [87] S. F. Li and X. G. Gong. Neutral and negatively charged Al_{12}X (X= Si, Ge, Sn, Pb) clusters studied from first principles. *Physical Review B*, 74(4):045432, 2006.
- [88] R. R. Zope and T. Baruah. Conformers of Al_{13} , Al_{12}M , and Al_{13}M (M= Cu, Ag, and Au) clusters and their energetics. *Physical Review A*, 64(5):053202, 2001.
- [89] R. Ahlrichs and S. D. Elliott. Clusters of aluminium, a density functional study. *Physical Chemistry Chemical Physics*, 1(1):13–21, 1999.
- [90] M. W. Knight, N. S. King, L. Liu, H. O. Everitt, P. Nordlander, and N. J. Halas. Aluminum for plasmonics. *ACS nano*, 8(1):834–840, 2014.
- [91] M. I. Lerner, E. A. Glazkova, A. S. Lozhkomoiev, N. V. Svarovskaya, O. V. Bakina, A. V. Pervikov, and S. G. Psakhie. Synthesis of Al nanoparticles and Al/AlN composite nanoparticles by electrical explosion of aluminum wires in argon and nitrogen. *Powder Technology*, 295:307–314, 2016.
- [92] E. König. The nephelauxetic effect calculation and accuracy of the interelectronic repulsion parameters I. Cubic high-spin d 2, d 3, d 7, and d 8 systems. In *The nephelauxetic effect calculation and accuracy of the interelectronic repulsion parameters (I. Cubic high-spin d 2, d 3, d 7, and d 8 systems) in "Structure and Bonding"*, pages 175–212. Springer, 1971.

- [93] A. Goebel, A. Rubio, and J. Lischner. Light-Induced Charge Transfer from Transition-Metal-Doped Aluminum Clusters to Carbon Dioxide.
- [94] A. Savin, R. Nesper, S. Wengert, and T. F. Fässler. ELF: The electron localization function. *Angewandte Chemie International Edition in English*, 36(17):1808–1832, 1997.
- [95] C. Kim, S. Hyeon, J. Lee, W. D. Kim, D. C. Lee, J. Kim, and H. Lee. Energy-efficient CO₂ hydrogenation with fast response using photoexcitation of CO₂ adsorbed on metal catalysts. *Nature communications*, 9(1):1–8, 2018.
- [96] X. Chang, T. Wang, and J. Gong. CO₂ photo-reduction: insights into CO₂ activation and reaction on surfaces of photocatalysts. *Energy & Environmental Science*, 9(7):2177–2196, 2016.
- [97] H. Schulz. Short history and present trends of Fischer-Tropsch synthesis. *Applied Catalysis A: General*, 186(1-2):3–12, 1999.
- [98] R. M. Eastment and C. H. B. Mee. Work function measurements on (100),(110) and (111) surfaces of aluminium. *Journal of Physics F: Metal Physics*, 3(9):1738, 1973.
- [99] J. P. Perdew, K. Burke, and M. Ernzerhof. Generalized gradient approximation made simple. *Physical review letters*, 77(18):3865, 1996.
- [100] S. Grimme, J. Antony, S. Ehrlich, and H. Krieg. A consistent and accurate ab initio parametrization of density functional dispersion correction (DFT-D) for the 94 elements H-Pu. *The Journal of chemical physics*, 132(15):154104, 2010.
- [101] P. Giannozzi, S. Baroni, N. Bonini, M. Calandra, R. Car, C. Cavazzoni, D. Ceresoli, G. L. Chiarotti, M. Cococcioni, I. Dabo, and et al. QUANTUM ESPRESSO: a modular and open-source software project for quantum simulations of materials. *Journal of physics: Condensed matter*, 21(39):395502, 2009.
- [102] K. F. Garrity, J. W. Bennett, K. M. Rabe, and D. Vanderbilt. Pseudopotentials for high-throughput DFT calculations. *Computational Materials Science*, 81:446–452, 2014.
- [103] V. Blum, R. Gehrke, F. Hanke, P. Havu, V. Havu, X. Ren, K. Reuter, and M. Scheffler. Ab initio molecular simulations with numeric atom-centered orbitals. *Computer Physics Communications*, 180(11):2175–2196, 2009.
- [104] V. Havu, V. Blum, P. Havu, and M. Scheffler. Efficient O (N) integration for all-electron electronic structure calculation using numeric basis functions. *Journal of Computational Physics*, 228(22):8367–8379, 2009.
- [105] A. Castro, H. Appel, M. Oliveira, C. A. Rozzi, X. Andrade, F. Lorenzen, M. A. L. Marques, E. K. U. Gross, and A. Rubio. Octopus: a tool for the application of time-

Bibliography

- dependent density functional theory. *physica status solidi (b)*, 243(11):2465–2488, 2006.
- [106] X. Andrade, D. Strubbe, U. De Giovannini, A. H. Larsen, M. J. T. Oliveira, J. Alberdi-Rodriguez, A. Varas, I. Theophilou, N. Helbig, M. J. Verstraete, and et al. Real-space grids and the Octopus code as tools for the development of new simulation approaches for electronic systems. *Physical Chemistry Chemical Physics*, 17(47):31371–31396, 2015.
- [107] N. Tancogne-Dejean, M. J. T. Oliveira, X. Andrade, H. Appel, C. H. Borca, G. Le Breton, F. Buchholz, A. Castro, S. Corni, A. A. Correa, and et al. Octopus, a computational framework for exploring light-driven phenomena and quantum dynamics in extended and finite systems. *The Journal of Chemical Physics*, 152(12):124119, 2020.
- [108] N. Tancogne-Dejean, M. J. T. Oliveira, and A. Rubio. Self-consistent DFT+ U method for real-space time-dependent density functional theory calculations. *Physical Review B*, 96(24):245133, 2017.
- [109] C. Hartwigsen, S. Goedecker, and J. Hutter. Relativistic separable dual-space Gaussian pseudopotentials from H to Rn. *Physical Review B*, 58(7):3641, 1998.

List of Hazardous Chemicals

No hazardous chemicals according to the Globally Harmonized System of Classification and Labelling of Chemicals (GHS) have been used in the course of this work.

Acknowledgements

The following pages are dedicated to all the people who have accompanied me along this journey. Their influences and contributions might have been very different in their nature, but without all of you this would not have been possible and I am deeply grateful for having met every single one of you!

In more detail I want to thank/Mein besonderer Dank gilt...

...my supervisor Angel Rubio for giving me the opportunity to pursue my Ph.D. in his group. It has been an excellent working environment with outstanding resources, both human and scientific. I am grateful for all the experiences I was able to make during the past four years.

...meinem Betreuer, Johannes Lischner. Ich danke dir für die Zeit und Geduld die du in den letzten Jahren in meine Ausbildung investiert hast. Ich habe nicht nur systematisches Arbeiten und kritisches Hinterfragen von Ergebnissen von dir gelernt, sondern auch wie wichtig es ist Geduld zu haben. Durch deine positive, motivierende Art habe ich auch die Zeiten wo die Forschung frustrierend war gut überwinden können. Gleichzeitig ist es dir gelungen, verständnisvoll auf verschiedene Persönlichkeiten und Situationen einzugehen was eine seltene menschliche Qualität ist. Ich habe es sehr geschätzt mit dir zu arbeiten und danke dir von Herzen für all die Unterstützung die du mir gegeben hast, ohne dich hätte das alles nicht geklappt!

...the members of my committee, Professor Gabriel Bester, Professor Volker Abetz, Professor Carmen Herrmann and Professor Arwen Pearson, who have sacrificed their time for examining my thesis and attending my defence.

...meinen Großeltern Margret und Alfred Göbel. Opa, du hast die Abgabe meiner Doktorarbeit nur um wenige Wochen verpasst, aber du gehörst genauso sehr auf diese Seiten wie jeder andere hier! Ihr habt mich mit großgezogen und seid immer schon wie Eltern für mich gewesen. Ich habe von euch so unglaublich vieles gelernt, sei es Fahrradfahren, Naturkunde oder aber einfach was es heißt Rückgrat zu haben. Ihr habt mich geprägt wie kaum jemand sonst und ohne euch wäre ich sicherlich nicht der Mensch der ich heute bin. Ich bin zutiefst dankbar für die vielen Jahre die wir zusammen verbringen durften. Opa, du hast immer gesagt dass du es schön fändest wenn ihr beide es noch erlebt dass ich meinen Dokortitel bekomme. Leider hat es für dich nicht mehr ganz geklappt, aber ich weiß dass du immer stolz auf mich warst, mit oder ohne Titel. Deshalb habe ich diese

Arbeit euch beiden gewidmet.

...meinen Eltern Horst und Angela Göbel. Ich danke euch für die Unterstützung die ihr mir habt zu Teil werden lassen, dass ihr mich großgezogen habt und für die Investitionen in meine Ausbildung ohne die ich wahrscheinlich nicht diesen Weg eingeschlagen hätte.

...meiner Schwester Susanne Göbel. Ich bin dankbar dafür dass ich dich habe und auch wenn wir in vielerlei Hinsicht sehr verschieden sind respektieren und unterstützen wir uns gegenseitig. Ich hab dich lieb!

...der tollsten Nichte der Welt, Katharina Göbel.:)

...meinem Partner Matthias Ruppert. Ich danke dir für deine Unterstützung in den schweren Zeiten, dafür dass die schönen Zeiten mit dir noch schöner sind und dafür dass du mich nie eingeengt hast. Ich kann wahrscheinlich mit keinem Menschen so viel lachen wie mit dir und ich hoffe dass wir bald zusammen durch leichtere Jahre gehen können.

...meinen Freunden Katharina Beine und Johannes Kaub. Ich kann mit euch einfach unglaublich viel Spaß haben, wir haben in den letzten 11 Jahren viel erlebt, Gutes und Schlechtes, aber egal was war, ich wusste einfach immer dass ich auf euch zählen kann. Auch wenn wir uns ewig nicht sehen ist es doch wie früher und wir haben es über lange Zeiten und große Distanzen geschafft uns das zu erhalten. Menschen wie euch trifft man einfach nicht oft und ich bin dankbar, Freunde wie euch zu haben.

...my "international cooking crew", Mary-Leena Tchenkoue-Djouom and Yashoj Shakya, for many fun cooking and baking nights, outings to the park, games of Kubb (one day Yashoj, one day we will beat you :D), an amazing "vacation" to "Portugal" and just for being around.

...den wunderbaren Menschen, die oft hinter den Kulissen im Institut dafür sorgen, dass alles funktioniert. Insbesondere möchte ich hierbei Ute Ramseger, Kathja Schroeder, Tania Hartin, Graciela Sanguino, Miriam Lange, Patricia Rihs, Gisbert Mantei, Andre Hein, Henning Glawe, Björn Witt, Neda Lotfiomran, Dagmar Schröder-Huse, Ralf Westermann und Frauke Kleinwort danken (und ich hoffe sehr, dass ich hier niemanden vergessen habe). Ihr seid für mich die Seele und das Rückgrat des Instituts!

...Micael Oliveira, whom I consider "the fairy godmother" of my Ph.D. and of course Nicolas Tancogne-Dejean and Martin Lüders. All three of you are extremely busy, but you always took your time to teach me, help me with problems and wrestle down the "eight-armed beast" if it was misbehaving. :) I learned so much from all of you and without you I would not be at the point where I am today.

...the amazing people from my group at MPSD, especially Uliana Mordovina, Theresa Reinhardt, Dominik Sidler, Franco Bonafe, Christian Schäfer, Fabio Covito, Mona Kalthoff, Kevin Liveley, Florian Buchholz, Iris Teophilou and of course, last but not least, the won-

derful people with whom I have had the pleasure of sharing an office over the years, Wenchuan Yang, Mary-Leena Tchenkoue-Djouom, Karen Fidanyan and Zahra Nourbakhsh. It was great to have you there to share successes, failures and lots of coffee and laughter and I am grateful for the friendships that have formed!

...the awesome people who I have met in London. I can't name all of you because this would make the list too long, but I will put some honorable mentions here. :) First of all, I want to thank Martik Aghajanian. We connected right from the start and it's just been a blast meeting you. I really appreciate how genuine you are and we have had many personal and awesome conversations as well as many beers and laughs. Without you I would have felt quite lonely in London at times and I am grateful for having you as a friend. You are an awesome person!

I also want to thank Lara Roman-Castellanos for amazing shared travelling experiences, cooking successes and baking disasters, remote tea-times, deep conversations and lots of laughter. I am really glad that we met and can't wait to travel with you again!

I also want to thank Miriam Scharnke for her honesty, having a really kind heart and starting a knitting/crocheting/sewing What's App group (ooof, what a word... :D) during Covid times. I am also grateful for having met Matthias Khak, Zachary Goodwin, Stefano Dal Forno, Harry Demetriou, Milla Paulomaa and just basically all of the other wonderful people from the office. Whether it was drinks, climbing, board games or just kitchen banter at lunch time, it was fun! You have made my times in London special!

...Herrn Professor Liauw und Herrn Professor Raabe. Sie beide waren für mich Mentoren und haben an mich geglaubt wenn ich es nicht getan habe. Ohne Ihre Ermutigungen hätte ich niemals eine Doktorarbeit angefangen. Es ist so wichtig dass es Menschen wie Sie gibt und ich bin sehr dankbar dafür.

...the IMPRS and the RTG QM³ graduate schools for additional financial support and interesting field trips and lovely people.

...all the people that I might have forgotten to mention here for being understanding and knowing that I do appreciate you nevertheless. :)

Eidesstattliche Versicherung

Hiermit versichere ich an Eides statt, die vorliegende Dissertationsschrift selbst verfasst und keine anderen als die angegebenen Hilfsmittel und Quellen benutzt zu haben.

Die eingereichte schriftliche Fassung entspricht der auf dem elektronischen Speichermedium.

Die Dissertation wurde in der vorgelegten oder einer ähnlichen Form nicht schon einmal in einem früheren Promotionsverfahren angenommen oder als ungenügend beurteilt.

Hamburg, den 30.8.2021